

Habilitationsschrift

zur
Erlangung der Venia legendi
für das Fach Physik
der
Ruprecht-Karls-Universität
Heidelberg

vorgelegt von
Heiko Scheit
aus
Arnstadt
2005

*Für
Simona*

The New Radioactive Nuclear Beam Facility
REX-ISOLDE/MINIBALL:
Sub-Barrier Coulomb Excitation of $^{30,32}\text{Mg}$
and the “Island of Inversion”

Abstract

The understanding of the structure of nuclei far from stability is one of the key problems in nuclear structure physics today. The questions to be addressed range from understanding of the limits of nuclear stability to the origin of the elements. While in nature there are only about 300 stable isotopes, there are more than 3000 unstable nuclides that have already been observed and an equal number that is expected to exist. Beams at most accelerator laboratories are restricted to the few stable isotopes. Therefore, only stable nuclei or nuclei close to stability are well studied (with some exceptions). On the contrary, little is known about the properties of especially neutron-rich exotic nuclei, characterized by an extreme ratio of neutron to proton number; for some of them only their existence is known.

With the commissioning of the REX-ISOLDE facility and the MINIBALL γ ray spectrometer, in which our group had a leading role, it is now possible to study nuclides far from stability with standard nuclear physics techniques such as “safe” Coulomb excitation, allowing to make systematic studies of key properties of exotic nuclei over wide regions in the nuclear chart, yielding a significant contribution to the understanding of nuclear structure.

In this work the main aspects of the REX-ISOLDE accelerator and of the MINIBALL array are presented. After the commissioning phase two experimental campaigns were carried out with the aim of shedding new light on the interesting region of the “Island of Inversion”. In this first study the reduced transition probabilities $B(E2; 0_{\text{gs}}^+ \rightarrow 2_1^+)$ of the neutron-rich isotopes $^{30,32}\text{Mg}$ were measured using the model-independent technique of “safe” Coulomb excitation. While the $B(E2)\uparrow$ of ^{30}Mg can be understood in terms of pure sd shell model configurations, the large value of ^{32}Mg is consistent with a pure $2p\text{-}2h$ configuration with a breakdown of the $N = 20$ shell closure at $Z = 12$. The reasons for this surprisingly abrupt transition into the “Island of Inversion” are discussed.

Danksagung

An dieser Stelle möchte allen, die am Zustandekommen dieser Arbeit beteiligt waren, von ganzem Herzen danken. Ich danke

- Dirk Schwalm für die Möglichkeit mit ihm zu arbeiten, für die Unterstützung und besonders für die große Freiheit die er mir während der Zeit am Institut gewährt hat.
- Christoph Gund, Martin Lauer, Hans Boie, Jörg Fitting, Vinzenz Bildstein, und Oliver Niedermaier, die durch ihre Diplom- und Doktorarbeiten diese Arbeit erst möglich gemacht haben.
- den REX Beschleunigerleuten, insbesondere Thomas Sieber, Robert v. Hahn, Oliver Kester, und vielen anderen mehr, ohne deren Einsatz die Experimente am CERN unmöglich gewesen wären.
- the members of the MINIBALL collaboration and everybody helping out during the experiments at CERN.
- Frank Köck für die Unterstützung bei größeren und kleineren Computerproblemen und die immer offene Tür.
- Helga Krieger, die immer zu Helfen wusste und (oft vergebens) für das kulturelle Angebot Heidelbergs warb.
- meinen Eltern, besonders meiner Mutter.
- Simona und natürlich Theodor, ohne die alles keinen Sinn haben würde.

Contents

Abstract

Danksagung

List of Figures xiii

List of Tables xv

1 Introduction 1

2 The REX-ISOLDE Facility 9

2.1 Re-Accelerated Radioactive Nuclear Beams 9

2.2 The ISOLDE Facility 11

2.3 The REX-ISOLDE Accelerator 13

2.4 Time Structure of the REX-ISOLDE Beam 14

2.5 Sources of Beam Contamination 16

3 The MINIBALL γ Ray Spectrometer 19

3.1 γ Ray Spectroscopy 19

3.2 Doppler Shift and Broadening 21

3.3 The Main Interaction Concept 23

3.4 The MINIBALL Array 26

3.5 Position Sensitivity and Pulse Shape Analysis 37

3.6 Standard Setup 46

4 Coulomb Excitation 51

4.1 General Considerations 51

4.2 Coupled Equations 54

4.3 First Order Perturbation Theory 58

4.4	Re-Orientation	60
4.5	De-Orientation	61
4.6	“Safe” Distance Condition	61
4.7	Intermediate Energy Coulomb Excitation	63
4.8	Experimental Method	64
5	First Results	71
5.1	Determination of Beam Impurities	71
5.2	Analysis of the Data	78
5.3	Results	84
6	$^{30,32}\text{Mg}$ and the “Island of Inversion”	87
6.1	Experimental Results	87
6.2	Experiment and Theory	91
6.3	On the Evolution of the Shell Structure	97
6.4	“Island of Inversion”	99
7	Summary and Outlook	103
	Bibliography	105

List of Figures

1.1	Schematic nuclear chart.	2
1.2	$B(E2; 0_{\text{gs}}^+ \rightarrow 2_1^+)$ values of the neutron-rich even-even Mg isotopes.	7
2.1	Production of re-accelerated radioactive nuclear beams.	10
2.2	Layout of the ISOLDE facility.	11
2.3	ISOLDE production target.	12
2.4	Schematic setup of REX-ISOLDE.	13
2.5	Picture of REX in 2002.	14
2.6	REX time structure.	15
2.7	EBIS Pulse.	15
3.1	EUROBALL cluster cube setup.	21
3.2	γ ray energy resolution and effective opening angle.	22
3.3	Schematic detector setup.	24
3.4	Main Interaction Concept	25
3.5	Geometry of the MINIBALL Ge crystals.	27
3.6	Schematic view of a MINIBALL module.	29
3.7	Pictures of the MINIBALL capsule.	29
3.8	Picture of the quadruple cryostat head.	31
3.9	Picture of a MINIBALL triple detector.	32
3.10	Digital electronics.	33
3.11	Analog part of the MINIBALL electronics.	34
3.12	Picture of a XIA DGF-4C.	35
3.13	MINIBALL.	37
3.14	MINIBALL efficiency.	38
3.15	Definition of radius r and azimuth ϕ	38
3.16	Weighting field of true co-axial detector.	40
3.17	Composition of a current signal.	41

3.18	Determination of r	42
3.19	Determination of ϕ	43
3.20	MINIBALL energy resolution in in-beam experiment.	45
3.21	Standard MINIBALL setup.	47
3.22	MINIBALL from top.	48
4.1	Schematic Coulomb trajectory.	52
4.2	Coulomb excitation amplitues.	60
5.1	Energy loss vs. t_p	73
5.2	Release curve.	74
5.3	Beam contamination as function of time.	77
5.4	Energy vs. angle for ^{30}Mg	79
5.5	Doppler corrected γ ray energy spectra.	80
5.6	Ni transfer lines.	81
5.7	^{32}Mg Coulomb excitation.	84
6.1	Experimental $B(\text{E2}; 0_{\text{gs}}^+ \rightarrow 2_1^+)$ values.	89
6.2	Coulomb-nuclear interference at intermediate-energies.	91
6.3	Experimental and theoretical $B(\text{E2})\uparrow$ values.	92
6.4	Experimental and theoretical level schemes.	93
6.5	Prediction based on Grodzins type systematics.	96
6.6	Nuclear single-particle levels of exotic nuclei.	98
6.7	Illustration of monopole shift.	98
6.8	Compilation of properties of nuclei near the “Island of Inversion”.	100
6.9	Compilation of $E2$ properties near the “Island of Inversion”.	101
6.10	Relevant references concerning the nuclei near the “Island of Inversion”.	102

List of Tables

5.1	Methods to measure the beam contamination.	76
5.2	Amount of ^{30}Al contamination in the beam.	77
5.3	Results for ^{22}Ne Coulomb excitation.	83
5.4	Summary of experimental campaigns.	85
5.5	The influence of the assumed $Q(2^+)$ on the extracted $B(\text{E}2)\uparrow$ value.	86
6.1	Summary of experimental $B(\text{E}2; 0^+_{\text{gs}} \rightarrow 2^+_1)$ values.	88

Nomenclature

Symbols and abbreviations used. The page of first occurrence is given.

α	fine structure constant: $\alpha \approx \frac{1}{137}$, p. 52.
β	Velocity v in units of the speed of light c : $\beta = \frac{v}{c}$, p. 23.
$\langle I_0 \parallel \mathcal{M}(E\lambda) \parallel I_f \rangle$	reduced matrix element, p. 56.
$\langle I_0 m_0 \mid \mathcal{M}(E\lambda, \mu) \mid I_n m_n \rangle$	electric multipole matrix element, p. 59.
Δ_s	safe distance, p. 62.
ϵ	total efficiency, p. 67.
ϵ_γ	total γ ray detection efficiency, p. 65.
$\epsilon_D(\Omega_\gamma)$	efficiency of γ ray detector (in laboratory system), p. 67.
$\langle \epsilon_\gamma \rangle$	averaged (total) γ ray efficiency, p. 65.
η	Sommerfeld parameter, p. 52.
$\frac{d\sigma}{d\Omega}$	differential cross section, p. 53.
γ	relativistic factor: $\gamma = \frac{1}{\sqrt{1-\beta^2}}$, p. 23.
\hbar	Planck's constant h divided by 2π , p. 53.
λ	multipolarity of transition, p. 59.
λ	de Broglie wavelength, p. 52.
$\mathcal{M}(E\lambda, \mu)$	electric multipole operator, p. 56.
$\mid 0 \rangle$	ground state, p. 55.
$\mid \psi \rangle$	time-dependent state vector, p. 55.
$\mid Im \rangle$	eigenstate of I^2 and I_z , p. 55.
$\mid n \rangle$	free nuclear eigenstate, p. 55.
$\mid \psi(t) \rangle$	time-dependent nuclear state vector, p. 54.
$\mid \psi \rangle$	nuclear state vector, p. 54.
μ	change in magnetic quantum number, p. 59.
Ω	solid angle direction (θ, ϕ) , p. 65.
$d\Omega$	solid angle element: $d\Omega = d\cos\theta d\phi = \sin(\theta)d\theta d\phi$, p. 65.
Ω_γ	direction of γ ray: $\Omega_\gamma = (\theta_\gamma, \phi_\gamma)$, p. 67.

Ω_D	solid angle covered by the particle detector, p. 59.
ω_{nm}	characteristic frequency for transition from state n to m , p. 57.
ϕ	azimuthal angle in the MINIBALL module (see figure 3.15 on page 38), p. 42.
ρ	statistical tensor, p. 67.
σ	Coulomb excitation cross section, p. 65.
σ	cross section, p. 53.
σ^p	Coulomb excitation cross section of the projectile, p. 65.
σ^t	Coulomb excitation cross section of the target, p. 65.
σ_i^{tk}	cross section to excite target component k by beam component i , p. 66.
σ_k^{pi}	cross section to excite beam (projectile) component i by target component k , p. 66.
σ_R	Rutherford cross section, p. 53.
τ_c	collision time, p. 57.
τ_n	nuclear period, p. 57.
θ	(scattering) angle, p. 53.
φ	angle within one segment of a MINIBALL module measured from the center line, p. 44.
ξ	adiabaticity parameter, p. 57.
A	nuclear mass number, p. 62.
a_0	half-distance of closest approach in a head-on collision, p. 52.
a_k	abundance of target component k , p. 66.
a_n	excitation amplitude for state $ n\rangle$, p. 54.
$a_{2,4}$	coefficients in front of Legendre polynomials in the expression for the angular distribution of γ rays, p. 61.
b	impact parameter, p. 52.
$B(E\lambda; I_0 \rightarrow I_f)$	reduced transition probability, p. 56.
b_γ	branching ratio, p. 67.
b_i	abundance of beam component i , p. 66.
C	capacitance, p. 33.
$d\Omega$	solid angle element, p. 53.
$D_{\min}(\theta)$	distance of closest approach, p. 62.
$E^{(0)}$	γ ray energy in frame of emitter, p. 23.
E_{cm}	center-of-mass energy, p. 62.
E_ξ	transition energy for $\xi = 1$, p. 57.
E_{lab}	γ ray energy in laboratory, p. 23.
$f_{E2}(\xi)$	total cross section functions, p. 59.

$f_{E\lambda}(\theta, \xi)$	cross section functions, p. 59.
$f_{E\lambda}(\xi)$	total cross section functions, p. 59.
$G_{2,4}(t)$	attenuation coefficient for angular distribution of γ rays , p. 61.
H	nuclear Hamiltonian, p. 54.
I	number of beam components, p. 66.
i	label of beam component, p. 66.
K	number of target components, p. 66.
k	label of target component, p. 66.
L	luminosity, p. 65.
l	orbital angular momentum of shell model single particle state, p. 97.
L_{ik}	luminosity, p. 66.
m	reduced mass, p. 54.
m_e	mass of the electron, p. 26.
N_{γ}^{pi}	γ ray yield of beam (projectile) component i , p. 66.
N_{γ}^{tk}	γ ray yield of target component k , p. 66.
$(N/A)_t$	number of scattering centers N per target area A , p. 65.
N_{γ}	γ ray yield, p. 65.
$N_{\gamma}^{t,p}$	number of (detected) γ rays , p. 65.
N_b	number of incident beam particles, p. 65.
$P_i(\cos \theta)$	Legendre polynomials, p. 61.
P_n	probability to excite state $ n\rangle$, p. 54.
R	nuclear radius, p. 62.
$S_{E\lambda\mu}$	orbital integral, p. 59.
t	time of event, p. 72.
t	time, p. 54.
T_1	time of last proton impact onto the ISOLDE target, p. 72.
t_p	time (of event) since last proton impact $t_p := t - T_1$, p. 72.
u	atomic mass unit, p. 72.
V	electro-magnetic potential, p. 54.
$W(\Omega_{\gamma})$	γ ray angular distribution (in system of emitting nucleus), p. 67.
$Z_{p,t}$	proton number of projectile and target, respectively, p. 52.
$B(E2)\uparrow$	$B(E2; 0_{\text{gs}}^+ \rightarrow 2_1^+)$, p. 55.
$B(E2; 0_{\text{gs}}^+ \rightarrow 2_1^+)$	reduced transition probability, p. 55.
CE	Coulomb excitation, p. 51.
DAQ	data acquisition, p. 16.
DAQ	data acquisition, p. 35.

DGF-4C	4 channel digital gamma finder, CAMAC module by XIA, Inc., p. 34.
DSP	digital signal processor, p. 35.
FE	full energy, p. 23.
FEE	full-energy event, p. 23.
FEP	Peak formed in a γ ray energy spectrum by the FEE, p. 26.
FET	field effect transistor, p. 31.
FI	first interaction, p. 23.
FIFO	first-in-first-out memory, p. 35.
FPGA	field programmable gate array, p. 35.
FWHM	full width at half maximum, p. 46.
HPGe	High Purity Germanium, p. 28.
ISOLDE	Isotope Separator On-Line DEvice, p. 9.
MI	main interaction, p. 23.
PSA	pulse shape analysis, p. 21.
PSB	proton synchrotron booster, p. 11.
REX	Radioactive beam EXperiment, p. 9.
RILIS	resonance ionization laser ion source, p. 17.
RNB	Radioactive Nuclear Beam, p. 1.
USD	universal <i>sd</i> interaction [1], p. 94.

Chapter 1

Introduction

Before the mid 1990s most experimental studies in nuclear structure physics, involving beams incident on suitable targets to excite the nuclei, have focused on nuclei in or near the valley of stability, due to the fact that the beams and targets used in accelerator laboratories are mainly composed of naturally occurring stable or very long-lived radioactive isotopes. The reaction products are therefore near stability, with the exception of neutron-deficient fusion-evaporation products and neutron-rich fission products available in limited regions of the nuclear chart. There are, however, less than 300 stable nuclides in nature, while already about 3000 unstable ones have been synthesized in nuclear structure laboratories. Only a fraction of them was studied in any detail and for many no other property than their existence is known. In addition, the nuclear landscape extends much further away into uncharted territories mainly on the neutron-rich side, where probably about another 3000 nuclides await discovery, as shown schematically in figure 1.1.

The study of these exotic nuclei¹ with radioactive nuclear beams (RNB) has emerged as a new and young field of nuclear structure physics about 10–15 years ago gaining more and more momentum. This development, which represents the principal future direction of nuclear structure physics, is driven by the availability of ever better and more intense RNBs and allows the systematic study of the evolution of nuclear structure in the isospin degree of freedom. The number of available (radioactive) beams at RNB facilities is an order of magnitude higher (albeit strongly varying intensity) than the number of stable ones, giving the experimenter the possibility to very flexibly choose the beam that best shows and amplifies the effect to be observed.

We have every reason to expect new phenomena and new insights into the nuclear many body problem as more and more exotic nuclei are studied:

¹Exotic nuclei refer to β unstable nuclei with extreme ratios of proton to neutron number.

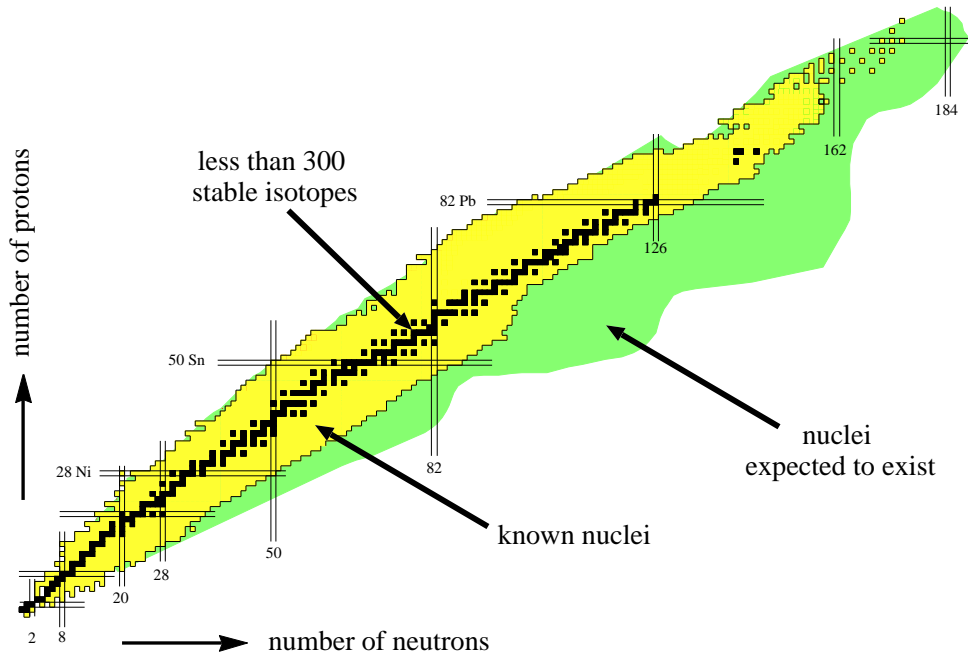


Figure 1.1: Schematic nuclear chart.

- Historically, the few exotic nuclei known have shown many remarkable phenomena from neutron-halos to the melting of magic shells, giving invaluable insights into the shell model which is the core or reference model for any nuclear structure theory today.
- Nuclei, where the valence orbits of neutrons and protons have very different quantum numbers, can be accessed and studied. It is expected that the residual interaction will be very different in comparison to stable isotopes, where the valence orbits, which determine most of the nuclear structure properties, have usually rather similar quantum numbers.
- The isospin dependence of certain observables can be systematically studied along extended isotopic and isotonic chains for the first time. The further away a certain nuclide is from stability the more sensitive the theoretical results are to the (parameters of the) theoretical model. For instance, before the melting of closed shells was discovered around ^{32}Mg (“Island of Inversion”) no model predicted it.
- The weakening of the spin-orbit force is predicted for very neutron-rich nuclei, resulting in a completely different shell structure, which has yet to be confirmed (see e.g. figure 6.6 on page 98).

- Extremely weakly bound systems can be produced and studied. While the nucleons in nuclei close to stability are bound by several MeV, the most exotic nuclei near the proton and neutron driplines are bound by less than a few 100 keV.
- The origin of the elements is considered one of “The 11 Greatest Unanswered Questions of Physics” [2]. While there certainly are very large uncertainties in the astrophysical models—not even the site of element production is identified—without knowledge of the properties of the exotic nuclei involved in the r - and rp -process a deeper understanding of the origin of the elements cannot be expected.

In the last 10–15 years the nuclear structure physics with RNBs was mainly driven by advances of projectile fragmentation facilities such as GSI (Germany), MSU (USA), GANIL (France), and RIKEN (Japan). New probes, adapted to the properties of these beams (high energy and poor beam quality), were developed (e.g. intermediate-energy Coulomb excitation) yielding valuable insight in the structure of exotic nuclei. However with these facilities the standard techniques such as “safe” Coulomb excitation cannot be employed.

It was clear, therefore, that besides projectile fragmentation an alternative method, namely isotope separation on-line (ISOL) with re-acceleration of the ions, is needed to fully exploit the possibilities of RNBs. Such a facility was termed generically as IsoSpin Laboratory already in the mid-1990s, for the obvious reason. The major planned facilities of this type, with construction costs in excess of 500 M€, are RIA [3] in the USA and EURISOL [4] in Europe, which were recommended by the corresponding scientific advisory panels (NSAC and NuPECC, respectively) as the highest priority for new construction.

While these facilities (if fully funded and built) are expected to become online in 10–20 years from now, there are several first generation ISOL facilities already operational, e.g. CRC at Louvain-la-Neuve [5], HRIBF at Oak Ridge [6], ISAC at TRIUMF in Vancouver [7], and SPIRAL at GANIL, Caen [8]. A first generation ISOL facility which was just commissioned three years ago is REX-ISOLDE² [9–11], which is special, since it is located at ISOLDE, CERN, which has a huge expertise and knowledge in the production and extraction of radioactive nuclei, collected in more than 30 years of operation. But so far *without* re-acceleration of the produced exotic nuclei. With REX, in principle, any nucleus on the huge and ever expanding ISOLDE beam list can be accelerated to energies around the Coulomb barrier, which is the energy of choice for most nuclear structure experiments.

²The REX collaboration initially consisted of institutes from the following cities: Aarhus, Brookhaven, Daresbury, Darmstadt, Dubna, Erlangen, Frankfurt, Gothenborg, Göttingen, Heidelberg, Leuven, Liverpool, Mainz, München, Paris, Saclay, Stockholm, Strasbourg, Surrey, Roskilde, and Villeurbanne [9].

The REX project was initiated in 1994 at the MPI-K [9] with strong involvement of the accelerator group throughout the project and of the nuclear physics group, which was essential during the commissioning phase in 2001–2002, where the whole REX/MINIBALL beam time was allocated to experiments proposed by the MPI-K group.

With the development of the RNB facility REX-ISOLDE it became clear that experimental equipment is needed that makes best use of the rare and expensive RNBs. Advances in detector efficiency and resolution not only allow for more precise measurements, but also to extend the limits of our knowledge to more exotic nuclei, as a reduction in beam intensity can be compensated by a corresponding increase in efficiency of the experimental setup. The MINIBALL³ HPGe γ -ray array [12] was especially designed and built for REX-ISOLDE and is currently the main experimental device at the REX-ISOLDE accelerator. It is the first array (in production use) employing segmentation of the detector electrodes and pulse shape analysis to increase the granularity of the array. The algorithms used were developed at the MPI-K during one Diploma [13] and two Ph.D. thesis [14, 15], were first tested on a triple cluster detector during a Diploma project [16] and implemented on the hardware during another Diploma [17] and one Ph.D. [18] project.

With REX and MINIBALL operational after the commissioning period our group was leading the research effort with the new devices by studying the neutron-rich even- A Mg isotopes by the well established and proven technique of “safe” sub-barrier Coulomb excitation. These nuclei are of particular interest, as they are located in the so-called “Island of Inversion” comprising the neutron-rich Ne, Na, and Mg isotopes with neutron number near $N = 21$. These isotopes show unusual properties, which could not be understood on the basis of shell-model calculations with the active orbits restricted to the $1s, 0d$ (sd) major shells. Even today, more than 30 years after the first anomalies were found, the reason for the existence of the “Island of Inversion” and its extent in neutron N and proton number Z in the nuclear chart are still debated in the literature and the huge interest on this region can be seen on the number of pertaining publications showing a strong increase especially in recent years.

The $N = 21$ nuclide ^{32}Na is generally believed to be at the center of the “Island of Inversion”. This nuclide as well as several other neutron-rich Na isotopes ($^{27-32}\text{Na}$) were first observed in 1969 at the ISOLDE facility [19]. Their masses were measured in 1973 and 1975 [20, 21] and a first irregularity was found. It was observed that contrary to expectation (from the spherical shell model) the deduced two-neutron separation energies S_{2n} actually

³Currently the MINIBALL collaboration comprises the following institutes: the LMU Munich, the TU Munich, the MPI-K Heidelberg, the GSI Darmstadt, the University of Cologne, the University of Leuven, the University of Edinburgh, and the University of York.

increased as the $N = 20$ shell was crossed toward more neutron-rich nuclei, which the authors took as a sign of deformation.⁴ Indeed, constrained Hartree-Fock calculations—with the quadrupole moment as constraint—by Campi *et al.* [22] suggested that the filling of the negative parity $\nu f_{7/2}$ shell would result in a deformed ground state configuration with increased binding. An extension of the mass measurements [23] to include the Mg isotopes up to ^{32}Mg showed that $^{31,32}\text{Mg}$ are also more tightly bound than expected, showing that the observed anomalies are not restricted to the Na isotopes. A further indication of a deformed ground state configuration came from a measurement of the energy of the first excited state of ^{32}Mg (assumed to have $J^\pi = 2^+$).⁵ It was found to lie at the remarkably low energy of only 885 keV [29], while most even- A $N = 20$ isotones with $Z > 12$ showed 2_1^+ excitation energies $E(2_1^+)$ in excess of 3 MeV [25] in line with the $N = 20$ shell closure. At the time it was believed that Coulomb excitation studies, giving a direct and model independent measure of deformation, would be impossible for these very exotic neutron-rich nuclides [23]. Therefore indirect methods were used to provide evidence of nuclear deformation. Besides the excitation energy in even nuclides, the variation of the mean square (charge) radii or isotope shifts and the two-neutron separation energies S_{2n} were investigated. The mean square charge radii showed a strong continuous increase with larger neutron number N , however, no sign of a sudden change when $N = 20$ was approached for the neutron-rich Na isotopes [30, 31] was observed, which would have been indicative of the onset of deformation.

The theoretical understanding of these nuclei was the subject of a multitude of publications (e.g. [22, 32–36] and references therein) and in a seminal shell model study by Warburton, Becker, and Brown [36], based on the work of Wildenthal and Chung [33], this region was termed “Island of Inversion” and according to these authors encompassed the Ne, Na, and Mg isotopes with neutron numbers in the range $20 \leq N \leq 22$ as outlined in [36, figure 1]. In this publication the origin of this peculiar structure was traced to three important mechanisms:

- a (small) reduction in the single-particle gap between the $\nu f_{7/2}$ and the $\nu d_{3/2}$ orbitals,

⁴While, a priori, the S_{2n} value is not related to the shape of a nucleus, two types of variation from a smooth behavior as a function of the mass number A have been observed. When crossing a magic number it is expected that new orbitals with less binding become active, resulting in a steep(er) drop of the S_{2n} value. However, a leveling off or even an upturn of S_{2n} with increasing A has been observed. Here new (shell model) configurations become accessible resulting in a stronger binding. This is typically associated with the occurrence of deformation.

⁵In even-even nuclides the energy of the first excited 2^+ state is related empirically to the $B(E2; 0_{\text{gs}}^+ \rightarrow 2_1^+)$ value [24, 25], which is a direct measure of collectivity and can be related to nuclear deformation within the rotational model [26–28].

- an increase in nn pairing energy, and
- an increase of the pn interaction energy.

These three mechanisms working together lead to a lowering of the $2\hbar\omega$ configurations and it becomes energetically more favorable to excite two neutrons into the $\nu f_{7/2}$ shell [36]. These findings, however, have been and are still being debated in the literature and explanations for the existence of the “Island of Inversion” range from large mean field effects, where in the most extreme case the energetic order of the $\nu f_{7/2}$ and the $\nu d_{3/2}$ orbits is actually reversed [22, 32, 34], to only small mean field effects with modified residual interactions, as the above mentioned strong nn and np interaction.

In the years following the discovery of the first unusual properties of the isotopes in this region, various techniques focusing on different aspects of nuclear structure were used with the aim of obtaining more detailed and more precise data and to extend the measurement to more neutron-rich nuclides. In early β decay studies the level schemes of decay products of the neutron-rich Na and Mg isotopes were studied such as ^{29}Al , $^{30,32}\text{Mg}$ [37–41]. Branching ratio, $\log ft$ values, level schemes of child nuclides, β delayed one- and two-neutron probabilities, γ intensities, Q_β values were measured providing in some cases limits on the spins and parities of the involved states. In more recent work these studies were extended to ^{35}Si , ^{33}Mg , ^{33}Al , and $^{28,29}\text{Na}$ [42–47], where in [46, 47] stopped intermediate-energy beams were used, i.e. the isotopes were produced at an in-flight facility. The results provided much information on these nuclei, but it is expected that these level schemes are rather incomplete, as only few levels are actually populated in these β decay studies.

The mass measurements were improved and extended further from stability [23, 48] and reviewed [49]. Especially in [48, figure 1] nuclides where strong deviations from sd shell model calculations in the binding energies occur can be seen. First evidence is presented that the “Island of Inversion”-effect extends below $Z = 11$ and 12 to $Z = 10$ (Ne), but not to the $Z = 13$ (Al) isotopes.

Already since 1978 laser spectroscopy was employed to deduce quadrupole moments, isotope shifts, and to determine the spins and parities of the ground states of some odd- A and odd-odd nuclei [30, 31, 50]. The determined ground state spin of $\frac{3}{2}$ of ^{31}Na gave another indication of deformation, as a spin of $\frac{5}{2}$ is expected from the spherical shell model [30]. The study of Keim *et al.* [50] showed directly that the ground state of ^{29}Na is strongly deformed, even more than predicted in an sd shell model calculation and can therefore be considered to lie at the border of the “Island of Inversion”.

A breakthrough in the experimental study of these exotic nuclides was reached in 1995 when the $B(E2; 0_{\text{gs}}^+ \rightarrow 2_1^+)$ value of ^{32}Mg was measured with the new experimental

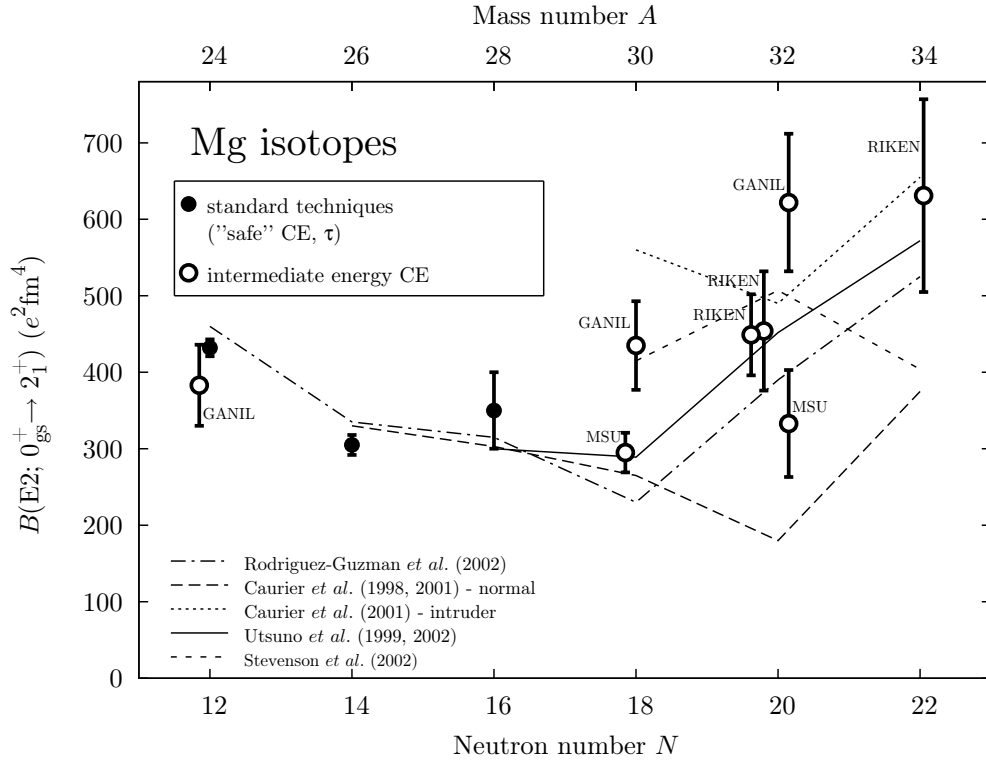


Figure 1.2: $B(E2; 0_{\text{gs}}^+ \rightarrow 2_1^+)$ values of the neutron-rich even-even Mg isotopes.

technique of intermediate-energy Coulomb excitation [51] finally giving direct evidence of large collectivity at $N = 20$. The $B(E2; 0_{\text{gs}}^+ \rightarrow 2_1^+)$ value deduced as well as the results of other experiments of this type [52–54] are shown in figure 1.2 together with results of standard methods for the nuclei near stability such as “safe” Coulomb excitation and life-time measurements [25]. Furthermore, different theoretical predictions are shown. While it is evident from figure 1.2 that most results do show a large $B(E2)\uparrow$ for ^{32}Mg , it is noticed that the values obtained at different laboratories do not agree and differences as large as a factor of two can be seen. While the origin of the differences is not known, there are several effects that might influence values obtained at unsafe beam energies, as discussed in chapter 6 on page 87.

The commissioning of the REX-ISOLDE facility and the MINIBALL array opened the possibility to study the nuclei in and near the “Island of Inversion” by standard techniques such as “safe” Coulomb excitation and single nucleon transfer reactions. In view of the apparent inconsistencies of the $B(E2; 0_{\text{gs}}^+ \rightarrow 2_1^+)$ values shown in figure 1.2 it was one of the first aims of our group to clarify the situation and to measure truly model-independent $B(E2; 0_{\text{gs}}^+ \rightarrow 2_1^+)$ values for the very neutron-rich isotopes $^{30,32}\text{Mg}$, already discussed in the original REX proposal [9] from 1994. The results of two experimental campaigns carried

out in 2003/4 as part of a Ph.D. project [55] allowed us to firmly establish that ^{30}Mg lies outside and ^{32}Mg inside the “Island of Inversion”.

In this work the first Coulomb excitation studies with beams around the Coulomb barrier near the “Island of Inversion” are presented. They are the culmination of many years of accelerator and detector development, with large contributions from the accelerator and the nuclear physics group at the MPI-K. The REX-ISOLDE facility and the MINIBALL array are introduced in chapters 2 and 3, respectively. The well established method of “safe” Coulomb excitation is shortly review in chapter 4, which also includes the description of the experimental method we used to measure the $B(\text{E}2; 0_{\text{gs}}^+ \rightarrow 2_1^+)$ values of $^{30,32}\text{Mg}$. The results, with special focus on the measurement of the beam impurities carried out as a Diploma project [56], are presented in chapter 5 and are discussed and compared to previous results and theoretical predictions in chapter 6. An outlook is given in chapter 7.

Chapter 2

The REX-ISOLDE Facility

The Coulomb excitation experiments presented in this work were performed at the newly commissioned REX¹, radioactive beam accelerator located at the ISOLDE facility at CERN, Geneva. ISOLDE operates at CERN for already more than 30 years resulting in the accumulation of a wealth of data and experience. Today, more than 600 isotopes out of 60 elements with intensities from 10^{11} to 10^{-1} s^{-1} can be provided by the ISOLDE facility. REX-ISOLDE, a first-generation radioactive ion beam facility, was developed and realized at CERN since 1995 by a European collaboration, exploiting the availability of exotic nuclei at ISOLDE. In this chapter the production methods for radioactive beams will be discussed. The ISOLDE facility and the novel REX radioactive beam accelerator will be shortly introduced. For a detailed overview of the ISOLDE facility see [57, 58] and for REX see [10, 11, 59, 60]. An overview of the activities in the last two years at REX-ISOLDE is given in [61].

2.1 Re-Accelerated Radioactive Nuclear Beams

Re-accelerated radioactive nuclear beams (RNB) are typically produced according to the scheme shown in figure 2.1 on the following page on the example of the (REX-)ISOLDE facility [57, 58, 62] at CERN. These beams are also called “ISOL-beams” as the first step is the production of the radioactive isotopes using an isotope separator on-line (ISOL) facility. This is achieved as follows: a suitable highly energetic beam (e.g. protons) bombards a thick target, consisting of many thin foils in a common container, leading to the fragmentation of the target nuclei. The produced fragments are eventually stopped in the target material. Via effusion and diffusion processes some fraction of them will reach the exit

¹REX stands for **R**adioactive beam **E**Xperiment

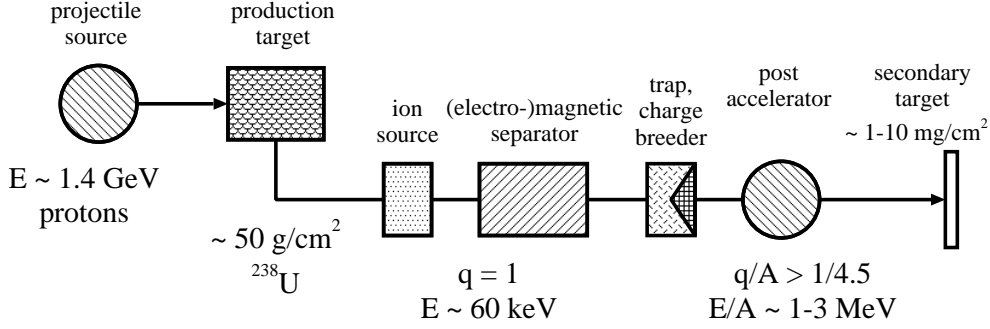


Figure 2.1: Production of re-accelerated radioactive nuclear beams.

of the target housing where the atoms of interest (and also others) are ionized by various methods. The ions are then mass separated and can readily be used for experiments such as mass measurements or β -decay studies.

In order to use the rich tools offered by fast beams, such as Coulomb excitation and transfer reactions, the nuclei have to be *re-accelerated* to energies around the Coulomb barrier. Therefore for an ISOL RNB facility at least two accelerators are involved: one for the primary beam (incident on the production target) and one for *re-acceleration* of the produced radio-isotopes. The details of the production of the radioactive nuclei as well as the acceleration scheme vary greatly from facility to facility, but common to all methods is that the produced radioactive ions are completely stopped in a target cell and the effusing atoms have to be ionized before being newly accelerated. Consequently the beams produced by this method have in principle the same beam quality as stable beams, as the ions lose all information on the production process, in contrast to in-flight facilities. The beam quality is therefore determined by the accelerator used for re-acceleration and the preceding beam preparation. Typically the beams have a good quality, i.e. a small longitudinal and transversal emittance resulting in small beam spot sizes (< 5 mm) and small energy variation ($\Delta E/E < 1\%$), especially in comparison to beams produced at in-flight facilities. But their main advantage is their (beam) energy which can be chosen to be ideally suited for the specific experiment and is typically near the Coulomb barrier.

A drawback of the ISOL method is that the beams are usually not mono-isotopic, but several isobars are present in the beam and it is not possible to have an event-by-event particle identification as is used very successfully at in-flight facilities, where most experiments are performed with so-called cocktail beams [52]. Furthermore, the effusion, diffusion and ionization process in the production target cell is highly chemically selective and therefore RNBs cannot be produced from all elements.

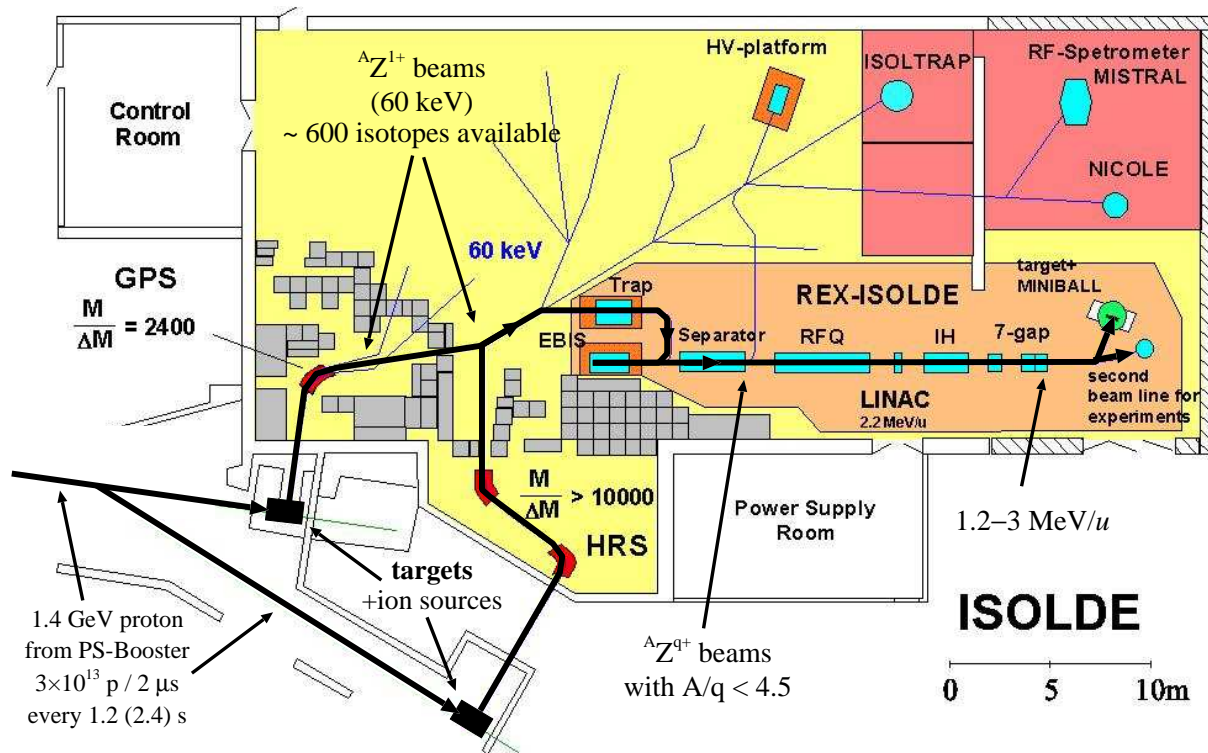


Figure 2.2: Layout of the ISOLDE facility before 2004.

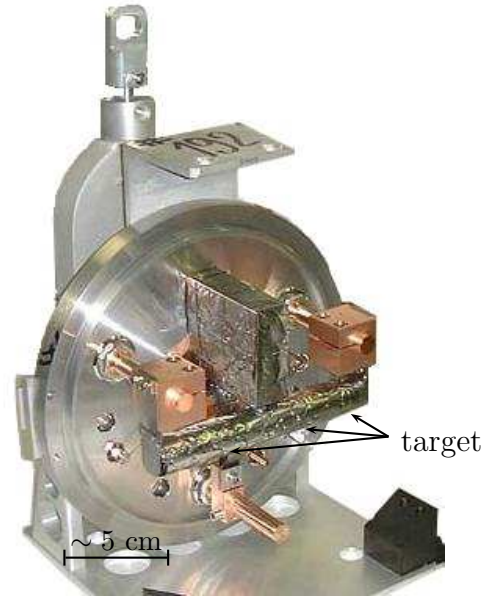
The major ISOL facilities providing re-accelerated beams currently in operation include REX-ISOLDE at CERN (section 2.3 on page 13), SPIRAL at GANIL [63], and HRIBF at ORNL [64].

2.2 The ISOLDE Facility

The ISOLDE facility—schematically shown in figure 2.2—is located at CERN and uses the highly energetic proton beam from the PS Booster (PSB), which comprises a stack of four synchrotrons accelerating protons up to an energy of 1.4 GeV. The delivered $2.4 \mu\text{s}$ long pulses contain up to $3.2 \cdot 10^{13}$ protons with a repetition time of about 1.2–2.4 s resulting in an average beam current of about $2.1 \mu\text{A}$ corresponding to a power of $\sim 3 \text{ kW}$.

This beam is incident on very thick targets (suitably chosen depending on the isotope of interest) where fission, fragmentation and spallation reactions produce the isotope of interest and many others, which are eventually stopped in the target material. A picture of such target is shown in figure 2.3 on the next page. An effusion and diffusion process transports the isotopes to an ion source producing $q = +1$ ions, which are thereafter

Figure 2.3: A typical ISOLDE production target assembly. The actual target is the silvery tube connected to the two copper current leads. The high energy proton beam from the PSB passes coaxially through the about 15 cm long target.



accelerated by a 60 keV potential step of the ISOLDE front end target station. There are several ion sources available, which are directly coupled to the target. Especially the resonant ionization LASER ion source (RILIS) [65] is of increasing importance due to its elemental selectivity, which is lacking in most other ionization techniques. Here several LASER beams (typically three) with frequencies tuned to specific atomic transitions of the element of interest are shone along the transfer tube out of the target. Ionization takes place by selectively exciting atomic transitions until the continuum is reached. In the cases of interest here, beams of Mg isotopes were produced using $\text{UC}_x/\text{graphite}$ targets ($\approx 50 \text{ g/cm}^2$ ^{238}U , $\approx 10 \text{ g/cm}^2$ C) together with the RILIS [66].

Once the ions are extracted and accelerated they have to pass through one of two mass separators. Depending on the used target station the high resolution (HRS) or the general purpose separator (GPS) is employed with nominal mass resolutions of 10^4 and 2400, respectively.² With ideal elemental resolution during the ionization process together with the mass resolution of either separator a mono-isotopic beam could be produced. Unfortunately the elemental selectivity is in most cases not sufficient so that in general there will be several contaminating isobars in the ISOLDE beam. The mass resolution of neither mass separator is sufficient to suppress these contributions except for very exotic nuclei, “high” up on the isobaric mass parabola with large mass differences. These and

²For the Mg beams of interest here the GPS was used, as a higher mass resolution would not increase the beam purity. In addition, the GPS target station possesses a higher RILIS efficiency, due to its shorter distance to the LASER station.

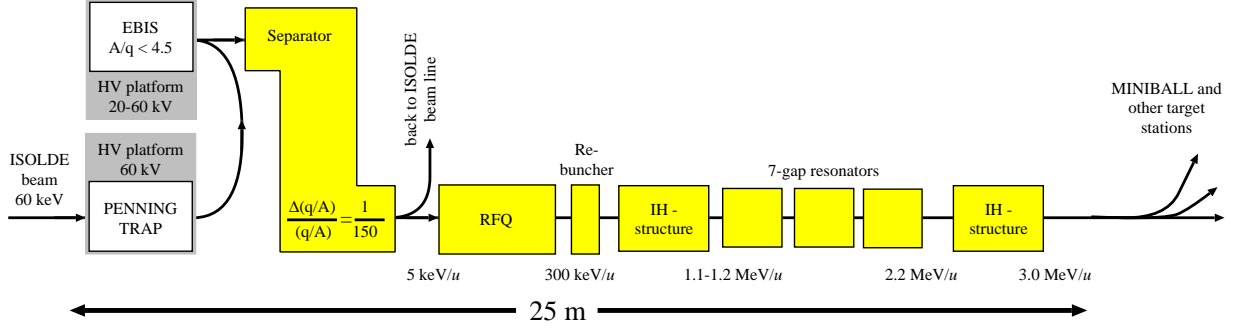


Figure 2.4: Schematic setup of REX-ISOLDE.

other sources of beam contamination are discussed in section 2.5 on page 16. In section 5.1 it is discussed how they can quantitatively be determined and how they influence the measurements presented here.

2.3 The REX-ISOLDE Accelerator

REX uses as novel charge breeding scheme to very efficiently accelerate the ions delivered by ISOLDE. These ions with charge state +1 are first accumulated, cooled and bunched in a buffer-gas filled Penning trap (REX-TRAP [67]) and then transferred to an electron beam ion source (REX-EBIS [68]), where their charge state is increased by bombarding them with a high energy electron beam. At the same time the accumulation in the REX-TRAP is resumed and the next bunch for transfer in the EBIS is prepared. The ions are released from the EBIS when a sufficiently high charge state ($A/q < 4.5$) is reached. After passing through a mass separator to remove copious residual gas components the highly charged ions can be efficiently accelerated by a short linear accelerator consisting of a radio frequency quadrupole, an interdigital H-type (IH) structure, three 7-gap resonators, and, since summer 2004, a 9-gap IH structure. The resulting maximum beam energy is 3.0 MeV/u with a possible continuous variation of the energy down to at least 1.2 MeV/u.

A schematic view and a photograph of the setup are shown in figures 2.4 and 2.5, respectively. In the latter figure the MINIBALL array can be seen in the foreground installed at the 65° beam line after a bending magnet used for the momentum analysis of the beam. The efficiency of the overall accelerator including the trap and ion source varies strongly with element, but is typically on the order of 5 %. The charge-breeder trap system has a cycling time, depending on the nuclide and the charge state to be reached, of about 20–200 ms—during this time no beam is accelerated—and the extraction pulse is

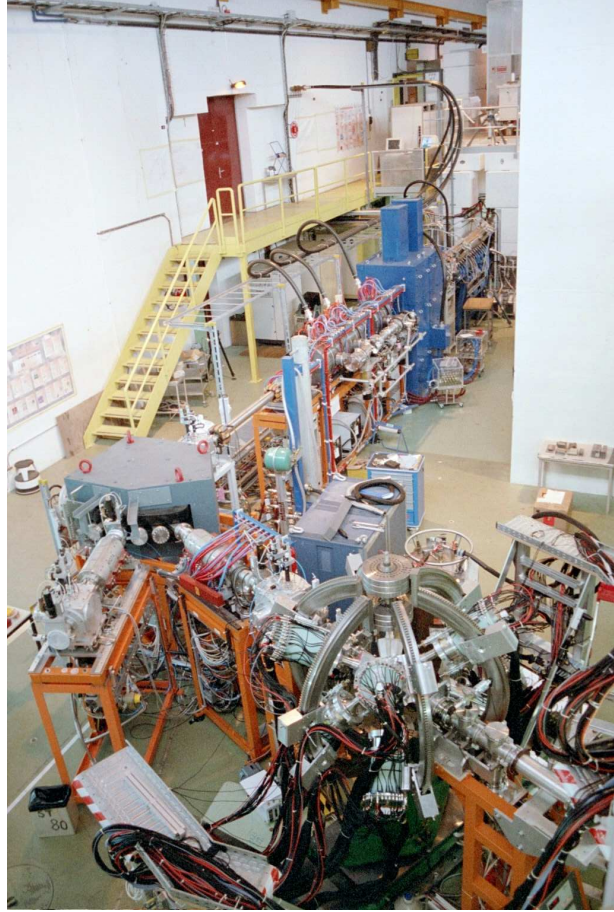


Figure 2.5: The REX accelerator at CERN in the ISOLDE hall with the MINIBALL setup in the foreground at the 65° beamline in 2002. At this time the 9-gap IH structure was not yet installed before the large bending magnet.

about $100\ \mu\text{s}$ long, resulting even for weak beams in a rather high instantaneous intensity. After commissioning of the accelerator in 2002 more than 17 nuclides of 10 elements have already been accelerated. For further details please see [10, 11, 60, 69].

2.4 Time Structure of the REX-ISOLDE Beam

Due to the mode of operation of the REX-ISOLDE accelerator the beam has an unusual time structure which is schematically shown in figure 2.6 on the next page.

To understand the micro, macro and super time structure the easiest is to follow the beam particles as they are produced and transported to the MINIBALL target. After proton impact on the ISOLDE target the produced radioactive nuclei diffuse out of the target with a certain (element dependent) release time and (isotope dependent) decay time. If one of these times is shorter than a few seconds an intensity profile as shown in panel (a) is obtained (super structure). Due to the trapping and charge breeding bunches are

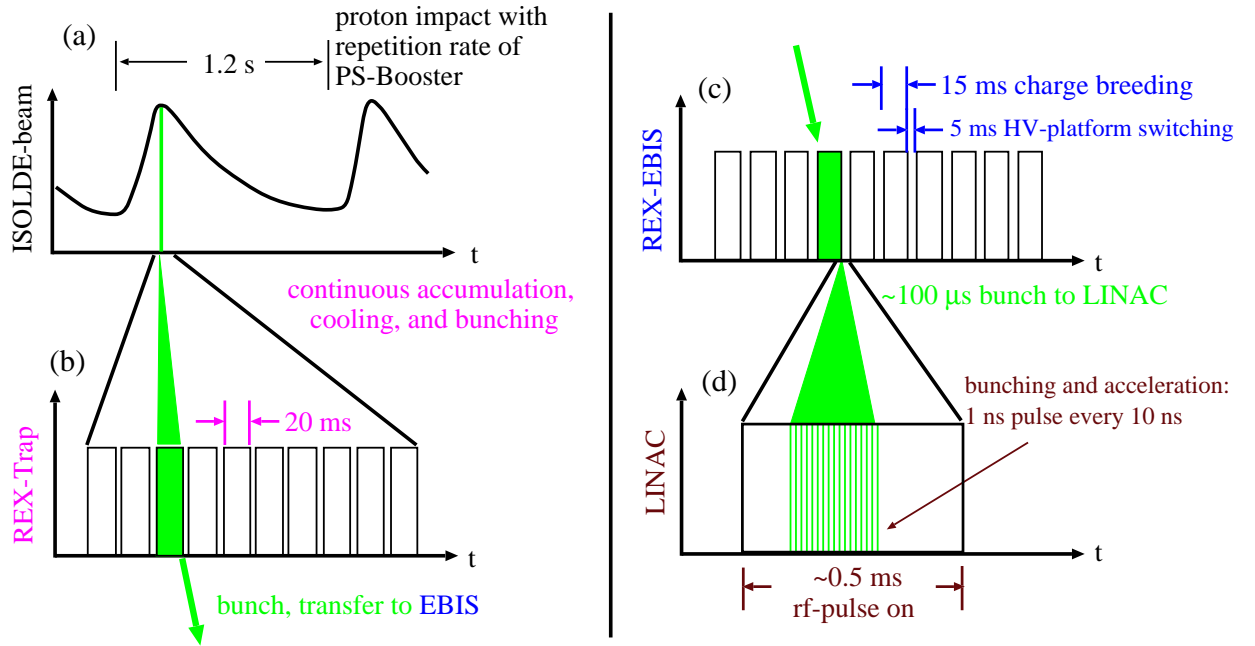


Figure 2.6: REX time structure.

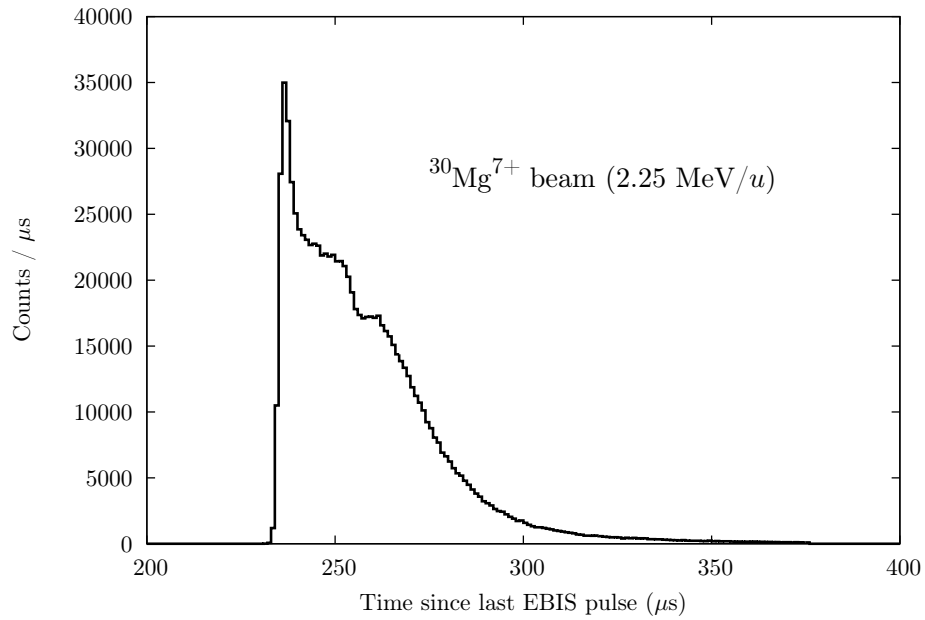


Figure 2.7: Histogram of the arrival time of particles after starting the extraction out of the EBIS. The time offset is arbitrary. Most particles are contained in a short 30 μs wide time window.

formed (panels b, c), which are accelerated with a repetition rate on the order of 20–200 ms. The length of these bunches is about $100\ \mu\text{s}$ (macro structure). There is also a micro structure due to the 100 MHz frequency of most acceleration structures of 1 ns wide bunches every 10 ns, which cannot be observed and is of no consequence (panel d). Figure 2.7 on the preceding page shows the time structure of the pulse released from the EBIS (macro structure). As can be seen the pulse is indeed barely $100\ \mu\text{s}$ long with more than half of the total intensity within a $30\ \mu\text{s}$ time window.

The macro (EBIS) and super (PSB) time structures have consequences. The most important one is the strongly increased instantaneous intensity compared to the average beam intensity. Due to the macro structure the peak of the beam intensity is about a factor of 200-1000 larger than the intensity averaged over one EBIS cycle (see figure 2.7 on the page before). The duty-factor of the PSB is averaged out to some extent by the slow release from the ISOLDE target [62, 66]. In cases of short release times, however, the instantaneous intensity can be larger by a factor of 20 (seen in figure 5.2 on page 74).

Not only is the peak intensity much higher than the average intensity, but also the intensity varies strongly within the EBIS pulse and in-between the PSB pulses. This makes it very difficult to determine the dead time of the data acquisition (DAQ) system, especially since the MINIBALL DAQ consists of several semi-independent sub-systems (see chapter 3). However, the analysis methods used in this work are insensitive to DAQ dead time issues as discussed in section 4.8 on page 64.

These time structures also have certain advantages as they can be exploited to check the consistency of the measured data [55]. Also the beam contamination can be determined based on the known release and decay times (see e.g. figure 5.2 on page 74).

In the future a slow extraction mode out of the EBIS will be implemented which makes the beam profile in figure 2.7 on the page before flatter, reducing the dead time problems.

2.5 Sources of Beam Contamination

As explained in section 2.2 the REX beams are in general not pure; the reason is inherent to the technique used to produce and accelerate these beams. Following the path of the particles from the ISOLDE production targets to the REX accelerator, e.g. in figure 2.2 on page 11), there are three main sources of contamination. The first source is the ISOLDE target itself: in the reactions of the high energy protons with the target material a multitude of different nuclides is produced and only a small fraction of the total yield is of interest. The nuclide of interest is usually selected and separated from the unwanted nuclei in a

two-step process, where first the element of interest is selected and subsequently a mass separator selects the mass (number), so that ideally a pure beam would result. In practice several isobars are extracted, ionized and accelerated.

For instance, in the case of the neutron-rich Mg isotopes under study here the produced radioactive Mg atoms diffuse out of the target and are ionized by the RILIS [65]. While the method very selectively ionizes only Mg atoms, unfortunately surface ionization of other isobars takes place which cannot be completely suppressed. In the present case the (less exotic) Al isobar is the dominant contamination. The Na isobar is also present, but, since it is more exotic, its intensity is negligible. As the mass difference between the Mg and the Al isobars are not large enough to be separated by the mass separator, both Mg and Al beams with the same mass number A and a charge state of $q = +1$ will be produced and undergo the charge breeding and acceleration procedure and will arrive at the MINIBALL target. This contamination can only be decreased with a mass separator that has a resolution on the order of the mass difference between the isobars or by a more selective elemental ionization method.

The second source of contamination is the β decay of the isotope of interest during the trapping and breeding time. For instance, ^{32}Mg has a half-life of 95 ms. During a trapping and breeding time of 32 ms about 21 % of the Mg isotopes will have decayed to Al, which decays further to the longer lived Si isotopes. This contamination is inherent to the charge breeding method and can only be diminished by reducing the breeding and trapping time.

The third source of contamination stems from the EBIS and is due to the presence of residual gas, which is always ionized and copiously extracted (see [11] for an A/q -spectrum). To filter out the ions of interest a mass separator is used with a resolution of about 1 %. Therefore all ions with an A/q within this range of the nominal value will pass the mass separator and will be accelerated. For instance, during one of the first commissioning experiments a $^{30}\text{Mg}^{8+}$ beam was accelerated and, while only 0.4 % naturally abundant, a strong $^{15}\text{N}^{4+}$ component was present in the beam. In subsequent experiments the contamination could be avoided by producing the ^{30}Mg beam with a charge state of $q = +7$. For the $A = 32$ beam produced for the ^{32}Mg beam time a small contamination of the stable nuclide ^{32}S could be identified. For identical A/q values this type of contamination can only be reduced by a cleaner vacuum system of the EBIS. For similar but not identical A/q values in addition an improved resolution of the mass separator after the EBIS can suppress the contaminants more strongly.

Chapter 3

The MINIBALL γ Ray Spectrometer

With the initiation of the REX project it became apparent that new highly efficient experimental equipment was needed at the end of this accelerator to make good use of the rare and expensive radioactive nuclear beams (RNBs). Therefore, the MINIBALL project was started with the aim of designing and building a high resolution and highly efficient Ge γ ray spectrometer optimized for the use with RNBs accelerated at the REX-ISOLDE facility.

In this chapter general considerations concerning γ ray spectroscopy will be laid out in section 3.1. Basic problems encountered in γ ray spectroscopy with the newly available radioactive nuclear beams and their solution will be discussed in section 3.2, while in section 3.3 the main interaction concept is explained. In section 3.4 the main features of the MINIBALL array will be introduced with special focus on the work performed at the MPI-K concerning the development and implementation of algorithms for the analysis of the shape of the Ge detector pulses (section 3.5). Finally, in section 3.6 the standard setup of the MINIBALL array at REX-ISOLDE is introduced. For further details on MINIBALL the reader is referred to [12, 15, 17, 18, 70].

3.1 γ Ray Spectroscopy

Due to the high standards of the experimental techniques and the well developed theory γ ray spectroscopy plays an exceptional role in nuclear structure research. The experiments, which often involve only the electromagnetic interaction of a nucleus with the free radiation field or with electromagnetic fields produced by external charges and currents, yield to a very large extent *model-independent* results, thanks to the fact that the electromagnetic interaction is the best understood of the fundamental interactions in nature.

In particular high-resolution γ ray spectroscopy using beams with energies around the Coulomb barrier is one of the main tools to study the structure of atomic nuclei. Among the most successful techniques are Coulomb excitation well below the barrier, where a complete and fully developed theory exists [71], as outlined in chapter 4 (see also [27, 72–74] and references therein) and few-nucleon transfer reactions [76, 77]. These techniques, which have been developed and used for more than 50 years with stable beams, experience a revival in recent years due to the availability of re-accelerated beams of exotic nuclei far from stability to address the problems and issues discussed in chapter 1.

For the adaptation of these γ spectroscopic tools to the study of exotic nuclei not only re-accelerated beams of exotic nuclei with energies around the Coulomb barrier are needed, but two eminent problems have to be overcome:

- due to the usually very low intensity of these beams γ rays have to be detected with the highest efficiencies and
- as the experiments are performed in inverse kinematics the γ emitting nuclei are the projectiles or are projectile-like, moving with a high velocity on the order of 5–10 % of the speed of light. This results in large Doppler shifts of the γ ray energies and large Doppler broadening, compromising the main advantage of Ge arrays: their unsurpassed energy resolution.

The resolving power, however, i.e. the ability to separate individual γ rays by their energy from a large number of others simultaneously emitted is not crucial while a high efficiency is of primary importance for experiments with RNBs. In such experiments the beam intensities are very low and only reactions with high cross sections can possibly be used to study them. These reactions result in the emission of only a few (< 5) γ rays.

The solutions to each of these problems hamper each other to some extent. On the one hand, to obtain the highest efficiency ideally large-volume high-purity Ge detectors should be used positioned very close to the target. In 1995 the cluster detectors [78], later to be deployed as part of the EUROBALL array [79], were available and it was decided to carry out several experimental campaigns at the MPI-K and at GSI with them using a setup that achieves the highest possible γ efficiency. The setup became known as the Cluster Cube, where six cluster detectors were placed according to the six sides of an imaginary cube surrounding the target chamber. A picture of the setup in Heidelberg is shown in figure 3.1 on the next page. The results obtained (e.g. [80]) convincingly demonstrated the high potential of small, compact and highly efficient γ ray arrays. However, the achieved granularity was quite limited and only poor Doppler correction was possible in some cases.

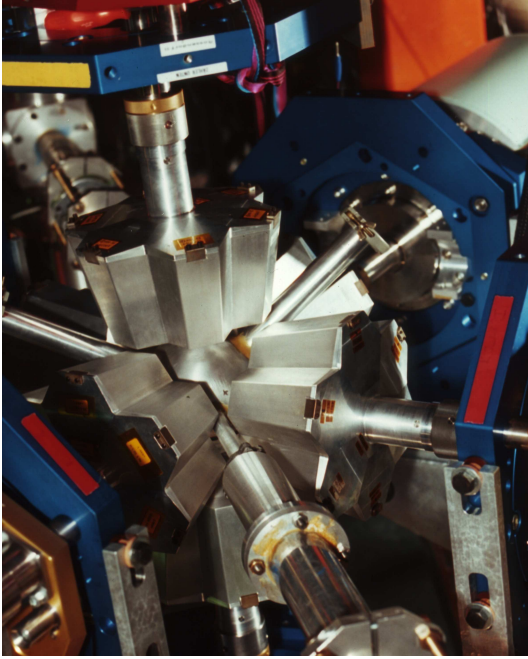


Figure 3.1: EUROBALL Cluster Cube setup at the MPI-K in Heidelberg in 1995. The arrangement of the EUROBALL cluster detectors in a cube like setup resulted in an enormous efficiency of nearly 20 %. The drawback is the poor granularity, which resulted in very strong Doppler broadening, especially if such a setup would be used with exotic beams in inverse kinematics. This problem is overcome by the MINIBALL array as described below.

On the other hand, in order to reduce the Doppler broadening the solid angle subtended by an individual detector should be kept as small as possible to achieve good angular resolution. One possibility is to place the detectors far from the target and either increase their numbers (and cost) or accept a correspondingly lower efficiency. However, the requirements of high efficiency and high granularity at reasonable cost can best be fulfilled by the application of the new technology of position sensitive Ge detectors. Here the outer electrodes of the individual Ge crystals are segmented resulting in an increased position resolution. This technology is employed by the arrays of the Belgian-German(-British) MINIBALL [12, 70, 81] and the French-British EXOGAM [82] projects, which were initiated at the end of the last century in view of the expected availability of low-energy RNBs at REX-ISOLDE (chapter 2) and at the SPIRAL facility [8], respectively. The advantage of the MINIBALL array, which is equipped with a purely digital electronics after the pre-amplifier, is, besides a higher segmentation, that pulse shape analysis (PSA) is used to further refine the interaction position within each segment.

3.2 Doppler Shift and Broadening

The experiments with radioactive beams are performed in so-called inverse kinematics, which means that the nucleus to be studied is either the beam particle itself or near to it in terms of proton and neutron number. After the reaction, such a nucleus essentially

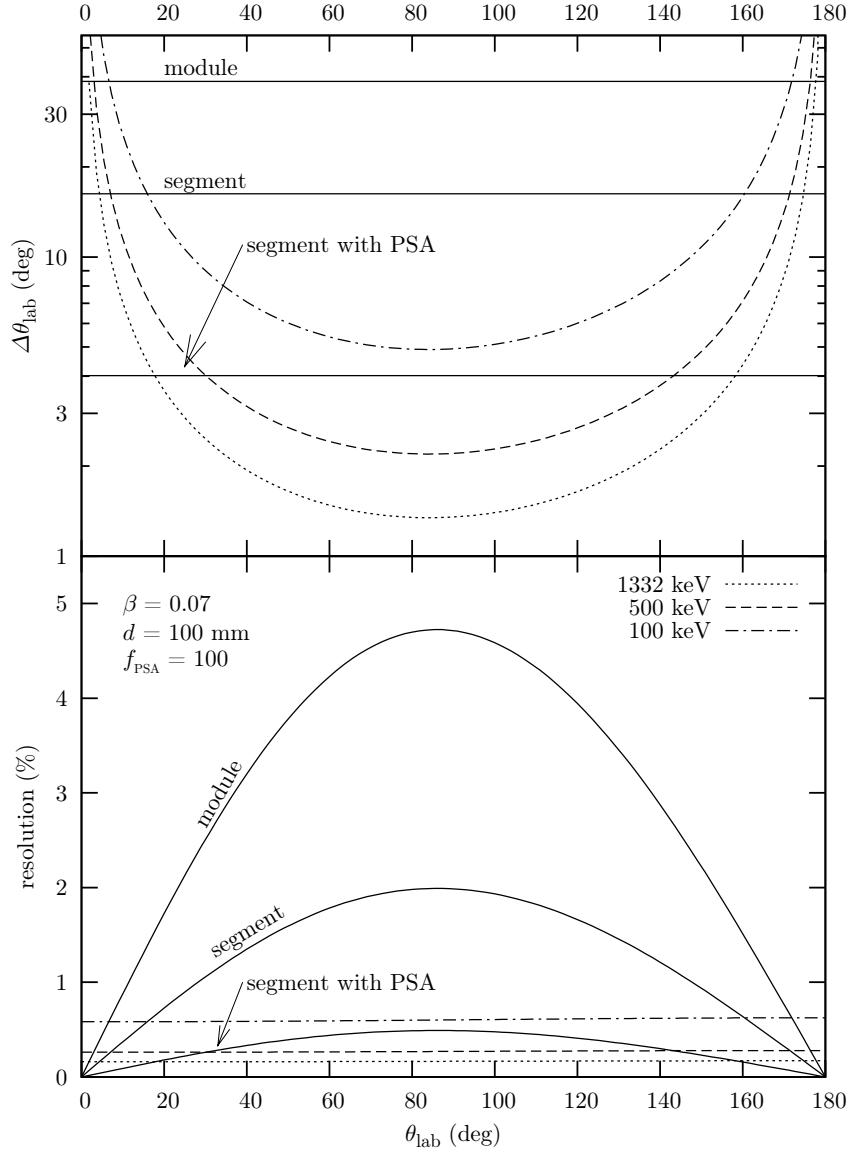


Figure 3.2: Resolution and granularity in a typical MINIBALL setup. The lower panel shows the resolution (FWHM) due to the Doppler broadening calculated according to 3.2 on the next page as a function of the angle θ between the γ ray and the velocity of the emitting nucleus in the laboratory (solid lines). The three curves show the resolution obtained assuming the opening angle of an unsegmented MINIBALL detector, of a segment, and of the PSA position resolution, respectively. For comparison the intrinsic resolutions are shown for the indicated energies (non-solid lines). The upper panel shows the effective θ resolution needed to match the intrinsic resolution of the Ge detectors. The horizontal lines show the θ resolution (i.e. the (effective) opening angle) of a MINIBALL module, a segment, and a PSA position resolution. The values assumed for β and the distance of the detectors from the target d are indicated in the figure, as well as the assumed increase in granularity when PSA is used, f_{PSA} .

moves with a velocity that is near the velocity of the incident beam, i.e. on the order of 6–8 % of the speed of light for REX. Thus, the γ ray energy is Doppler shifted considerably, as can be seen from the relation between the photon energy in the laboratory frame and the frame of the γ emitter, $E^{(0)}$ and E_{lab} , respectively

$$E^{(0)} = \gamma E_{\text{lab}} (1 - \beta \cos(\theta_{\text{lab}})) ; \quad (3.1)$$

θ_{lab} is the angle between the velocity vector (with magnitude β) of the emitter and the direction of the γ ray, (see also figure 3.3 on the following page). The factor γ is the usual relativistic expression $\gamma = 1/\sqrt{1 - \beta^2}$. Since the angle θ_{lab} can only be measured with a certain precision $\Delta\theta_{\text{lab}}$, the measured γ ray energy in the laboratory shows an uncertainty of ΔE_{lab} given by

$$\frac{\Delta E_{\text{lab}}}{E_{\text{lab}}} = \frac{\beta \sin(\theta_{\text{lab}})}{1 - \beta \cos(\theta_{\text{lab}})} \Delta\theta_{\text{lab}} . \quad (3.2)$$

Assuming that the velocity vector $\vec{\beta}$ of the emitting particle is known exactly, the opening angle of the γ detector determines $\Delta\theta_{\text{lab}}$. Due to this uncertainty the peaks in the γ ray energy spectra are Doppler broadened, even after correction for the average Doppler shift. This is illustrated in figure 3.2 on the preceding page, which shows the expected γ ray energy resolution as a function of θ (lower panel) and the required granularity $\Delta\theta$ to match the intrinsic resolution for a given γ ray energy (upper panel).

3.3 The Main Interaction Concept

All position sensitive Ge γ ray detector arrays that do not perform tracking (see e.g. [83, 84]) rely on the so-called main interaction concept. It is important to recall that usually many interactions (photo effect, Compton scattering, and pair production) of a γ ray in the detector volume are needed to deposit its full energy (FE) resulting in a full energy event (FEE). With current detectors it is not possible to separate different interactions, e.g. on the basis of time differences, and the overall detector signal is therefore dominated by the main interaction (MI) where most of the energy was deposited. The information on the direction of the incident γ ray, needed to correct for the Doppler shift, can be obtained only from the first interaction (FI), however, as illustrated in figure 3.3 on the following page. The main interaction concept relies on the fact that for all FEE the MI is in most cases identical or very close to the FI and no severe degradation of the Doppler correction is expected by not identifying it [13–15].

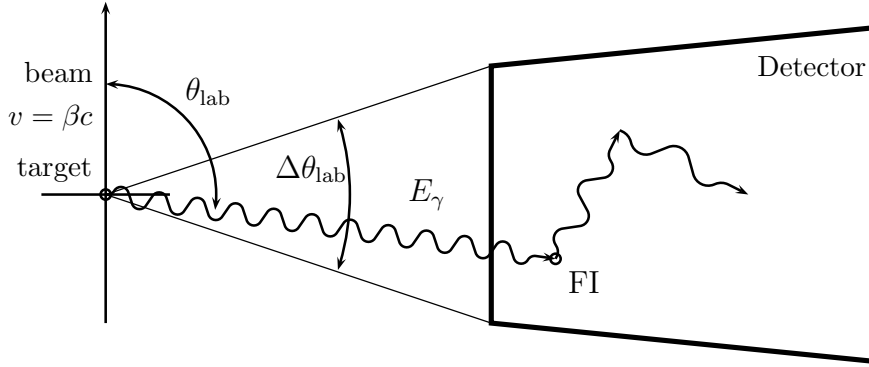


Figure 3.3: Schematic detector setup. The opening angle of the detector $\Delta\theta$ the angle θ of the γ ray with respect to the velocity vector of the emitting particle and the first interaction (FI) are indicated.

This is illustrated in figure 3.4 on the next page, where several probabilities are shown. In the panels above the plot the corresponding situation is schematically displayed. The dot-dashed curve shows the probability that the FI and MI are identical (panel (a)). For energies around 300 keV this probability can even drop below 50 %. Since the expected final position resolution is on the order of 5 mm, no problem occurs if the MI and the FI are separated by this distance (panel (b)); the probability, shown by the dashed curve, is already improved. Since the exact three-dimensional location of the FI is not of interest, but only its projection on the two-dimensional detector front face toward the target, defining the direction of the incident γ ray, a location of the MI within the hatched region in panel (c) is acceptable. This probability is shown by the solid curve. Therefore, for most energies the MI is a very good approximation for the first interaction.

Depending on the γ ray energy there is a different reason for this. For low energies (< 200 keV) photo absorption dominates and the FI is the MI. At very high energies (> 2500 keV) pair production dominates and the kinetic energies of the created electron and positron are larger than their mass and the FI is again identical to the MI. At energies in-between it is important to recall that only FEE are considered. Here the first interaction is likely to be a Compton event and the deposited energy ΔE_γ depends on the deflection angle θ

$$\Delta E_\gamma = \frac{1 - \cos \theta}{1 - \cos \theta + \frac{m_e c^2}{E_\gamma}} E_\gamma, \quad (3.3)$$

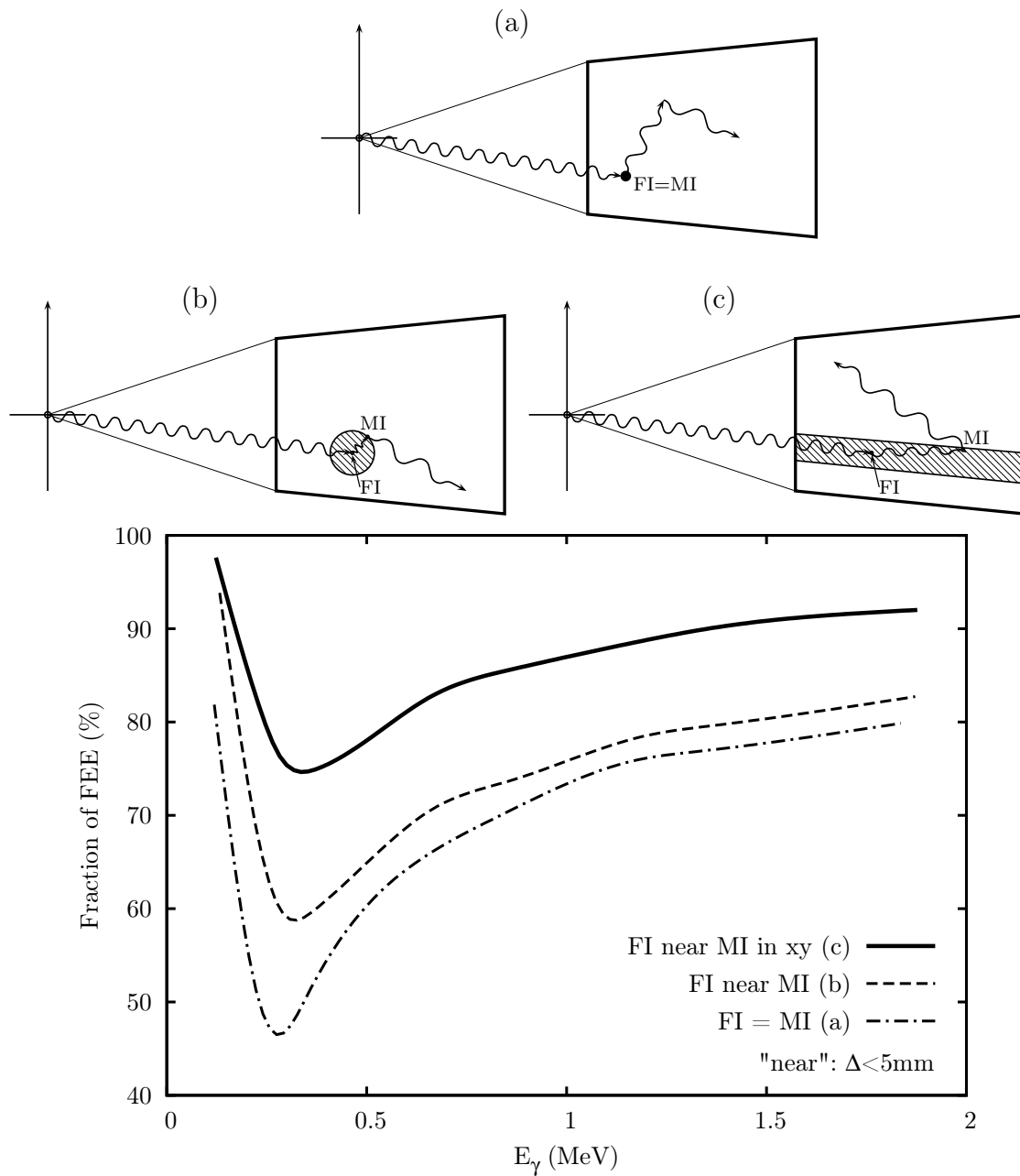


Figure 3.4: Fraction of full energy events (FEE) where the main interaction (MI) is equal to the first interaction (FI) (dash-dotted line), fraction of FFEs where the MI is located within a radius of 5 mm within the FI (dotted line) and fraction of FFEs where the MI is located within 5 mm of the FI when projected onto the detector surface toward the target position (solid line). The latter curve takes into account that the measured direction of the γ ray is reconstructed correctly if the FI and MI differ in position only along the line toward the target. In most cases the MI is therefore a very good approximation to the FI. This is the result of a GEANT simulation for the MINIBALL array [13].

where m_e is the mass of the electron and c is the speed of light. Therefore if

$$\theta > \arccos\left(\frac{m_e c^2}{E_\gamma} - 1\right) \quad \text{for } E_\gamma > \frac{m_e c^2}{2} = 255 \text{ keV} \quad (3.4)$$

the FI is equal to the MI. For smaller angles this might not be the case, but as the angles are small the γ ray, after scattering, travels with nearly the same direction and the next interaction is likely to occur in the region indicated in panel (c) of figure 3.4 on the preceding page.

Another reason is that the mean free path of a γ ray with an energy of more than 1 MeV in Ge is larger than the crystal size. The chances to fully deposit its energy are rather meager, unless a substantial fraction is deposited in the FI.

3.4 The MINIBALL Array

The developments necessary to realize the MINIBALL array covered all parts of the spectrometer: the encapsulation technology[85] had to be extended to segmented detectors, which had to be developed, a new cryostat capable of coping with the additional cabling required for segmented detectors was needed, as well as new pre-amplifiers transmitting the pulse shape as accurately as possible, new digital electronics to perform the PSA in real-time and a flexible support frame. In this section some of these aspects will be discussed in detail, especially those involving work performed at the MPI-K; for others the relevant references will be given.

3.4.1 Specifications

With the start of the MINIBALL design and construction project the physics opportunities with so-called Ge *Mini(-ball)* Arrays were assessed during a workshop at the MPI-K in 1995 [86]. The main interest in the study of exotic nuclides lies in the study of their low-lying levels and therefore only low-multiplicity ($M_\gamma < 10$) γ cascades have to be coped with. A new array should therefore be optimized with respect to full-energy efficiency rather than resolving power, which is the ability of an array to energetically resolve different γ rays detected simultaneously. The following design criteria were put forward:

- A full-energy peak efficiency of $> 10\%$ for a γ energy of 1 MeV at the most compact detector arrangement should be reached.

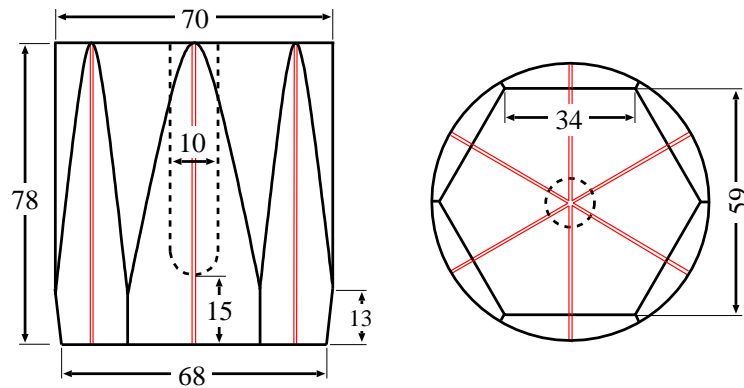


Figure 3.5: Geometry of the MINIBALL crystal. The central electrode is shown by the dashed curves. The electric segmentation lines are also indicated. The dimensions are given in mm and should be considered approximate as each individual crystal differs slightly in size.

- For beam velocities of up to $\beta = 0.1$ the Doppler-broadening¹ should be less than 1 % of the energy of the γ ray.
- The successful encapsulation technology and the semihexaconical shape of the EUROBALL cluster modules [78] should be used.
- In order to achieve the necessary granularity a six-fold segmentation of the outer contact was to be used.
- The array should be equipped with digital sampling electronics.
- An adjustable support frame should be developed and built.
- The array should be able to cope with high event rates in excess of > 10 kHz per detector module (crystal).
- All parts should be optimized for the use at REX-ISOLDE, but flexible enough to be used elsewhere.

3.4.2 The MINIBALL Module

The shape of the MINIBALL Germanium modules corresponds to that of the EUROBALL cluster modules [78] and is shown schematically in figure 3.5. In addition, due to the

¹Doppler broadening is the Doppler-shift related contribution to the energy resolution (see section 3.2 on page 21).

throughout positive experiences with the encapsulation technology for the EUROBALL cluster detectors it was early decided to employ it also for the MINIBALL modules [70, 78]. The modules have a semihexaconical shape tapered to a focus distance of 43 cm, the nominal target distance in the EUROBALL setup. While this geometry is not optimal for a target-detector distance of only 10 cm, which was the minimum distance envisaged for MINIBALL, it was nevertheless not altered for several reasons: MINIBALL was designed to be flexible, so there was no optimal distance; the EUROBALL detectors with their Aluminum encapsulation were already developed and routinely produced by EURISYS [87]; a modification of the shape would have required long development and testing cycles. In addition, the mechanical compatibility to the original EUROBALL modules was felt to be advantageous also for the design and construction of new cryostats [78], which then could also house the “old” not-segmented EUROBALL modules. It was therefore decided to restrict the development directly concerning the Ge detectors to the already challenging electric segmentation of the outer contact. The main tasks were the electric insulation of the outer contact(s) from the Al encapsulation can, the segmentation itself and the modification of the lid to allow for six additional signal feed troughs. A first prototype two-fold segmented detector was delivered to the MPI-K in 1995 and the results of extensive testing [13] were used to develop the six-fold segmentation for the MINIBALL modules.

The detectors are made of n -type high purity Germanium (HPGe) with impurity concentrations around 10^8 cm^{-3} [15], requiring positive high voltages between 3 kV and 4.5 kV applied to the central electrode. At these voltages almost the full volume of the detectors is sensitive to γ ray irradiation. Furthermore, even though the magnitude of the electric field changes considerably throughout the detector volume the drift velocity of the charge carriers is nearly constant, which is important for the analysis of the detector pulse shapes.

In the fabrication process the segmentation is achieved by employing masks during the implantation of the outer surface with boron to create the outer contacts. These masks leave regions of about $100 \mu\text{m}$ width which are not implanted and therefore not contacted. This causes the electric separation of the six segment contacts.

The Aluminum can, into which the detector is inserted, has a wall thickness of 0.7 mm and the crystal is separated by a distance of 0.7 mm from the capsule wall. In figure 3.6 on the next page the arrangement of can, detector and lid is schematically shown. For details concerning the support, fixation, and electric insulation of the Ge crystal inside the Aluminum can the reader is referred to [70]. Photographs of the modules can be seen in figure 3.7 on the facing page.

The detector modules were extensively simulated [13, 15] including the energy deposition, the signal generation on the detector electrodes, and the effects of the pre-amplifier

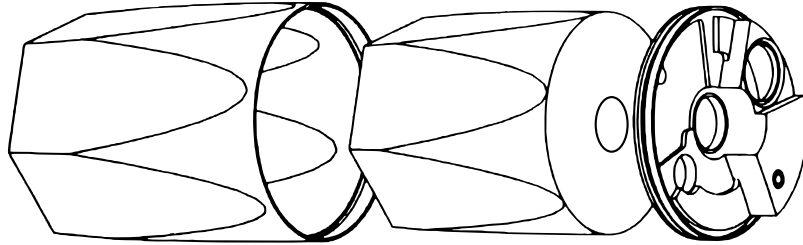


Figure 3.6: Schematic view of a MINIBALL module with Al can and lid.

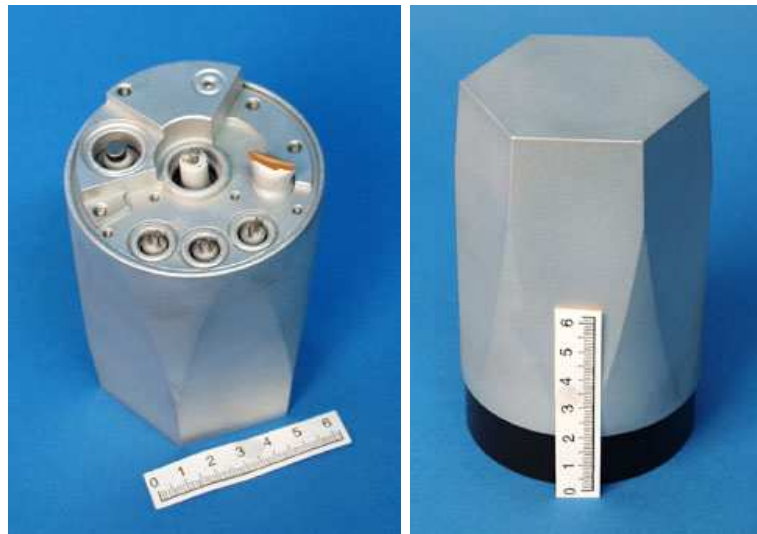


Figure 3.7: Pictures of the MINIBALL capsule. In the pictures only the Aluminum encapsulation can be seen; the actual Ge crystal is contained within. On the left picture the central high voltage and signal feed-through and three pairs of segment signal feed-throughs are visible. The actuator for the ion getter and the sealed vacuum flange can be seen as well.

and the sampling electronics. The main findings were:

- The electric field inside the detector volume (due to the applied high voltage) varies considerably in the range from about 750 to 2000 V/cm². The drift velocity of the electrons and holes is nevertheless nearly constant with a value of about 1 cm/100 ns.
- The calculated weighting fields of the core contact show that the steepest-slope algorithm [14] can be used to determine the radial position of the interaction by pulse shape analysis.
- The calculated weighting fields of the segment contacts show that one can determine the azimuthal interaction position within a segment by pulse shape analysis.

Details concerning the last two points are given in section 3.5 on page 37.

3.4.3 The MINIBALL Cluster Detector

While it was originally planned to build septuple cryostats to achieve a similar setup as was used for the Cluster Cube campaign (see section 3.1 on page 19 and figure 3.1 on page 21), it was decided to design and build a new and compact cryostat for MINIBALL. The main reasons for doing so are

- the weight of the detectors: they should be bearable by one person without a crane or other support,
- the increase in the number of channels: with a triple or quadruple cryostat “only” 21 or 28 signal channels had to be dealt with, and not 49,
- the alignment of the detector axis with the target position: the detectors of a triple or quadruple cryostat are pointing more directly toward the target position than in a septuple cryostat, and
- the greater flexibility an increased number of cryostats offers: special configurations, such as detectors grouped around forward and backward angles for Doppler line shape measurements or setups for angular correlation measurements, can more easily be realized.

The new cryostat was designed and built by CTT [88] in collaboration with the IKP, Cologne [70]. Due to its modular design the cryostat can house either three or four six-fold



Figure 3.8: Picture of the quadruple cryostat head.

segmented detectors together with their pre-amplifier electronics. To change the configuration only the end-cap (in figures 3.8 and 3.9 on the next page the quadruple and triple end-cap, respectively, can be seen) and the cold detectors support have to be changed, while the cabling, vacuum feed throughs, cryostat mechanics and the electronics can remain unchanged. The cryostat features a high cooling power through improved thermal contact and conductivity between the detectors and the liquid nitrogen dewar and reduced microphony due to a new flexible support of the detectors. The cryostat can not only cool the detectors to their operational temperature below 100 K, but it can also compensate for the power consumption of the cold part of the pre-amplifier, the field effect transistor (FET), with about 50 mW per channel. The dewar has a capacity of 2.7 l and needs to be refilled roughly every 12 hours when the pre-amplifiers are powered up (for the triple version).

The (warm parts of the) pre-amplifiers (up to 28) are plugged into motherboards housed inside the pre-amplifier block below the dewar (indicated in figure 3.9 on the following page). The cables to facilitate an electric connection between the cold and the warm part of the pre-amplifiers are routed in a special fixture along the cold finger of the cryostat. During the commissioning of the first cluster detectors no oscillations or drift of signals were observed, validating the good design of the cryostat. Cross talk, however, was initially observed and only due to the encapsulation technology was a fast trial-and-error procedure possible which reduced it to an acceptable level, i.e. below 0.01 %, which is the lowest cross talk that can be measured [70].

3.4.4 The MINIBALL Electronics

In order to fully exploit the capabilities of the segmented detectors the MINIBALL collaboration decided to follow a radically new approach: instead of the standard analog

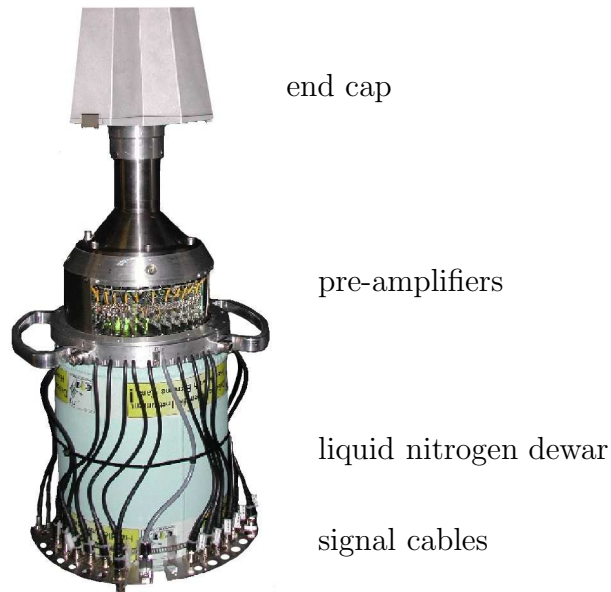


Figure 3.9: Picture of a MINIBALL triple detector.

electronics so far employed for similar detector arrays, a fully digital² electronics system should be used. In contrast to conventional electronics, here all trigger, energy, timing and position information is derived from the digitized pre-amplifier pulses of the core and segments. While similar electronics was used already for several years in high-energy physics experiments this was the first time that such a system was employed for a Germanium γ ray spectrometer with its extreme requirement on the energy resolution. The differences between a standard analog and a digital system are displayed in figure 3.10 on the next page.

Pre-Amplifier

In order to house up to 28 signal channels in the MINIBALL cryostat and to fulfill the strict requirements on the output signal a new pre-amplifier was developed—based on an initial development at the MPI-K in Heidelberg—at the IKP in Cologne. The new pre-amplifier should have a large bandwidth and should reproduce the true signal as close as possible, i.e. without the over- and under-shots commonly observed in standard commercial systems. Indeed, while for the latter these artefacts are of no concern, as the energy resolution is not sensitive to them, the pulse shape analysis proposed for MINIBALL is.

The developed pre-amplifier has resistive feedback with a decay time of $50 \mu\text{s}$ and a

²after the pre-amplifier

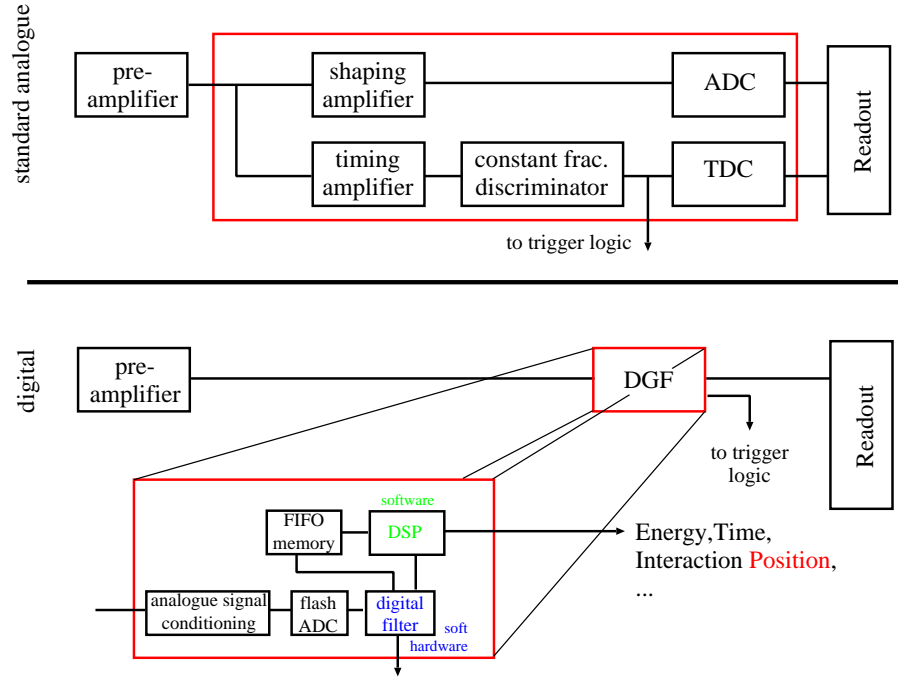


Figure 3.10: Schematic comparison of analog and digital electronics.

rise time of $15 \text{ ns} + C \cdot 0.3 \text{ ns/pF}$, with C the capacitance of the detector, which comes to about 40 ns ; the integration time is 16 ns [70]. The physical size of the pre-amplifier is $40 \times 25 \text{ mm}^2$. It is possible, and done for MINIBALL, to separate the pre-amplifier into a cold and warm stage. The most (noise) sensitive part of the pre-amplifier, the FET, is located as close as possible to the detector, i.e. directly on the Aluminum capsule, to obtain an optimum energy resolution. The main board of the pre-amplifier is operated at room temperature. All electric contacts (signals from the cold stage of the pre-amplifier, $\pm 12 \text{ V}$ supply voltage, ground and output signal) are plug-and-socket connections so that a broken module can be changed quickly and easily. There are adjustments for pole zero, DC offset, and the drain current of the FET.

The analog part of the electronics is schematically shown in figure 3.11 on the following page. While the segment electrodes are directly connected to their respective contacts, a capacitor is needed to separate the signal of the core contact from the detector high voltage.

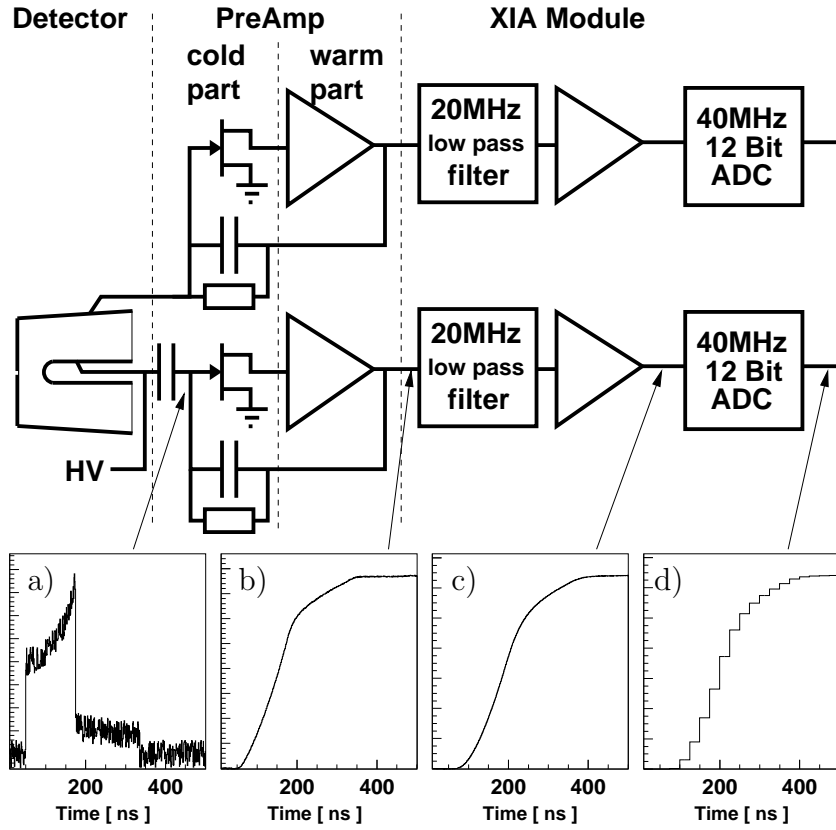


Figure 3.11: Analog part of the MINIBALL electronics (plus the flash ADC; from [15]). Only one of the six segment channels is shown. In the lower part of the figure typical signal shapes are shown at the corresponding places in the diagram above, which correspond to a) the current signal of the detector, b) the charge signal after the pre-amplifier, c) the charge signal after the low-pass filter, and d) the digitized charge signal.

The DGF-4C Module

For the digital electronics a commercial solution was adopted [89], which was the only possibility at the time fulfilling most of the requirements listed in section 3.4.1 on page 26. The 4-channel single-width CAMAC module DGF-4C³ is shown in figure 3.12. A block diagram is shown in figures 3.10 and 3.11. The analog signal is first adapted to the range of the analog-to-digital converter (ADC) via a gain and offset adjustment with 14 bit precision. To remove so-called signal “ghosts” the signal passes through a Nyquist filter, which removes high frequency components. The ADC has a resolution of 12 bit and operates as well as all other digital components on the card, with a frequency of 40 MHz.

³Digital Gamma Finder, 4 channel Camac

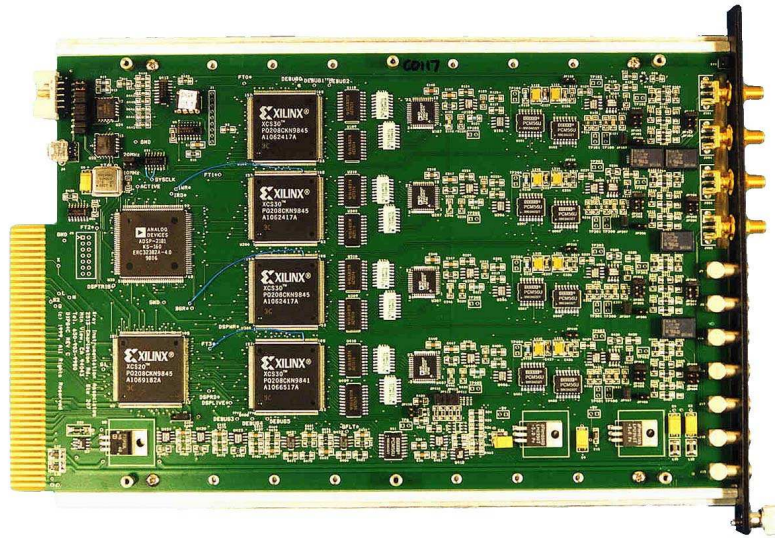


Figure 3.12: Picture of a XIA DGF-4C card. The signal inputs can be seen on the right.

The digitized samples are first processed by a field programmable gate array (FPGA) (one for each channel) and simultaneously stored in a first-in-first-out (FIFO) memory for further processing. In case a signal is detected, the content of the FIFO is copied and made available to a digital signal processor (DSP) (one common DSP for all 4 channels) where algorithms too complicated and too resource intensive for the FPGA are executed. While it is also possible to read out the full signal trace to a host computer, during operation the signal shape is analyzed on-line in real-time on-board the DGF4C card and only few parameters are actually read out, as otherwise the requirement of high-rate capability could not be fulfilled. More details on the implementation and performance of the PSA code can be found in [17, 18].

DAQ system

In this section a short introduction to the basic features of the MINIBALL data acquisition (DAQ) system will be given. It will focus on certain particulars of the MINIBALL DAQ system that are unusual for typical DAQ systems employed in nuclear physics experiments so far.

One point has already been discussed above, namely the use of digital electronics for the MINIBALL detectors. Besides the advantages discussed above there are others. Not every event has to be read out immediately as the RAM on the DGF-4C is large enough to store several events with all the necessary information (time stamp, energy, time, PSA

parameters, etc.) on-board. With the time structure of the REX beam (section 2.4 on page 14) the data can essentially be read out in a dead time free mode: during the about $100\ \mu\text{s}$ long beam pulse all data is stored on the cards and only after the beam pulse, in the about 20 ms long time span without beam, the data is read out and the DAQ system is ready for the next beam pulse.

Not all detectors used in MINIBALL experiments with REX at CERN were equipped with digital electronics. Since for these channels no time stamp would be available a correlation, e.g. between particle and γ rays, would be impossible. A possible event-by-event readout would reduce the advantages mentioned above; in fact only one event per beam pulse could be read out, as the dead time during readout would far exceed the length of the beam pulse. The ADCs (TDCs) used, however, can store up to 30 events on-board. By feeding the gate (stop) signal into a spare DGF channel a time stamp for these event was generated.

The first step of the off-line analysis is the reconstruction of physical events by associating individual detector events taking place within a certain time window (typically $4\ \mu\text{s}$) and then the usual analysis steps (calibration, sorting, etc.) are performed [55, section 3.5].

3.4.5 The MINIBALL Support Frame

While typically rigid frames were used for 4π spectrometers, with fixed positions for the individual detectors, for MINIBALL an adjustable frame was designed and built (visible in figures 3.13 on the next page, 3.22 on page 48 and also in the foreground of figure 2.5 on page 14). As MINIBALL will be used at different laboratories for a wide variety of experiments this mechanical flexibility is a necessity, as e.g. a change from a 2π to a 4π configuration can quickly be realized.

The frame consists of 6 semi-circular arcs along which the detectors (up to three per arc) can be moved with the detectors always pointing to the center of the target chamber. Each arc is supported at the upper and lower end such that it can be rotated around the vertical axis passing through the center of the target chamber. Two halves of the frames can be moved perpendicular to the beam axis by about one meter to either side to allow easy access to the target chamber and to simplify the mounting of the detector onto their holders attached to the arcs. Furthermore, each detector can be moved radially toward or away from the target position and can be rotated around its axis. This structure was designed and built by a collaboration of the University of Cologne, IRES Strasbourg and the University Göttingen. For further details see [12, 15, 70].

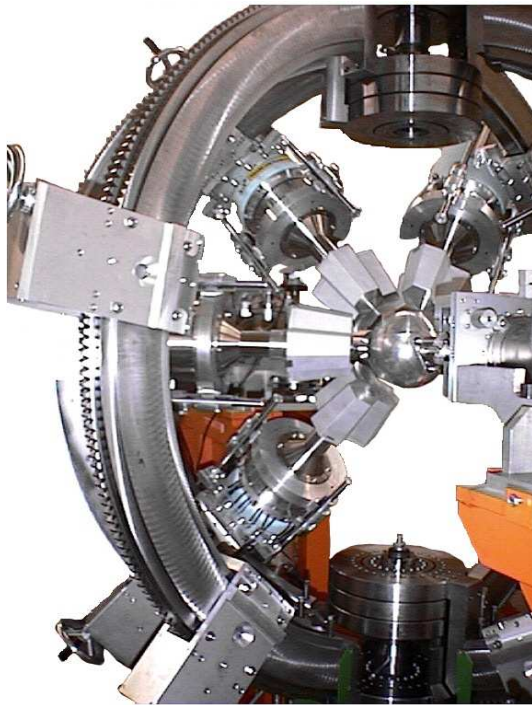


Figure 3.13: Picture of the MINIBALL frame with four detectors installed (2002 at the IKP in Cologne).

3.4.6 Efficiency

The efficiency of the MINIBALL array as a function of E_γ is shown in figure 3.14 on the following page as measured in the Sept. 2004 experimental campaign (see chapter 5 on page 71 and [55]), where eight triple clusters were operational and mounted near 60° and 120° with a distance to the target of 9 cm. The efficiency depends strongly on the chosen MINIBALL configuration and the curve shown in the figure does not apply generally; it is only an example.

3.5 Position Sensitivity and Pulse Shape Analysis

In order to extract the interaction position from the detector signal, essentially two steps have to be taken. First the distribution of the energies on the core and segment signals is analyzed and second, when the segment with the largest charge (or energy) deposition is identified the detailed shape of the current pulse is analyzed. While the height of the charge signal at the core electrode is proportional to the energy deposited in the full crystal (as in a conventional detector) the charge signal measured at the segment contacts allows to measure the energy deposited in each of the triangular shaped segments. Once the segment with the largest energy is identified, localizing the main interaction in that segment, the

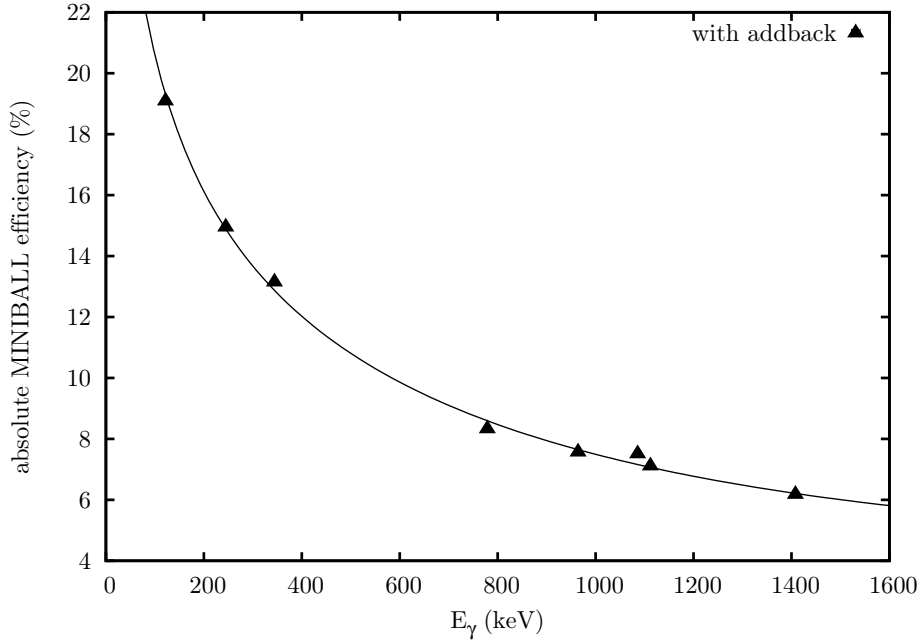
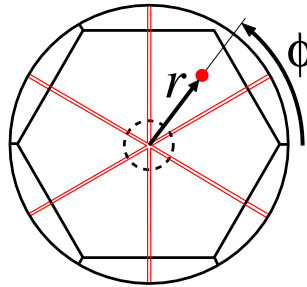


Figure 3.14: MINIBALL efficiency with eight triple clusters in closest configuration. A ^{152}Eu source was used for its determination.

detailed shape of the core signal as well as that of the neighboring segment signals can be analyzed. Doing so results in an increase of the granularity of the detector by determining on an event-by-event basis the (r, ϕ) coordinates (see figure 3.15) of the main interaction. Please note that with the six-fold segmented detectors no information on the interaction depth, i.e. position in longitudinal direction along the detector axis, can be obtained. As the γ radiation is in general not incident perpendicularly to the detector front face, the missing information on the interaction depth is taken from a simulation [15, 16, 18].

Figure 3.15: Definition of radius r and azimuth ϕ which can be extracted from the pulse shape analysis of the core and segment signals. The angle within one segment is designated a φ .



3.5.1 Pulse Generation

In order to understand the algorithms for the (r, ϕ) determination, explained in sections 3.5.2 and 3.5.3, the signal generation on the segment and core electrodes after energy deposition shall be shortly reviewed here.

When energy is deposited in the crystal a number of majority and minority charge carriers, i.e. electron-hole-pairs, are produced in the Ge semi-conductor. The electric field due to the applied high voltage separates these charges before they can recombine and (in case of the MINIBALL detectors) the electrons and the holes drift with a nearly constant velocity to the central core and the segment contacts, respectively. While these charges are drifting, image charges on the electrodes are influenced. As the speed of the drifting charges is much slower than the speed of light the whole system, consisting of the drifting majority and minority charge carriers *and* the influenced image charges on the electrodes, obeys the electrostatic Maxwell equations, i.e. essentially the Poisson equation with certain boundary conditions. As the charges are drifting inside the detector the image charges on the electrodes are changing constantly, giving rise to the detector signals.

These currents can be calculated with the help of the so-called “Weighting field”. It was numerically determined for the MINIBALL detector modules at the MPI-K [14, 15] and the results obtained are summarized in sections 3.5.2 and 3.5.3.

3.5.2 Determination of r —The Steepest Slope Method

The magnitude of the weighting field of the core electrode as a function of the radius r is shown in figure 3.16 on the following page for the infinitely long true co-axial detector with inner and outer radius of 5 and 35 mm, respectively. The most prominent feature is the steep rise close to the central core contact, which means that any charge drifting toward this electrode will cause a very steep rise of the current just before it reaches the contact. This is shown in figure 3.17 on page 41 for an assumed interaction at $r = 15$ mm. The contribution to the total current signal (c) from the electrons (a) and holes (b) as a function of time since the interaction (shown on the top x -axis on all plots) is displayed by the solid, dot-dashed, and dashed lines, respectively. A constant drift velocity of the charge carriers of 0.1 mm/ns was assumed. The current contributions of both types of charge carriers have the same polarity as they do not only differ in sign but also in drift direction, i.e. the product of charge q , weighting field \vec{E}_w , and velocity \vec{v} have the same sign. From panel (c) it is apparent that the steep drop in the current occurring at $t = 100$ ns is indeed a strong signature that should be discernible even under not optimal conditions. Therefore,

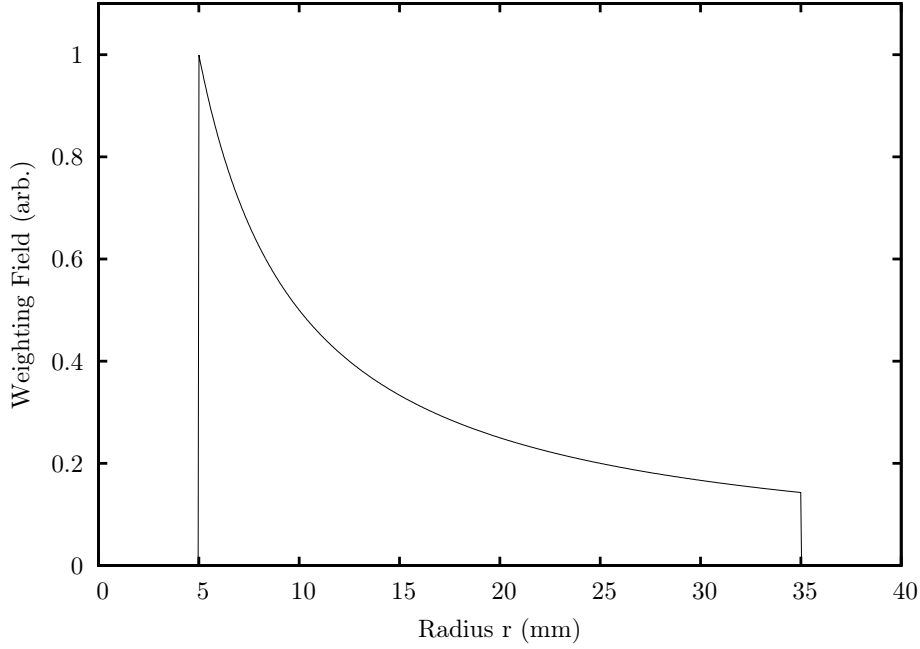


Figure 3.16: Weighting field of the central contact of an infinitely long true co-axial detector as a function of r . Apparent is the steep rise close to the central contact at $r = 5$ mm. The outer contact lies at $r = 35$ mm.

in order to infer the radius r of the interaction (see 3.15 on page 38) the time from the start of the pulse until the drop in the current signal has to be determined. In a realistic situation with finite bandwidth this drop should still be perceptible as the *steepest slope* of the current signal [14].

A full simulation of the true geometry and measurements confirmed the above for the MINIBALL modules to a large extent⁴. This is shown in figure 3.18 on page 42. In the four panels a–d the (idealized) current of the core $I_c(t)$ (a), the digitized charge signal $Q_c(t)$ (b) and the first (c) and second (d) derivative of the charge signal $I(t) = \Delta Q(t)/\Delta t$ and $\Delta I(t)/\Delta t$, respectively, are shown. In panel (c), showing the reconstructed current signals, their steep drop, when the electrons reach the core contact (indicated by the vertical lines), is still visible. By searching for the time when the slope of the current (d) has a minimum the drift time of the electrons is measured and thereby also the radius of the interaction. In panels (e) and (f) the results of measurements with a collimated γ source of 662 keV (perpendicular irradiation), with a MINIBALL module using the DGF-4C as ADC card are shown [70]. In panel (f) histograms of the measured steepest-slope times are plotted for different radial positions of the collimated γ -source. The resolution

⁴Deviations to this picture are due to the non-coaxial front part of the detector.

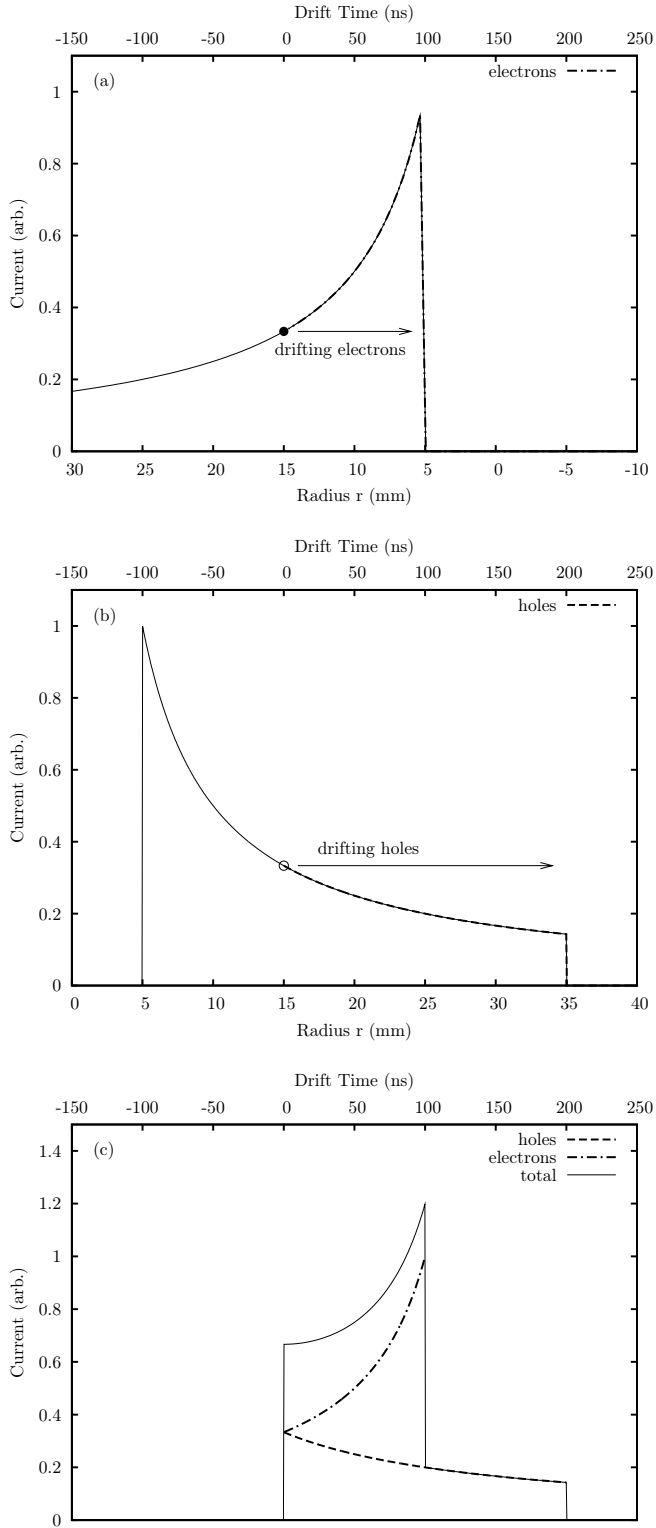


Figure 3.17: Composition of a current signal. All three plots have the same time scale (upper x -axis). Shown is an interaction at $r = 15$ mm. The electrons drift to the core, i.e. to smaller radii, therefore the reversed lower x -axis in panel (a). The holes drift to the outside, i.e. to larger radii (panel (b)). The thin line in (a) and (b) indicates the current for a charge drifting from the outer (inner) to the inner (outer) radius. The dot-dashed and dashed lines show the current contribution of the electrons and holes. The total current is shown in panel (c) by the solid line. The most prominent feature is the steep drop in the current signal near $t \sim 100$ ns, corresponding to the time when the electrons reach the core contact. With the steepest-slope-algorithm the time from the start of the pulse to the steepest slope in the current signal is determined, which is a direct measure of the radius r .

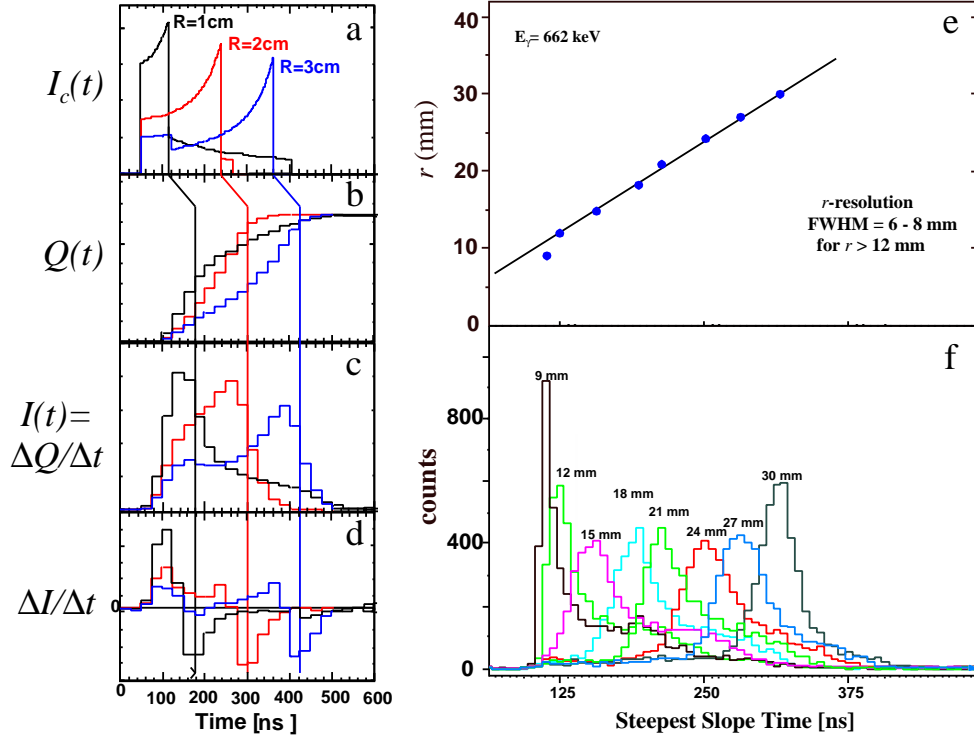


Figure 3.18: Radial resolution. The spot size of the γ ray collimator used was about 4 mm in diameter. The simulation in panels a-d were taken from [15] and the data in the panels e and f from [70].

is about ± 5 mm. In panel (e) a linear fit of the radial position to the measured centroids is shown, nicely demonstrating the linear relationship. The method does not work for radii smaller than 9–12 mm with the current electronics as for the second derivative at least 3 samples are necessary, meaning that a drift time of at least 75 ns ($= 3 \cdot 25$ ns) is needed. The corresponding detector volume is small however, so that for most events a good measurement can be made.

3.5.3 Determination of ϕ

To determine the ϕ angle the induced charges in the neighboring segments have to be considered. In figure 3.19 on the facing page typical pulses are shown in panels (a)–(d), where energy was deposited in only one segment (so-called one-segment-events). In panel (a) the core signal is shown and the step in the signal shows that a certain energy was deposited in the detector. Similarly, energy was deposited in segment 2 (panel (c)), while in the neighboring segments 1 and 3, shown in panels (b) and (d), respectively, no net

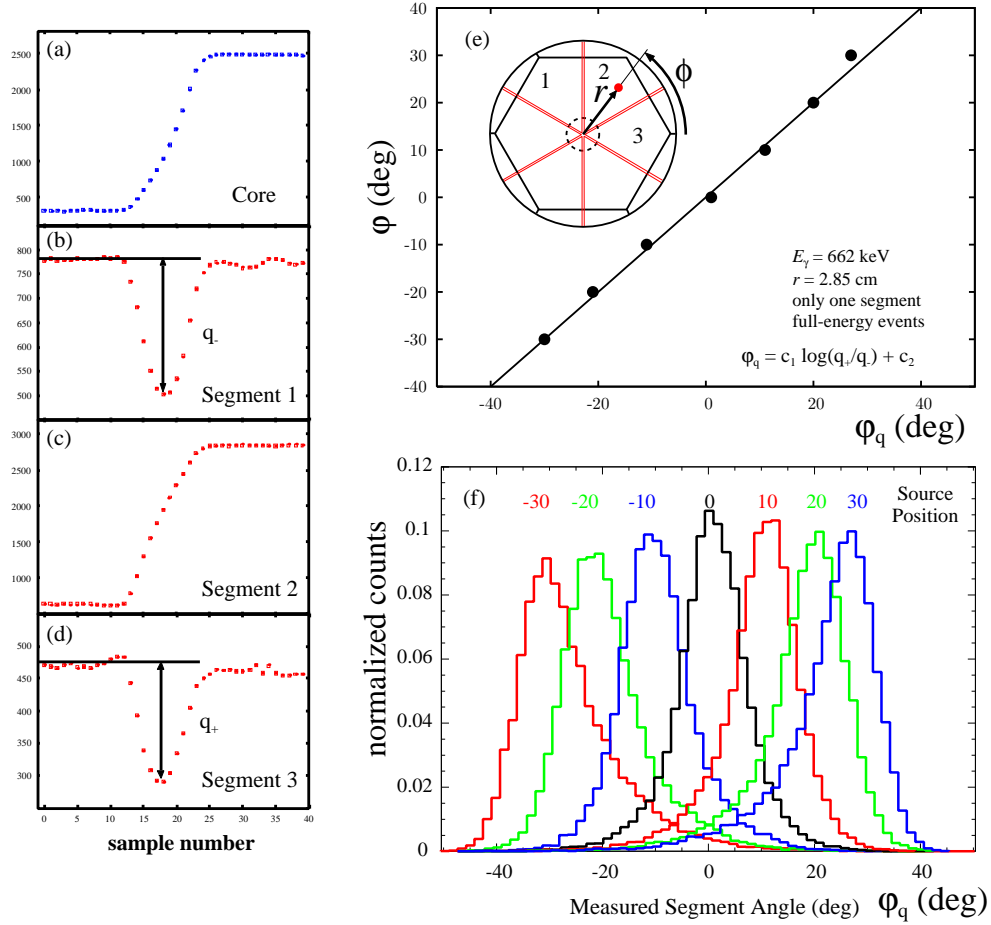


Figure 3.19: Azimuthal (ϕ) resolution. Panels (a)–(d) show measured current pulses [15, 18], while in panel (e) the ϕ_q calibration curve is shown. In panel (f) histograms are plotted measured with a collimated γ ray source (662 keV) at different collimator positions ($r = 28.5$ mm and $\phi = \{-30^\circ, -20^\circ, \dots, 30^\circ\}$). The inset in panel (e) shows the segment numbers corresponding to the pulses shown in panels (b)–(d).

charge was measured. But between sample numbers 12 and 26 temporary mirror charges were induced on these two segments electrodes. Their height will be the larger the closer the interaction takes place to the segment border. With the help of a detailed simulation and calculation of the weighting fields [15] it was found that the angle within one segment φ (measured from the segment center line) is proportional to the logarithm of the ratio of the maximum of the two charge signals in the neighboring segments q_+ and q_- :

$$\varphi_q \propto \log \left(\frac{q_+}{q_-} \right). \quad (3.5)$$

The angle ϕ is given by

$$\phi = n \cdot 60^\circ + \varphi_q, \quad (3.6)$$

where n is the segment number of the hit segment. In panel (f) histograms of φ_q measured with a collimated γ ray source for various collimator positions are shown. All histograms were obtained for $r = 2.85$ cm. The corresponding linear calibration [15] is shown in panel (e). While the angular resolution worsens for smaller r the arc-length resolution ($r \cdot \Delta\varphi$) remains nearly constant for all r with a value of ± 5 mm (FWHM).

In case charge is also deposited in one or more of the neighboring segments the algorithms have to be adapted [15, 70]. In [15, table 4.2] a detailed description of the best algorithm to determine the interaction position in the MINIBALL cluster detectors is given.

3.5.4 Implementation on the DGF-4C

The subject of one Diploma and one Ph.D. work at the MPI-K [17, 18] was the implementation of the above described algorithms on the DGF-4C card. To facilitate sufficient access to the soft and hardware of the commercial DGF-4C module this included a three-month visit at XIA. After the implementation the necessary parameters, such as the time of steepest slope and the maxima and minima of the induced charge, are included in the data stream. These parameters are used off-line to calculate the r and ϕ values. More details can be found in [17, 18, 55].

3.5.5 Resolution in In-Beam Experiment

In order to evaluate the position resolution in an experiment the reduction of the Doppler broadening was investigated. The standard MINIBALL setup at REX-ISOLDE was employed, described in section 3.6 on page 46. A stable ^{22}Ne beam was used for this purpose, which is copiously available from the REX-EBIS. The beam energy was $E = 2.25$ MeV/ u

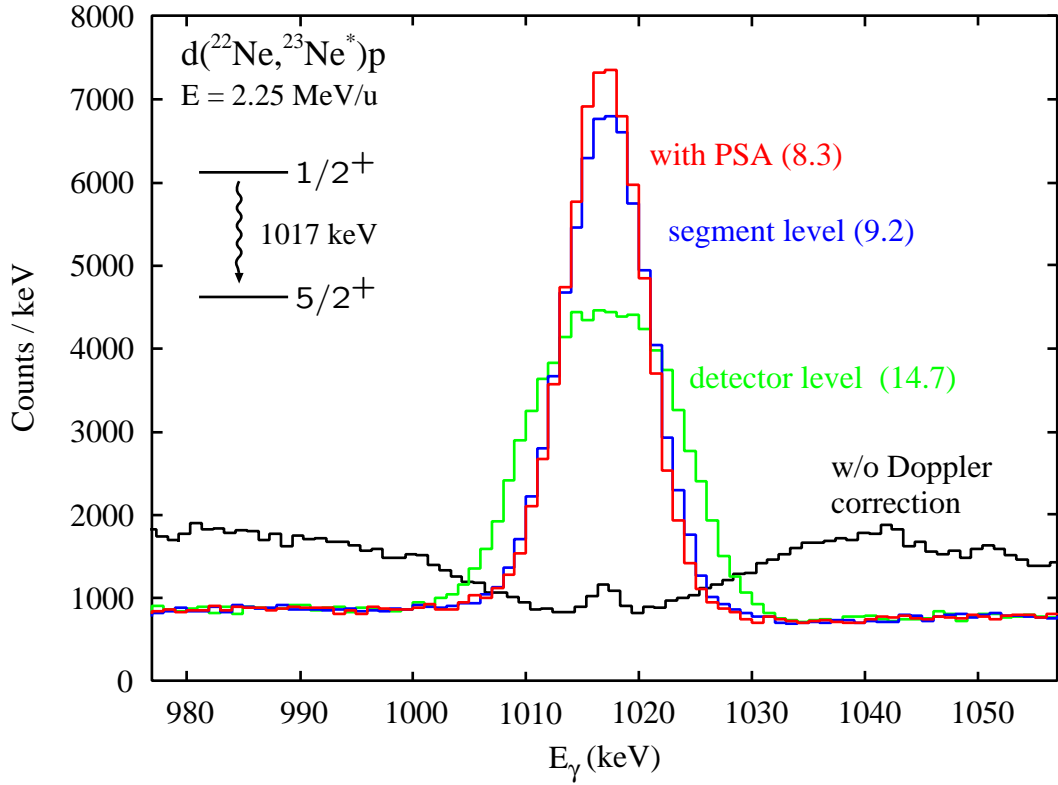


Figure 3.20: Energy resolution obtained in an in-beam experiment using the ^{22}Ne residual gas beam from the EBIS (see text). Depending on the information used for the Doppler correction different results are obtained. Without correction only two broad bumps can be seen, while when the detector position is used for the Doppler correction a peak can already be observed. When the segment information is included in the Doppler correction the resolution improves already to 9.2 keV (FWHM) and with the PSA information a value of 8.3 keV (FWHM) is obtained. The only modest improvement with PSA is largely due to the not corrected kinematics of the (d,p) reaction in inverse kinematics. See text for a discussion of additional reasons.

with an intensity of about 10^6 s^{-1} . A deuterated plastic target (99 % enriched) was used and in a (d,p) reaction in inverse kinematics the first excited state ($J^\pi = 1/2^+$) in ^{23}Ne was populated which decays by a $E_\gamma^{(0)} = 1017 \text{ keV}$ transition to the ground state ($J^\pi = 5/2^+$). The black histogram in figure 3.20 on the preceding page shows the γ energy spectrum without any correction for the Doppler shift. Only two “bumps” about 20–40 keV below and above $E_\gamma^{(0)}$ can be seen, which are caused by the grouping of the eight MINIBALL triple cluster detectors near 60° and 120° . When only the 24 detector positions are used for the Doppler correction a peak is already discernible with a resolution of 14.7 keV (FWHM). After the segment information is also used the resolution improves to 9.2 keV and with PSA a resolution of 8.3 keV is reached [55]. In the last step only a small improvement was realized. There are several reasons for this:

- The reaction kinematics was not considered and not corrected for. The angle of the outgoing ^{23}Ne with respect to the beam axis of about 5° increases the uncertainty in θ_γ .
- The beam spot size was at least 5 mm in diameter contributing to the uncertainty in θ_γ .
- Only global calibration parameters for the PSA were used. These could be optimized for each detector, or even for each segment.
- Data of eight cluster detectors contributed. Any uncertainty in the energy or position calibration results in a wider peak. A much improved result can be obtained by using only one triple cluster [70].

A better PSA calibration and an implementation of the prescription given in [15, table 4.2] to determine the γ ray interaction position is planned in the future. With this a position resolution of about $\pm 5 \text{ mm}$ in r and arc-length $r\phi$, corresponding to an effective increase in granularity of about 100 with respect to an unsegmented detector, should be achieved.

3.6 Standard Setup

The standard experimental setup that was used with MINIBALL at REX-ISOLDE is shown schematically in figure 3.21 on the next page. The MINIBALL target chamber (Al) is located at the center of the array. It has a radius of about 8.5 cm and a wall thickness of 2 mm. With a target wheel inside the chamber one of six targets can be inserted into the beam without opening the chamber.

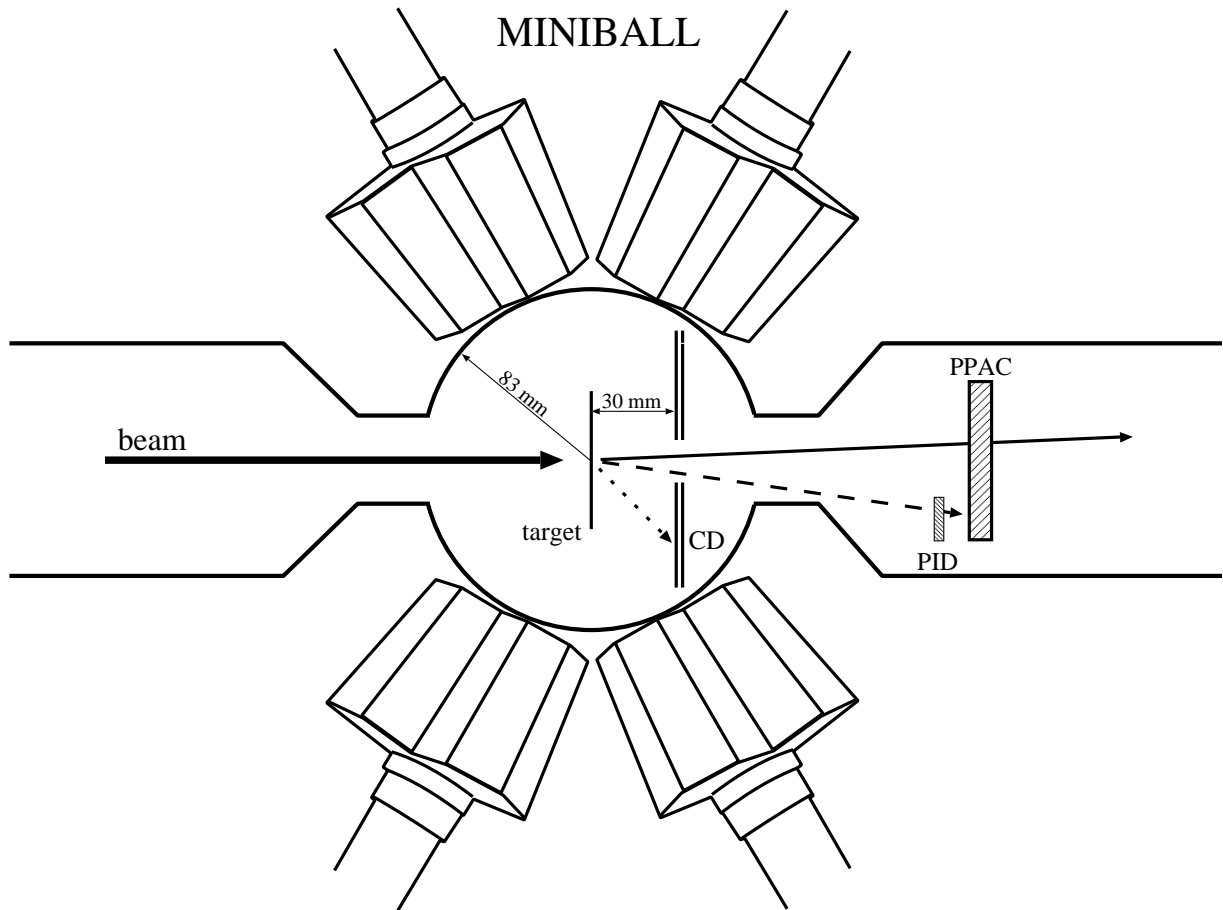


Figure 3.21: Schematic experimental MINIBALL setup (not to scale). See text for an explanation of the different components. After the target three particle tracks are shown. Most particles pass the target unperturbed (except for energy loss and resulting energy and angular straggling) and are measured by a parallel plate avalanche counter (PPAC) at zero degrees (solid line). A fraction of the incident beam is deflected to angles $> 5^\circ$ and can be registered by a thin ΔE detector (long-dashed line), which is not installed for all experiments. Elastically and inelastically scattered particles are detected by the CD detector in the θ_{lab} range from 16° to 53° (short-dashed line). The outer radius of the chamber is 85 mm with a wall thickness of 2 mm (Al).

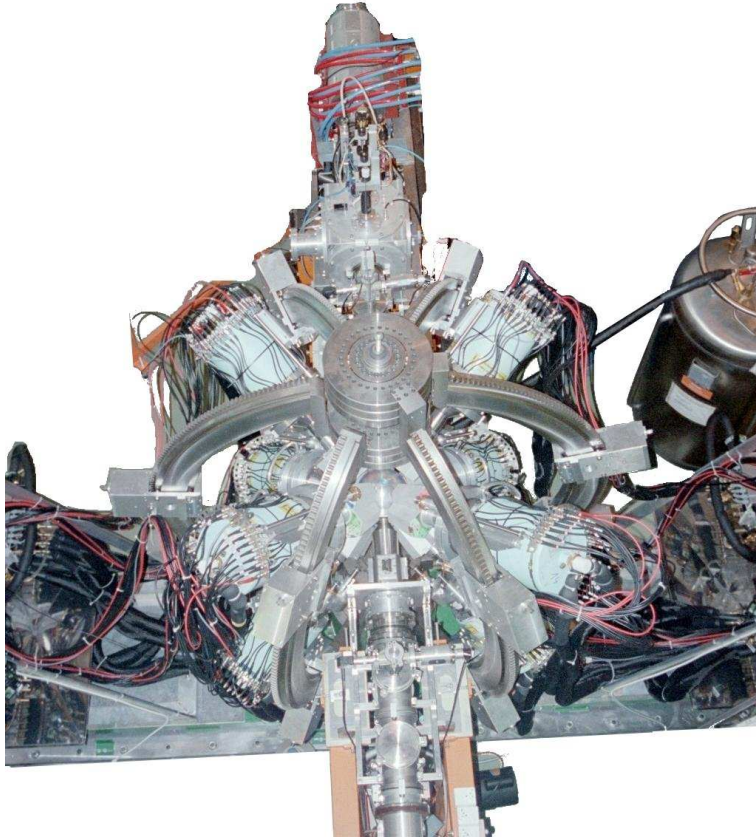


Figure 3.22: MINIBALL from top.

Installed inside the target chamber approximately 30.5 mm behind the target position is a compact-disk (CD) shaped charged particle detector [90] covering laboratory angles from 16° to 53° . This annular silicon p-i-n detector [91] consists of four highly segmented independent quadrants each with an azimuthal coverage of 82° , an inner radius of 7.5 mm and an outer radius of 42.5 mm. The front (p^+ -type) side of one quadrant consists of 16 annular strips of 1.9 mm width and 2 mm pitch, while the back (n^+ -type) side is comprised of 24 sector strips with a pitch of 3.4° . The CD quadrants employed so far had thicknesses between 476 and 481 μm [55], but detectors with a different thickness can be installed. Each of the quadrants was backed by an unsegmented detector of same shape and size, allowing for a ΔE - E measurement for hydrogen isotopes. While this telescope setup was not used for the Coulomb excitation measurements presented in chapter 5, as all particles are stopped in the first detector, it was used during calibration measurements where protons, deuterons and tritons could be distinguished in the bombardment of a deuterated polyethylen target with a stable ^{22}Ne beam.

In order to monitor the shape, size and location of the beam a parallel plate avalanche counter PPAC [92] is installed at zero degrees about 15 cm behind the target. It has an annular active area of 4 cm diameter and an effective thickness of only 1 mg/cm², including the gas (typically 5 mbar CF₄), two gas containment foils, one aluminized mylar cathode foil and two anode foils with each 25 evaporated aluminum strips of 1.6 mm pitch. The small effective thickness allows the *radioactive* beam particles to traverse the PPAC without stopping and to reach the shielded beam dump about 2 m downstream, keeping the singles count rate in the MINIBALL detectors at acceptable levels. It was employed for the first time in an in-beam test experiment at the MPI-K [93]. While it can be operated in single-particle mode allowing for an event-by-event x - y position measurement, in most experiments at REX-ISOLDE the current readout mode was used, as the instantaneous intensity—see section 2.4 on page 14—was too large even for the weakest beams. In current readout mode the current on each of the 25 horizontal and vertical strips is measured providing a projection of the beam profile onto the x - and y -axes.

After the first commissioning beam times in 2002/3 it became apparent that a reliable and unambiguous beam particle identification was needed. For the beams relevant in this work with $Z \leq 16$ two about 10 μm thick silicon diodes with an area of $1 \times 1 \text{ cm}^2$ were installed covering laboratory scattering angles from about 3° to 7°. As the beam particles from the REX accelerator have a known charge to mass ratio q/A and a known velocity β the energy loss in these diodes (being proportional to Z^2) can be used to determine the charge number Z of the projectiles. See also sections 2.5 on page 16 and 5.1 on page 71.

Chapter 4

Coulomb Excitation

The purpose of this chapter is to introduce the subject of Coulomb excitation and to mention those features of the theory that are needed to understand the analysis of the presented data obtained in the first Coulomb excitation studies at REX-ISOLDE/MINIBALL. In the first part of the chapter up to section 4.6 on page 61 the main characteristics of Coulomb excitation (CE) with beam energies below the Coulomb barrier, so-called “safe” CE, are described. For a detailed and almost complete development of this theory the reader is referred to the excellent monograph by Alder and Winther [71] and numerous other books and review articles (e.g. [72, 94, 95]). For completeness, in section 4.7 on page 63 the main aspects of intermediate energy CE are treated, which help to understand possible sources for the discrepancy between results obtained at low and intermediate energies. Finally in section 4.8 on page 64 the experimental method used for the presented measurements is described.

4.1 General Considerations

Coulomb excitation (CE) is the excitation of a nucleus in a time-dependent electromagnetic field present in the collision of two atomic nuclei. If the bombarding energy is sufficiently low the colliding nuclei stay far enough apart to ensure that the interaction via the strong force between them remains negligible. In this case the interaction is dominated by the well known electromagnetic force, allowing a *quantitative* analysis of the observed cross sections in terms of the static and dynamic electromagnetic multipole moments of the nuclei, which are the only nuclear properties entering into the theory, making it manifestly independent of any nuclear (reaction) model.

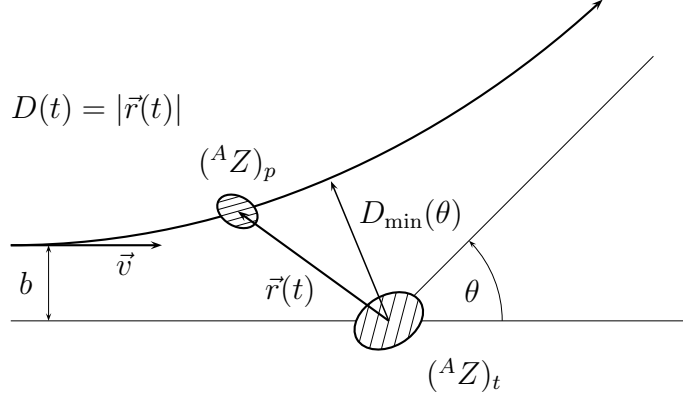


Figure 4.1: Shown is a Coulomb trajectory in the center-of-mass system, i.e. the target is assumed to be infinitely heavy and the projectile mass corresponds to the reduced mass. The vector $\vec{r}(t)$ is pointing from the target to the projectile; its magnitude $D(t)$ determines the electric field strength felt by the projectile. The initial velocity of the projectile is v . The impact parameter b and the deflection angle θ are also shown. An important quantity is the minimum distance during the collision $D_{\min}(\theta)$, which is equal to $2a_0$ in a head-on collision with $b = 0$.

4.1.1 The Sommerfeld Parameter

The Sommerfeld parameter η indicates if the semi-classical approximation, which is commonly used in the treatment of the CE process, is applicable. It is a measure of the minimum target-projectile distance in units of the de Broglie wavelength of the projectile λ

$$\eta = \frac{a_0}{\lambda} = \alpha \frac{Z_p Z_t}{\beta}. \quad (4.1)$$

Here a_0 is half of the distance of closest approach D_{\min} in a head-on collision, β is the *initial* velocity of the projectile in units of the speed of light c and $Z_{p,t}$ are the proton numbers of the projectile and target, respectively. The expressions for a_0 and λ are given by

$$a_0 = \frac{1}{2} \frac{Z_p Z_t e^2}{E_{\text{cm}}} = \frac{Z_p Z_t e^2}{mv^2} = \frac{Z_p Z_t e^2}{c^2 m \beta^2}, \quad (4.2)$$

$$\lambda = \frac{\hbar}{p} = \frac{\hbar}{mv} \quad (4.3)$$

and α is the fine structure constant. The classical trajectory together with characteristic quantities of the orbit, such as the scattering angle θ and the impact parameter b , is shown in figure 4.1.

If η is much larger than unity a quantum mechanical wave packet is expected to follow the classical trajectory and the semi-classical approximation can be applied to treat the excitation process. In this case the relative motion of projectile and target is considered classically, while the excitation process is treated quantum mechanically. The Hamiltonian describing the system acquires an explicit time dependence given by the orbit of the projectile.¹ Besides a large Sommerfeld parameter other conditions must be fulfilled before the semi-classical approximation can be applied, namely the change in the orbit due to the excitation process (removal of kinetic energy) and due to angular momentum transfer has to be small [28, 71, 72].² For the systems considered here all these conditions are fulfilled: the values of η are larger than 35, only the lowest excited states with spin of $2\hbar$ and excitation energies around 1 MeV are populated with typical center-of-mass beam energies of 50 MeV and orbital angular momenta in excess of $1000\hbar$.

The (small) systematic uncertainties introduced by the semi-classical approximation can be taken into account by appropriately symmetrizing the parameters ξ , χ , a_0 , and η (see below) with respect to the initial and final relative velocities. The differences between an exact quantal treatment and a semi-classical one are on the order of 1 to 3 % [72, 97]. The reason for the very accurate results within the semi-classical approach (even when the above conditions are nearly violated) might be the fact that the classical Rutherford scattering cross section is identical to the quantal expression [96]. Furthermore it was shown that even a purely classical calculation gives reasonable estimates of the maximum spin populated during Coulomb excitation [28, 98], stressing the validity of the semi-classical approximation.

4.1.2 Excitation Cross Section

Since the projectiles follow the classical orbit the elastic cross section corresponds to the Rutherford expression with the center-of-mass scattering angle θ

$$\frac{d\sigma_R(\theta)}{d\Omega} = \left(\frac{a_0}{2}\right)^2 \sin^{-4}\left(\frac{1}{2}\theta\right), \quad (4.4)$$

and the cross section σ_n to excite a certain final nuclear state $|n\rangle = |I_n m_n\rangle$ is

$$\sigma_n = \int \frac{d\sigma_n(\theta)}{d\Omega} d\Omega \quad \text{with} \quad \frac{d\sigma_n(\theta)}{d\Omega} = P_n(\theta) \frac{d\sigma_R(\theta)}{d\Omega}. \quad (4.5)$$

¹Here and in the following “orbit of the projectile” means the orbit of the reduced mass in the center-of-mass frame.

²There is also an interesting discussion of this topic in [96, section on Coulomb scattering].

The excitation probability is

$$P_n(\theta) = |a_n(\theta)|^2, \quad (4.6)$$

where $a_n = \langle n | \psi(t = \infty) \rangle$ is the amplitude to populate the state $|n\rangle$ if the system was initially in the ground state $|\psi(t = -\infty)\rangle = |0\rangle$; $|\psi(t)\rangle$ is the time dependent state vector of the nuclear system. As the nucleus to be excited is usually not aligned and in the final state the magnetic quantum number is not distinguished an average over m_i and sum over m_f must be performed

$$P_{f,i}(\theta) = \frac{1}{2I_i + 1} \sum_{m_i, m_f} |a_{I_f m_f, I_i m_i}(\theta)|^2, \quad (4.7)$$

to obtain the excitation probability to the state $|I_f\rangle$ from the state $|I_i\rangle$.

4.2 Coupled Equations

From the previous section it is clear that in order to compute the excitation cross section the amplitudes a_n must be known. In this section coupled differential equations for the a_n are derived which can, at least in principle, be solved exactly without any other approximation besides the semi-classical one.

In the following the excitation of the projectile nucleus is considered, but the relations apply to the excitation of the target nucleus as well if the target and projectile charge number Z and the matrix elements are exchanged. Unless otherwise specified all quantities are considered in the center-of-mass system and m is the reduced mass of projectile-target system

$$m = \frac{m_p m_t}{m_p + m_t}. \quad (4.8)$$

With the trajectory of the projectile $\vec{r}(t)$ given by the classical expression, the excitation process is described by the time-dependent Schrödinger equation

$$i\hbar \dot{|\psi(t)\rangle} = (H + V(t)) |\psi(t)\rangle, \quad (4.9)$$

where H is the intrinsic free (nuclear) Hamiltonian and $V(t)$ is the time-dependent electromagnetic interaction potential between target and projectile; its explicit time-dependence is due to the assumed classical trajectory $\vec{r}(t)$. As the multipole-multipole interaction is weak the Schrödinger equation of the combined system of target and projectile can be separated into two independent equations for projectile and target excitation. In this case the potential V in 4.9 describes only the monopole-multipole interaction as the monopole-monopole

interaction is absorbed into the classical trajectory and the explicit time dependence of the potential. In equation 4.9 on the facing page $|\psi\rangle$ is the state vector of the target (projectile) nucleus and V is the potential of a point charge Z_p (Z_t) at the projectile (target) position.

Expanding the state $|\psi\rangle$ in terms of the eigenstates $|n\rangle$ of the unperturbed Hamiltonian H with eigenvalue E_n

$$H|n\rangle = E_n|n\rangle, \quad (4.10)$$

$$|\psi(t)\rangle = \sum_n a_n(t) e^{-i\omega_n t} |n\rangle \quad \text{with} \quad \omega_n = \frac{E_n}{\hbar}, \quad (4.11)$$

results in a set of first order differential equations for the excitation amplitudes $a_n(t)$ as a function of time

$$i\hbar \dot{a}_n(t) = \sum_m \langle n|V(t)|m\rangle e^{i(E_n - E_m)t/\hbar} a_m(t). \quad (4.12)$$

The solutions of these equations are straightforward—while not trivial—to obtain with the condition that the nucleus is initially in the ground state, i.e. $a_i(-\infty) = \delta_{0i}$. Please note that $a_n(t)$ and $V(t)$ implicitly depend on the orbit, i.e. on the scattering angle θ . The final excitation amplitudes are found for $t \rightarrow \infty$ and the excitation probability is given by 4.6 on the preceding page, i.e. $P_n = |a_n(\infty)|^2$. It should be noted that $|n\rangle$ specifies exactly one state $|I_n m_n\rangle$ and appropriate sums and averages over the magnetic quantum numbers have to be taken as discussed in section 4.1 on page 51. Furthermore the exact solution is only obtained if *all* states are considered. In practice, however, only few states are coupled strongly to the ground state and the neglect of higher-lying states causes only small deviations. This is especially so for the results presented here, where only the $B(E2; 0_{\text{gs}}^+ \rightarrow 2_1^+)$ value, i.e. the reduced transition probability between the ground and the first excited 2^+ , is of interest.

4.2.1 Multipole Expansion

By performing the usual multipole expansion of the potential the matrix element $\langle n|V(t)|m\rangle$ can be decomposed into a part only dependent on the nuclear properties $\langle n||\mathcal{M}(E\lambda\mu)||m\rangle$, the so-called reduced matrix element, and another part that depends only on the parameters determining the orbit and the transition energy ΔE . The electric multipole operators are given by

$$\mathcal{M}(E\lambda\mu) = r^\lambda Y_{\lambda\mu}(\vec{r}) \left(\frac{1}{2} + \tau_z \right), \quad (4.13)$$

where the last term in parenthesis is the nuclear charge operator projecting the state vector of the protons; τ_z is the z component of the isospin operator [27, 94]. The magnetic terms

of the multipole expansion do not need to be considered for the excitation process, as they are suppressed by a factor of β^2 in the cross section.

The reduced matrix element $\langle I_0 \| \mathcal{M}(E\lambda) \| I_f \rangle$ is defined by the Wigner-Eckart theorem

$$\langle I_0 m_0 | \mathcal{M}(E\lambda\mu) | I_f m_f \rangle = (-1)^{I_0 - m_0} \begin{pmatrix} I_0 & \lambda & I_f \\ -m_0 & \mu & m_f \end{pmatrix} \langle I_0 \| \mathcal{M}(E\lambda) \| I_f \rangle \quad (4.14)$$

and corresponds to the multipole matrix elements $\langle I_0 m_0 | \mathcal{M}(E\lambda\mu) | I_f m_f \rangle$ with the trivial geometric factors—the first term on the right-hand side is a Clebsch-Gordan coefficient—removed.³ The averaging and summation over initial and final quantum numbers in the expression for the Coulomb excitation cross section leads to the definition of the reduced transition probability, the $B(E\lambda)$ value,

$$B(E\lambda; I_0 \rightarrow I_f) = \sum_{m_f \mu} |\langle I_0 m_0 | \mathcal{M}(E\lambda\mu) | I_f m_f \rangle|^2 \quad (4.15)$$

$$= \frac{1}{2I_0 + 1} |\langle I_0 \| \mathcal{M}(E\lambda) \| I_f \rangle|^2, \quad (4.16)$$

which will be needed later on in section 4.3 on page 58.

Electromagnetic Decay

While not important for this section it should be noted that the same electromagnetic multipole matrix elements characterize the electromagnetic decay of excited nuclear states. The partial γ ray transition probability of multipolarity $E\lambda$ is directly proportional to the $B(E\lambda; I_f \rightarrow I_i)$ value—shown in any standard nuclear physics textbook [27, 94, 99]—which is related to the value for the excitation via

$$B(E\lambda; I_f \rightarrow I_0) = \frac{2I_0 + 1}{2I_f + 1} B(E\lambda; I_0 \rightarrow I_f). \quad (4.17)$$

4.2.2 Adiabaticity

It is well known and can be seen from the exponential factor in 4.12 on the preceding page that the time dependence of the (pulsed) potential $V(t)$ plays a crucial role for the excitation process as an excitation can only occur if the time scale of the variation of V

³Sometimes in the literature a different definition, by a factor $\sqrt{2I_0 + 1}$, is used [94].

is on the same order or shorter than the nuclear period τ_n characteristic of the transition from one state to another: $\tau_n^{-1} = \omega_n = \Delta E/\hbar$. The adiabaticity parameter ξ is defined as

$$\xi = \omega_n \tau_c = \frac{\tau_c}{\tau_n} \quad (4.18)$$

$$= \frac{a_0 \Delta E}{\hbar c \beta}, \quad (4.19)$$

with $\tau_c = a_0/v$ being a measure for the duration of the collision. A substantial excitation can only occur if ξ is smaller or on the order of unity. For large ξ the nucleus follows the potential adiabatically changing only its orientation—similar to the needle of a compass in a slowly varying magnetic field—and the excitation probability drops exponentially with increasing ξ . For $\xi \ll 1$ the sudden approximation can be applied. Typical values for the systems of interest here are around 0.5.

This result is important also in view of the number of states that have to be included in 4.12 on page 55. From 4.19 and the condition $\xi < 1$ it follows that an excitation takes place only if

$$\Delta E < E_\xi = \frac{\hbar c \beta}{a_0}. \quad (4.20)$$

Thus, the excitation energy is essentially limited to values below 1–2 MeV in “safe” Coulomb excitation experiments where β is on the order of 5 %. This justifies to a large extent the neglect of transitions with larger energies in the treatment of the excitation process. For intermediate-energy “unsafe” Coulomb excitation this condition implies that even states with energies in excess of 10 MeV can be populated as discussed in section 4.7 on page 63 on intermediate-energy Coulomb excitation.

4.2.3 Excitation Strength

The magnitude of the excitation depends not only on the degree of adiabaticity but also on the strength of the interaction which can be estimated by

$$\chi^{(\lambda)} \approx \frac{V^{(\lambda)} \tau_c}{\hbar}, \quad (4.21)$$

where $V^{(\lambda)}$ is the interaction energy of multipolarity λ at the closest approach between target and projectile. Classically $\hbar\chi$ is equivalent to the time integral of the torque exerted on the projectile by the field of the target [28, 98], thus, the parameter $\chi^{(\lambda)}$ is an estimate of the number of quanta of multipolarity λ exchanged in the collision. A consistent and exact definition of χ is given in [71]; in particular for electric transitions

$$\chi^{(\lambda)} = \frac{\sqrt{16\pi}(\lambda-1)!}{(2\lambda+1)!!} \frac{Z_t e}{a_0^\lambda \hbar v} \frac{\langle I_0 \| \mathcal{M}(E\lambda) \| I_f \rangle}{\sqrt{2I_0+1}}. \quad (4.22)$$

If χ is small the probability of exciting the corresponding state is small, and perturbation theory can be applied. In contrast, if χ is large and ξ is small the state is strongly excited. In fact, for $\theta = \pi$ and $\xi = 0$ the excitation probability is given by $|\chi|^2$. For the $E2$ excitations, important here, the χ is given by

$$\chi^{(2)} = \frac{\sqrt{16\pi}}{15} \frac{Z_t e}{a_0^2 \hbar v} \sqrt{B(E2; 0_{\text{gs}}^+ \rightarrow 2_1^+)} . \quad (4.23)$$

Typical values for the systems of interest here are on the order of 0.2.

4.2.4 Computer Codes

For the numerical solution of 4.12 on page 55 the computer codes based on the original Winther & de Boer program [100, 101] such as CLX [102, 103] or GOSIA [104] are available and were used in the present work.

4.3 First Order Perturbation Theory

Equation 4.12 on page 55 can be solved approximately by first order perturbation theory. Even in cases where it is not strictly applicable, as in most experiments involving heavy ions as target and projectile, it still gives a reasonable estimate of the excitation cross section of the lowest states with large matrix elements to the ground state. Furthermore, the simple results allow insights into the Coulomb excitation process which cannot easily be obtained from the exact solution.

4.3.1 Excitation Amplitudes

Dropping the time dependence of the amplitudes a_i on the right-hand side of 4.12 on page 55 and fixing these amplitudes at their original values, i.e. $a_i = \delta_{0i}$, results in the following expression for the time derivative of the excitation amplitudes

$$i\hbar \dot{a}_n(t) = \langle n|V(t)|0\rangle e^{i\omega_n t} . \quad (4.24)$$

Here $\omega_n = E_n/\hbar$ with $E_0 = 0$, the ground state energy. This can easily be integrated to give

$$a_n = \frac{1}{i\hbar} \int \langle n|V(t)|0\rangle e^{i\omega_n t} dt . \quad (4.25)$$

After the expansion of the potential in terms of the electric multipole operators (see equation 4.13 on page 55) Alder & Winther [71] obtain

$$a_n = \frac{4\pi Z_t e}{i\hbar} \sum_{\lambda\mu} \frac{1}{2\lambda+1} \langle I_0 m_0 | \mathcal{M}(E\lambda, \mu) | I_n m_n \rangle^* S_{E\lambda\mu}, \quad (4.26)$$

where only the electric matrix elements were considered, as magnetic excitations are suppressed by a factor of β^2 (in the cross section) and can therefore be neglected. The term $S_{E\lambda\mu}$ contains the time integral over the classical orbit, including all information dependent on the parameters of the collision, while the matrix element $\langle I_0 m_0 | \mathcal{M}(E\lambda, \mu) | I_n m_n \rangle$ depends only on nuclear properties.

4.3.2 Cross Section

Inserting the above amplitudes into equation 4.5 on page 53 and after summing over the final and averaging over the initial magnetic quantum numbers the cross section is obtained

$$\sigma_{E\lambda} = a_0^2 |\chi^{(\lambda)}|^2 \frac{((2\lambda+1)!!)^2}{16\pi((\lambda-1)!)^2} f_{E\lambda}(\xi) \quad f_{E\lambda}(\xi) = \int_{\Omega_D} \frac{df_{E\lambda}(\theta, \xi)}{d\Omega} d\Omega \quad (4.27)$$

$$= \left(\frac{Z_t e}{\hbar v} \right)^2 a_0^{-2\lambda+2} B(E\lambda; I_0 \rightarrow I_f) f_{E\lambda}(\xi) \quad (4.28)$$

where $f_{E\lambda}$ is the Coulomb excitation cross section function $df/d\Omega$ [71] integrated over the solid angle covered by the particle detector Ω_D . It only depends on the parameter ξ introduced above—and θ for the differential expression—and can be easily calculated or looked up in compiled tables. The parameters ξ and χ introduced above are indeed the relevant quantities governing the excitation process as is evident from 4.28. For this work in particular the $E2$ contribution is the most relevant and the cross section is given by

$$\sigma_{E2} = \left(\frac{Z_t e}{\hbar v} \right)^2 a_0^{-2} B(E2; 0_{\text{gs}}^+ \rightarrow 2_1^+) f_{E2}(\xi) \quad (4.29)$$

Therefore, within the framework of first-order perturbation theory the Coulomb excitation cross section is directly proportional to the $B(E2; 0_{\text{gs}}^+ \rightarrow 2_1^+)$ value. Typical values for the systems considered here are on the order of 100 mb.

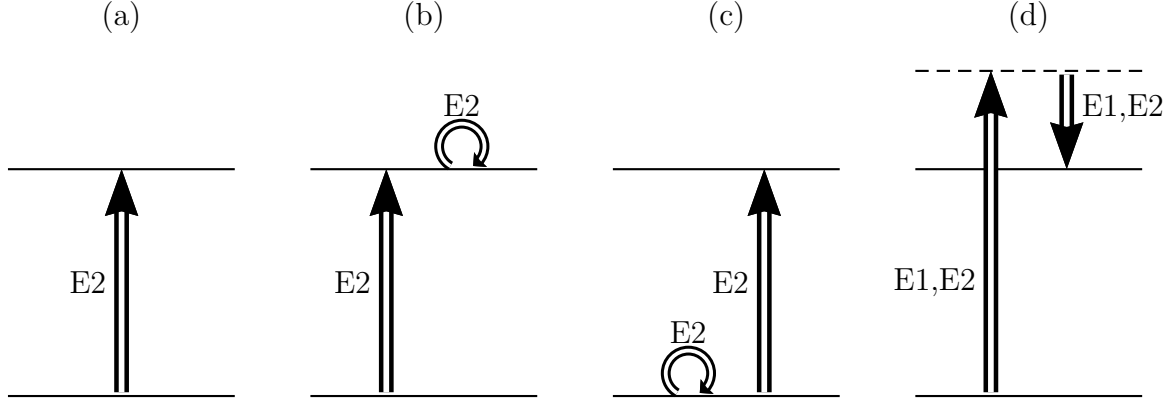


Figure 4.2: Pictorial representation of first and second order amplitudes in the excitation of the first excited state. Only the leftmost diagram (a) is of first order; all others are of second order. Diagram (c) does not contribute if the ground state possesses a spin of zero. Interference between (a) and (b) (and (c)) gives rise to the re-orientation effect. Diagram (d) shows a second order process where a high-lying state was virtually excited.

4.4 Re-Orientation

The so-called “re-orientation” effect⁴ describes the influence of the static quadrupole moment of an excited state $Q(J^\pi)$ on the excitation cross section. While it can be used to actually measure the quadrupole moments of excited states (e.g. [74]), it introduces an uncertainty into the results presented here and is therefore shortly discussed.

In the framework of perturbation theory the “re-orientation” effect, pictorially presented in figure 4.2, is of second order. The amplitudes of the direct (first order) population (a) interfere either constructively ($Q(2^+) > 0$) or destructively ($Q(2^+) < 0$) with the second order amplitudes (b). For a detailed treatment of the effect see [105].

To understand its influence on the cross section it is useful to consider the energy of the $m = 0$ magnetic state of a $J^\pi = 2^+$ state of an even-even nucleus, which is the only sub-state populated in a head-on collision. In the strongly inhomogeneous field of the target nucleus at the classical turning point the energy of the $|Jm\rangle = |20\rangle$ state is shifted due to the interaction of its *static* quadrupole moment with the electric field gradient [105, 107]

⁴The name “re-orientation” exists for historical reasons, as the effect can lead to a change of the magnetic sub-state population as compared to first order perturbation theory, resulting in a change of the alignment or “orientation”, influencing the angular distribution of the emitted γ rays. Its effect on the excitation cross section is much more important, however.

according to

$$\Delta E_Q = -\frac{e^2 Z_t Q(2^+)}{16a_0^3}. \quad (4.30)$$

For typical systems relevant here absolute values are in the range of 10-30 keV. If the 2^+ state has a prolate deformation $Q(2^+) > 0$ the excitation energy of the $m = 0$ sub-state is reduced, which significantly increases the excitation cross section especially if $\xi \gtrsim 1$, when the cross section depends exponentially on ξ [71].

4.5 De-Orientation

Before undergoing γ decay the excited nuclei usually leave the target material and recoil into the vacuum of the target chamber. The highly ionized atomic shells of the ions can produce very strong magnetic fields (up to 10 kT [72, 74]) and electric field gradients, which interact with the nuclear dipole and electric quadrupole moment, respectively. This hyperfine interaction leads to transitions among the magnetic sub-states more or less equilibrating their population, depending on the life-time of the excited state. In addition the fields are randomly oriented and the net effect is an attenuation of a possible alignment produced by the Coulomb excitation process. Usually neither the involved nuclear moments nor the electromagnetic fields are known. Therefore, models are used to take this effect into account, which assume random orientations and field strengths. For instance, the computer code GOSIA used in this work takes the de-orientation into account by attenuation factors G in the angular distribution integrated over ϕ_γ , due to cylinder-symmetric particle detection around the beam axis

$$W(\theta_\gamma, \tau) = 1 + a_2 G_2(\tau) P_2(\cos \theta_\gamma) + a_4 G_4(\tau) P_4(\cos \theta_\gamma). \quad (4.31)$$

These factors depend on the life-time τ of the excited nuclear state with $G(\tau) \rightarrow 0$ for large τ (fully de-oriented) and $G(0) = 1$ (initial alignment). In the present analysis also the effect of a “complete” de-orientation was considered but the influence was found to be small. This is partly due to the large solid angle coverage of the MINIBALL array and the particle detector.

4.6 “Safe” Distance Condition

The importance that the projectile and target nuclei stay outside the range of the nuclear force during the collision was already stressed in the beginning of this chapter. To quantify

this requirement a *surface* distance Δ_s is defined by subtracting the nuclear radii $R_{p,t}$ from the distance of closest approach $D_{\min}(\theta)$

$$\Delta_s(\theta) = D_{\min}(\theta) - R_t - R_p \quad \text{with} \quad D_{\min}(\theta) = a_0 \left(1 + \sin^{-1} \left(\frac{\theta}{2} \right) \right), \quad (4.32)$$

where the half-distance of closest approach in a head-on collision a_0 is given by

$$a_0 = \frac{1}{2} \frac{Z_p Z_t e^2}{E_{\text{cm}}} = \frac{Z_p Z_t e^2}{mv^2}. \quad (4.33)$$

Thus defined, Δ_s is the minimal distance between the *surfaces* of the two colliding nuclei. Due to the short range of the nuclear force, the rather well defined nuclear surface, and the large Sommerfeld parameter η it is a good parameter to study the validity of the theory of Coulomb excitation. Using experimental data on the Coulomb-nuclear interference effect several groups obtained “their” safe-distance condition

$$\Delta_s(\theta) > \Delta_s^{\min} \quad (4.34)$$

by observing deviations from the predictions either of the excitation function, i.e. the integrated cross section as a function of beam energy [108], or of the differential cross section as a function of the scattering angle θ [73, section 4].

Various ways to determine Δ_s and the corresponding Δ_s^{\min} were proposed with the aim to exhaust the safe-margin as strongly as possible without jeopardizing the model independence. The reason for this can be seen on equation 4.29 on page 59: the cross section scales with a_0^{-2} . Therefore a larger and “safer” distance of closest approach results in reduced cross sections. In addition, if ξ is near unity the total cross section function $f(\xi)$ depends exponentially on ξ ($f \propto e^{-\xi}$) [71] further reducing the cross section with increasing a_0 (see equation 4.19 on page 57). Therefore, a relaxation of the “safe” condition has already been proposed for experiments with rare exotic nuclei [9, 28], by accepting smaller Δ_s as long as the expected uncertainties are much smaller than the statistical ones.

The conditions obtained in the past with stable beams are to a large extent consistent with each other and range from rather complicated methods [109] to calculate the nuclear radius R from the mass number A , to the common proportionality of R to $A^{1/3}$: $R = r_0 A^{1/3}$ with r_0 ranging from 1.25 to 1.6 fm and corresponding safe surface distances Δ_s^{\min} ranging from 5 to 3 fm, respectively. For instance in [72] “a conservative crude safe ... criterion” is proposed with $r_0 = 1.25$ fm and $\Delta_s^{\min} = 5$ fm leading to non-Coulomb effects below 10^{-3} (!). Values of $r_0 = 1.6$ fm and 1.44 fm with $\Delta_s^{\min} = 3$ fm and 2.88 fm were put forward in [73, section 4] and [71, section x.4], respectively.

Ideally the beam energy should be chosen such that the safe condition 4.34 is fulfilled for $\theta = 180^\circ$, ensuring that nuclear effects are negligible for *all* scattering angles. In practice this is not always possible for the reasons mentioned above. In this work we adopted the very strict condition of $r_0 = 1.25$ fm and $\Delta_s^{\min} = 6$ fm and restricted the analysis to the angular range where 4.34 was fulfilled.

4.7 Intermediate Energy Coulomb Excitation

Intermediate-energy or relativistic Coulomb excitation is a relatively new experimental technique already discussed in chapter 1. It exploits the exotic beams with energies in excess of 30 MeV/*u* available at projectile fragmentation facilities such as RIKEN[51], GSI[110], MSU[111] and GANIL [112].

While the beam energy is highly unsafe, the basic features of this technique can easily be understood by considering the parameters η , ξ , and χ introduced above [113]. The definition of the parameters at these high beam energies is almost identical, only the half-distance of closest approach a_0 should be replaced by the impact parameter b in most expressions—plus a slight adjustment to take relativistic effects into account—see [113] for details.

As in the low-energy case, the Sommerfeld parameter η is usually large and the semi-classical approximation can be applied with assumed straight line trajectories. The interaction strength parameter χ (equation 4.21 on page 57), however, is always small due to the very short collision time τ_c . For low-lying states important in this work the collision is essentially sudden with $\xi \approx 0$, resulting in cross sections nearly independent of the excitation energy. Values of ξ near unity are reached only for excitation energies as high as 10–15 MeV, showing that at intermediate-to-relativistic energies even the giant resonance region can be excited. Therefore, any 1^- and 2^+ state will be excited if its transition matrix element with the ground state allows for it, in contrast to low-energy “safe” Coulomb excitation. Thus, in the analysis of such data, transitions from higher lying states, possibly feeding the first 2^+ state, must be taken into account.

The excitation probabilities will always be small and first order perturbation theory is a very good approximation [113]. The second order effects, such as re-orientation, can be neglected and the cross sections to excite low-lying 2^+ states of even-even nuclei are proportional to the $B(E2; 0_{\text{gs}}^+ \rightarrow 2_1^+)$ values.

Due to the high projectile velocities with $\beta \sim 0.3$ – 0.6 also magnetic excitations, which are suppressed at low energies by a factor of β^2 , are possible and must be considered where

appropriate. Often these excitations are ruled out by selection rules, as for even-even nuclei, where only $E2$ transition to the first excited 2^+ state are possible.

To ensure the dominance of the Coulomb interaction extremely forward projectile scattering angles of only a few degrees must be imposed. Furthermore, events in which violent reactions take place have to be avoided. The effects of the Coulomb-nuclear interferences have been discussed in the literature [52, 53, 114] and their influence on the results of these experiments is still not fully settled. Figure 6.2 on page 91 shows the results of coupled channel calculations of the differential cross section to excite the 2_1^+ state of ^{24}Mg , by scattering it off ^{208}Pb and ^{12}C targets at beam energies of 32 MeV/ u [53]. The effect of the Coulomb-nuclear interference is evident and variations in the cross section can be as large as a factor of two.

Concerning γ ray spectroscopy at these high beam velocities it should be mentioned that often the Doppler broadening is so large that even highly granular detectors reach only resolutions typical of scintillation detectors [115]. Furthermore, the backscattered electrons off the projectiles have energies of up to a few MeV causing copious X-ray backgrounds in the γ ray energy spectra reaching far into the energy range of interest as seen e.g. figure 5.7.

4.8 Experimental Method

While in the previous sections it was outlined how the nuclear properties that we are interested in, the $B(E2; 0_{\text{gs}}^+ \rightarrow 2_1^+)$ values, are related to the Coulomb excitation cross section, in this section the experimental method used to measure the cross section will be explained in detail. The principle of the measurement is simple: during the bombardment of the target material by the projectiles Coulomb excitation of both the target and the projectile takes place. The Coulomb excitation yields of the projectile and the target are proportional to the integrated luminosity $L = N_b(N/A)_t$, which is the product of the number of incident beam particles N_b and the areal density of the target nuclei $(N/A)_t$, the number of scattering centers per target area. Thus, the yield from the target is proportional to the yield from the projectile and the (unknown) projectile cross section can be determined from the (known) target cross section. In the present case the experimental observable is the yield of the detected γ rays from which the Coulomb excitation cross section is inferred. Several effects, such as the γ ray detection efficiency and possible beam contaminations have to be considered, as discussed below.

Even though the determination of absolute cross sections is preferable it would give

very error prone results, as first the beam intensity is only known to about a factor of two and second the macro and super time structures of the REX beam—section 2.4 on page 14—make it nearly impossible to obtain reliable and precise dead time values.

4.8.1 The γ Ray Yield

The number of γ rays detected (in the MINIBALL array), the γ ray yield, is given by

$$N_\gamma = \epsilon_\gamma \sigma N_b \left(\frac{N}{A} \right)_t = \epsilon_\gamma \sigma L, \quad (4.35)$$

where ϵ_γ is the *total* γ ray detection efficiency, L is the luminosity and σ is the Coulomb excitation cross section. The determination of ϵ_γ is somewhat cumbersome and is discussed in section 4.8.2 on page 67. For now we assume it is known.

The aim of the presented experiments is to study the (exotic) projectile nuclides. As equation 4.35 is valid for both target and projectile excitations and the (integrated) luminosity L is the same, the (unknown) excitation cross section for the projectile σ^p can be obtained from the (known) target cross section σ^t by multiplying it with the efficiency corrected ratio of the γ ray yields

$$\sigma^p = \frac{\epsilon_\gamma^p}{\epsilon_\gamma^t} \frac{N_\gamma^p}{N_\gamma^t} \sigma^t. \quad (4.36)$$

Unfortunately equation 4.36 is an oversimplification, because usually the beams are not pure and occasionally the target material is not mono-isotopic. Therefore, the following equations are needed to describe the γ ray yields of the target component k (N_γ^{tk}) and the beam component i (N_γ^{pi})

$$N_\gamma^{pi} = \sum_k \epsilon_k^{pi} \sigma_k^{pi} L_{ik} \quad (\text{projectile excitation}) \quad (4.37)$$

$$N_\gamma^{tk} = \sum_i \epsilon_i^{tk} \sigma_i^{tk} L_{ik} \quad (\text{target excitation}) \quad (4.38)$$

where

$$L_{ik} = N_{bi} \left(\frac{N}{A} \right)_{tk} \quad (4.39)$$

is the partial luminosity of projectile i with target component k . The cross section for the excitation of the beam (target) component i by the target (beam) component k is given

by $\sigma_k^{p(t)i}$. With the known abundances of target and beam species a_k and b_i

$$a_k = \frac{(N/A)_{tk}}{(N/A)_t} \quad b_i = \frac{N_{bi}}{N_b} \quad (4.40)$$

the following relation holds for the luminosities

$$L_{ik} = L b_i a_k, \quad (4.41)$$

where in each case the quantity without index is

$$L = \sum_{ik} L_{ik}, \quad N_b = \sum_i N_{bi}, \quad \left(\frac{N}{A}\right)_t = \sum_k \left(\frac{N}{A}\right)_{tk}. \quad (4.42)$$

There are a total of $2IK + 1$ unknowns (σ_k^{pi} , L_{ik} , and L) and $IK + I + K$ equations (4.37, 4.38, and 4.41), where I and K are the number of beam and target components, respectively. All other quantities can either be measured in the experiment, e.g. all N_γ s, or can be calculated, e.g. the target excitation cross sections σ_k^{ti} and the efficiencies. The number of degrees of freedom is therefore

$$(2IK + 1) - (IK + I + K) = (I - 1)(K - 1). \quad (4.43)$$

Only if there is exactly one target component ($K = 1$, any I) or exactly one beam component ($I = 1$, any K) can all σ_k^{pi} be determined. In the first case these are the cross sections σ^{pi} to excite the different beam components by the (one) target material and in the latter case the cross sections σ_k^p to excite the beam nuclide (one type) by the different target components. Fortunately there are other relations, namely the ratio of the cross sections for the excitation of the same beam nuclide i by different target components k can be calculated, resulting in the $I(K - 1)$ equations

$$\sigma_k^{pi} = s_k^i \sigma_1^{pi} \quad \forall \quad i = 1, \dots, I \quad \text{and} \quad k = 2, \dots, K, \quad (4.44)$$

where s_k^i are defined by the above equation and correspond to the cross section σ_k^{pi} relative to σ_1^{pi} , chosen to be the reference cross section. In practice the factor s can be assumed to be unity if the elementally pure target consists of different isotopes. Therefore, the number of degrees of freedom is reduced to

$$(I - 1)(K - 1) - I(K - 1) = 1 - K \quad (4.45)$$

and for any number of beam and target components a unique solution for the projectile excitation cross sections can be found. In fact, for more than one target component ($K > 1$) the cross sections are over-determined allowing for additional consistency checks.

Experimentally it is crucial to separate the different contributions in the γ ray energy spectrum based on the (Doppler corrected) γ ray energy alone, stressing the need for a γ ray spectrometer with the best resolution.

4.8.2 Efficiency

The total γ ray detection efficiencies ϵ occurring in 4.37 and 4.38 on page 65 include not only the detector efficiency $\epsilon_D(\Omega_\gamma^{\text{lab}})$, but also the effects of the distribution of the emitted γ rays $W(\Omega_\gamma)$ and the γ ray branching ratio b_γ if other decay channels exist. In the above expressions Ω_γ stands for a direction in space, i.e. $\Omega_\gamma = (\theta_\gamma, \phi_\gamma)$.

To determine the efficiency the following effects have to be considered: during Coulomb excitation the magnetic sub-states are not populated equally, resulting, in general, in an aligned excited state and a non-isotropic emission of the γ rays. The alignment is usually described by a density matrix ρ in the rest-frame of the emitting nucleus [71]; from it the double differential cross section⁵

$$\frac{d^2\sigma}{d\Omega d\Omega_\gamma} \quad (4.46)$$

is obtained (see e.g. [71, section iii.3]). The resulting angular distribution⁶

$$W(\Omega_\gamma) = \frac{1}{\sigma} \frac{d\sigma}{d\Omega_\gamma} = \frac{1}{\sigma} \int_{\Omega_D} \frac{d^2\sigma}{d\Omega d\Omega_\gamma} d\Omega \quad (4.47)$$

with

$$\sigma = \int_{\Omega_D} \frac{d\sigma}{d\Omega} d\Omega \quad (4.48)$$

has to be transformed into the laboratory frame before it can be folded with the detector efficiency $\epsilon_D(\Omega_\gamma^{\text{lab}})$.

For practical reasons, however, an alternative method was used. The transformation of a differential quantity such as 4.47 from one coordinate system to another, say from the system of the emitting nucleus into the laboratory, consists of two steps: first the direction $\Omega_\gamma = (\theta, \phi)$ has to be transformed $\Omega_\gamma \rightarrow \Omega_\gamma^{\text{lab}}$ and second the solid angle element $d\Omega_\gamma \rightarrow d\Omega_\gamma^{\text{lab}}$, i.e.

$$W^{\text{lab}}(\Omega_\gamma^{\text{lab}}) = W(\Omega_\gamma(\Omega_\gamma^{\text{lab}})) \frac{d\Omega_\gamma}{d\Omega_\gamma^{\text{lab}}}. \quad (4.49)$$

For γ rays the change in solid angle element can be considered most easily on an event-by-event basis during the evaluation of the experimental data, as

$$\frac{d\Omega_\gamma^{\text{lab}}}{d\Omega_\gamma} = \left(\frac{E_\gamma^{(0)}}{E_\gamma^{\text{lab}}} \right)^2. \quad (4.50)$$

⁵An Ω without subscript refers to the direction of the scattered projectile.

⁶If not otherwise specified all quantities are given in the rest frame of the emitting nucleus.

Thus, for all Doppler corrected spectra the events were not incremented with equal weight “one”, but with a weight given by 4.50 on the page before which is known for each event from the Doppler correction of the γ ray energies. For example a γ ray emitted in forward direction, i.e. with a small ratio $E_\gamma^{(0)}/E_\gamma^{\text{lab}}$, receives a reduced weight, compensating the increased detection probability for such a photon in the laboratory.

To correct the effect of the transformation of the direction Ω_γ the easiest is to transform the detector efficiency $\epsilon_\gamma(\Omega_\gamma^{\text{lab}})$ into the rest frame of the γ ray emitter neglecting the solid angle transformation. The transformed efficiency can then be folded with the γ ray angular distribution $W_\gamma(\Omega_\gamma)$

$$\langle \epsilon_\gamma \rangle = b_\gamma \int_{4\pi} \epsilon_\gamma(E_\gamma^{(0)}, \Omega_\gamma^{\text{lab}}(\langle \beta \rangle, \Omega_\gamma)) W_\gamma(\Omega_\gamma) d\Omega_\gamma, \quad (4.51)$$

where also the γ branching ratio b_γ is considered. Two approximations were applied in 4.51: in general the γ ray energy E_γ^{lab} depends on the direction Ω_γ and the velocity vector of the emitting nucleus via the Doppler shift—section 3.2 on page 21. For the MINIBALL setup, however, the efficiency changes nearly linearly within the variation of E_γ^{lab} and therefore the average transition energy $\langle E_\gamma^{\text{lab}} \rangle$ is used, which is to a good approximation given by $E_\gamma^{(0)}$. The second approximation concerns the transformation of the laboratory efficiency into the “rest frame” of the emitting nucleus. As the scattered projectiles and the recoiling target nuclei have no fixed scattering direction nor a fixed velocity, no exact transformation can be performed. Rather a transformation with an average velocity $\langle \beta \rangle$ along the z -axis, as the average scattering angle, was performed.

The errors introduced by these approximations are very small, since the MINIBALL array covers a large fraction of the full solid angle as does the CD detector. In fact the correction factors determined [55, 114, 116] for the cases considered here were less than 2 %, far below the typical statistical uncertainty of about 10 %. Furthermore even if one assumes that the distribution of the target (projectile) γ rays is isotropic and the one of the projectiles (targets) is as given above, the change in the deduced cross sections is only on the order of 5 % [114].

While a GEANT4 Monte Carlo simulation for the MINIBALL array was implemented [117, 118] and used for the determination of $\epsilon_D(\Omega_\gamma)$, to fully consider the angular distribution a corresponding event generator would have to be implemented. However, due to the expected small correction factors, this was considered too time consuming and not worth the effort.

Summarizing this section: the Coulomb excitation cross sections for the projectile(s) $\sigma_k^{\text{p}i}$ are determined by solving equations 4.37 and 4.38 on page 65, where the occurring

efficiencies ϵ are understood as the average values given by 4.51 on the preceding page and the N_γ s are the line intensities obtained from spectra where the individual events were incremented with a weight according to 4.50 on page 67.

4.8.3 Cross Sections

The computer codes CLX and GOSIA were used to calculate the Coulomb excitation cross sections (see section 4.2.4 on page 58). The calculation of the excitation cross section of the target nuclei σ_i^{tk} was performed including as much spectroscopic information as needed and available. In particular, not only the $B(E2)\uparrow$ values, but also the diagonal matrix elements were used when available and in the case of the ^{107}Ag target also the coupling between the excited states and the $M1$ matrix elements, which are important for the angular distribution, were considered.

For the projectiles the $B(E2)\uparrow$ value was varied in an iterative procedure until the measured cross sections were reproduced. Various (diagonal) static $E2$ matrix elements were assumed (see section 4.4 on page 60 and chapter 5).

In all cases the energy loss in the (rather thick targets) was not negligible and therefore the cross section was averaged over the target thickness by subdividing it into several slices (typically 11) and performing the above cross section calculations for each slice after adjusting the beam energy according to the energy loss (in the preceding slices).

Chapter 5

First Results

The aim of the two first experimental campaigns at REX-ISOLDE, one in Oct. 2003 and the other in Sept. 2004, was the determination of the $B(E2; 0_{\text{gs}}^+ \rightarrow 2_1^+)$ values of the neutron-rich Mg isotopes $^{30,32}\text{Mg}$ [119, 120], which are located near or in the so-called “Island of Inversion”. The physics issues to be addressed and answered were discussed in chapter 1, and the experimental method used, namely “safe” Coulomb excitation, in chapter 4. REX-ISOLDE was described in chapter 2 and MINIBALL in chapter 3, with the experimental setup described in section 3.6 on page 46.

In this chapter the analysis steps are outlined in section 5.2, with special focus on the important issue of the beam impurities (section 5.1), the sources of which were discussed in section 2.5 on page 16. The final results are presented in section 5.3 and in table 5.4 on page 85, where also the experimental parameters, such as beam energies and intensities, are listed.

5.1 Determination of Beam Impurities

As discussed in section 2.5 on page 16, one of the major concerns in experiments with post-accelerated beams from ISOL facilities are beam impurities of various origin. In particular, in Coulomb excitation experiments where the relative γ ray yield of projectile and target nuclei determines the result,¹ methods to qualitatively and quantitatively determine the beam impurities have to be developed. Only then can reliable results be obtained.

During the analysis of the measured data several methods to study the beam composition were investigated. These are sensitive to some or all of the sources of beam

¹For instance, excitations of the target by the beam impurities have to be subtracted. Formally, this is seen in equation 4.40 on page 66, where the abundances of each isotope b_i in the beam are required.

contamination identified in section 2.5 on page 16. The principles of the methods are mentioned and some examples are given here and summarized in table 5.1 on page 76; more details and the application to the presented results can be found in [55, 56, 114].

Method #1 Particles with different mass number A are most easily identified by their measured total energy in the CD detector. Since the A/q of the mass separator as well as the velocity of the ions β are known and A and q can only assume positive integer values, there are usually not many combinations for A and q for possible contaminants in the beam, which would match the nominal A/q . In addition, from the energy measured in the CD detector E_b an approximate particle mass number A can be determined from the kinetic energy relation $E_b = \frac{1}{2}Au\beta^2$, with u the atomic mass unit. Since the particles are scattered off the target, different Rutherford scattering cross sections and energy losses in the target have to be considered for a quantitative analysis. With the CD detector even particles of the same mass number A can be distinguished if a thick target is used and the energy loss due to the different Z is large enough to resolve the two (or more) contributions.

Method #2 The most direct method to identify and quantify the beam contaminants with the same A but different Z is the measurement of their energy-loss (proportional to Z^2) in the PID detector. Also this method is based on the fixed and known A/q and beam velocity β . Since small-angle scattering is observed (the detectors are located at about 5°) a correction for the different Rutherford cross sections as a function of Z and the energy loss in the target has to be performed. For example, in the right-hand panel of figure 5.1 on the facing page a sample spectrum is shown. The different components in the beam can clearly be separated, with the component with the smallest energy identified to be ^{32}Mg , the isotope of interest. In addition, in the left panel a yield dependence on $t_p = t - T_1$, the time since the last proton impact, can be seen², which will be discussed further below in this section. The installation of the detectors and the analysis of the results was part of a Diploma project at the MPI-K [56].

Method #3 The contamination can be estimated when the RILIS is used to ionize the particles: in this case a so-called LASER ON/OFF run can be performed, where the LASER is periodically blocked. By comparing the measured intensities in the particle and also in the γ detectors the amount of contamination can be inferred, assuming that during the measurements the yield of the ISOLDE target did not vary. However, with this method

²The time of the event is t and T_1 (ISOLDE jargon) is the time of the last proton impact; $t_p = t - T_1$ is therefore the time since the last proton impact.

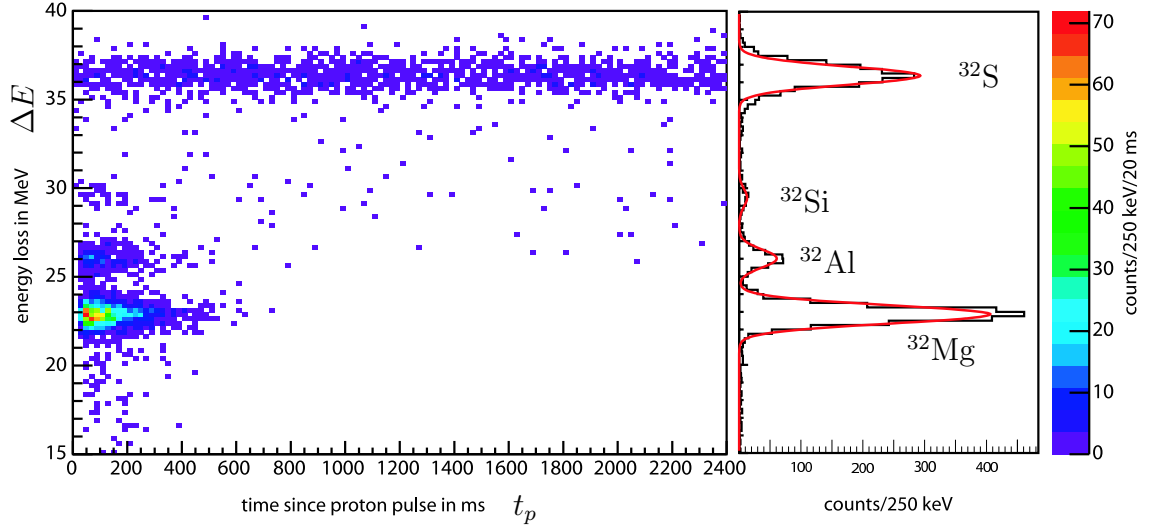


Figure 5.1: The measured energy loss ΔE (in the PID detector) vs. the time after proton impact $t_p = t - T_1$ observed in the ^{32}Mg beam of the Sept. 2004 campaign (see table 5.4 on page 85). Impurities of radioactive ^{32}Si , ^{32}Al , and stable ^{32}S can be seen. Due to the short half life of ^{32}Mg (95 ms) it is only observed for about 400 ms after proton impact. In contrast, the stable ^{32}S stems from the EBIS residual gas and is always present independent of t_p . In the right panel the projection on the ΔE axis is displayed without any additional cut on t_p . For the analysis of the CE data a cut of $0 \leq t_p \leq 400$ ms was applied strongly suppressing the S contamination. The energy-loss values ΔE do not follow an exact Z^2 dependence due to the energy loss in MINIBALL target (^{107}Au , 1.1 mg/cm²) and the large thickness of the PID detector. The S contribution is almost stopped in this detector.

only the contamination from the ISOLDE target is accounted for; e.g. contributions due to the β decay during trapping and breeding cannot be observed. Moreover, the efficiency of the REX-TRAP depends on the intensity of the beam and can be different in the LASER ON and LASER OFF periods, which might distort the extracted results.

Method #4 The effect of the β decay during breeding and trapping can be calculated from the known life-times and branching ratios. An example is given on page 78.

Method #5 The release curve, a histogram showing the intensity of the ion beam as a function of time after proton impact t_p , can also be used to determine the beam purity if the release times from the ISOLDE target for the wanted nuclear species are sufficiently different from that of the not wanted ones and short in comparison to the PSB repetition

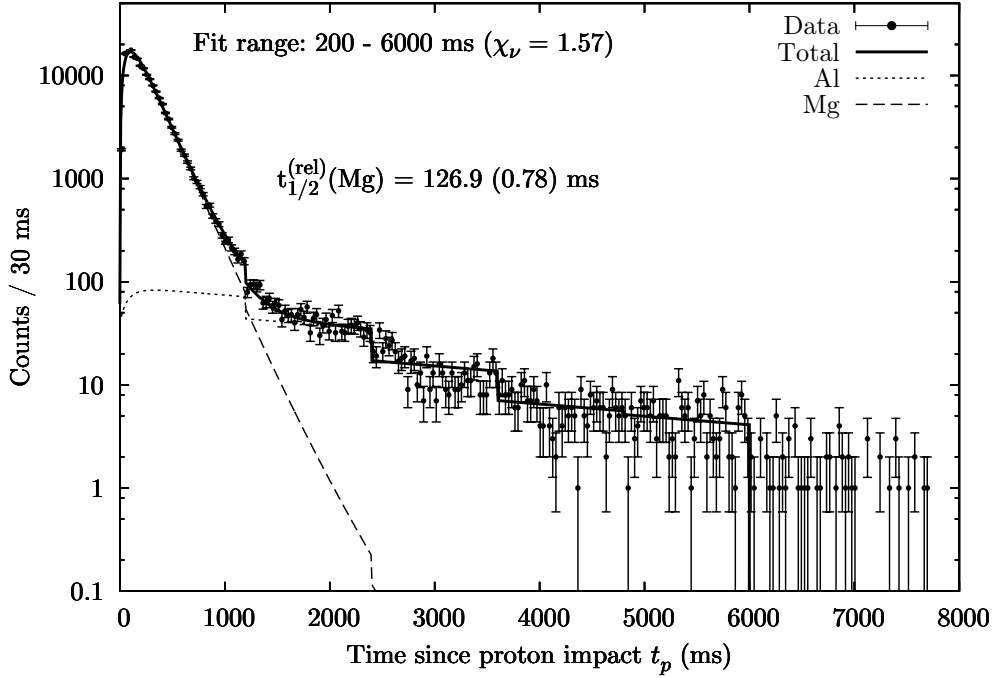


Figure 5.2: Release curve measured in the ^{30}Mg experiment (Oct. 2003) by observing the particles in the CD detector scattered off a $^{\text{nat}}\text{Ni}$ target (see table 5.4 on page 85). The proton impact occurs at time zero followed by a steep rise in the yield mainly due to produced ^{30}Mg , which is released fast from the target with only negligible yield after 2 s. The data are fitted with a sum of two functions describing the typical release from the ISOLDE target [62, 66] for Mg and Al. The fitted release time for Mg $t_{1/2}^{(\text{rel})}(\text{Mg})$ of 127 ms (dashed curve) agrees very well with the previously measured Mg release time (190 ms) [66], which only depends on the element, folded with the half-life of ^{30}Mg (335 ms), resulting in 121 ms. Al is released much slower (dotted curve). By integrating the fitted functions in the t_p range used for the analysis (0–1.2 s in this case) the effective beam contamination is determined. The steps in the data (and the fit) at $n \cdot 1.2$ s are due to varying time distances between PSB proton pulses delivered to ISOLDE within the PSB super cycle.

rate of about 1.2–2.4 s. An example of a release curve is shown in figure 5.2 on the preceding page together with a two-component fit from which the amount of the contamination can be extracted. This method is sensitive to the impurities released directly from the ISOLDE target and from the EBIS.

Method #6 A method to check which contamination comes from the EBIS and which from the ISOLDE target is to compare measurements with open and with closed beam gate (electro-static deflector), blocking the beam directly after the ISOLDE target. Everything present with the beam gate closed must come from the EBIS.

Method #7 In special cases it is possible to look for known reaction channels of the contaminant with the target. For instance in one measurement a limit on the Coulomb excitation yield of the first excited state of ^{30}Al could be deduced, which gave an upper limit for the total ^{30}Al contamination [55, 114] listed in table 5.2 on page 77.

Method #8 Last but not least if the β and γ branching ratios are known the intensity of each radioactive beam component can be inferred from the measured γ yield after β decay. Since most of the contaminants are isobaric the γ ray yield of a contaminant line is usually the sum of the direct contamination and the contribution from the β decay of other isotopes. Only by carefully subtracting the different contributions starting with the most exotic nuclide can reliable results be extracted [55]. This method is not sensitive to stable or long lived impurities.

Comparison As an example the results obtained with some of the methods are shown in table 5.2 for the case of a ^{30}Mg experiment of the Oct. 2003 campaign. The methods are indeed consistent with one another, except for the LASER ON/OFF, which deviates slightly probably due to the reasons mentioned above (method # 3).

The different methods are summarized in table 5.1 on the next page. For some methods (#3, 4, and 6) special action is needed to use them, such as blocking the LASER, thereby interrupting the running measurement. With others (#1, 2, 5, 7, and 8) the beam impurities can be monitored throughout the course of the experiment as is shown in figure 5.3 on page 77, where the ^{32}Al contamination is shown as a function of time, as measured by the two PID detectors during the about 60 hours long ^{32}Mg beam time. Only a slight variation with time occurs which might be caused by changes in temperature of the ISOLDE target modifying the surface ionization efficiency of Al. Please note that the figure uses an expanded scale ranging from 10 % to 15 % only.

#	Method	Detector	Meas. quant.	Sensitive to impurities from		
				ISOLDE target	TRAP/EBIS res. gas	β -decay
1	Energy	CD-detector	A, I_A	*	*	*
2	Energy loss	PID-detector	Z, I_Z	*	*	*
3	LASER ON/OFF	CD, PID, MINIBALL, BD	I_t	*	—	—
4	β decay	pen, paper and computer [†]	$I_{A,Z}$	—	—	*
5	Release curve analysis [§]	CD, PID, MINIBALL, BD	$I_{A,Z}$	*	*	—
6	Beam gate OPEN/CLOSE	CD, PID, MINIBALL, BD	I_t	—	*	—
7	Reactions of contaminant	CD, MINIBALL	$I_{A,Z}$	*	*	*
8	β decay	MINIBALL, BD [‡]	$I_{A,Z}$	*	—	*

Table 5.1: Different methods to measure the beam contamination and their sensitivity to the different sources, together with the detectors used and the quantity measured. Each method is only sensitive to the sum of its contributing sources. An advantage of methods 1 and 2 is that the particles are identified experimentally and for each isotope the intensity $I_{A,Z}$ is available. Other methods are only sensitive to the changes in the total intensity I_t , but the type of contamination is not known. Methods # 1, 2, 5, 7 and 8 can be applied during the actual measurement, while for the others special steps have to be taken, such as blocking the LASER. The beam dump detector (BD) is a Ge detector placed near the beam dump to monitor the beam intensity.

[†] to calculate the intensities

[‡] to observe γ rays after β decay

[§] only applicable if the release and decay times are known and in right range

method	#	$N(^{30}\text{Al})_{\text{decay}}$ [%]	$N(^{30}\text{Al})_{\text{ISOLDE}}$ [%]	$N(^{30}\text{Al})_{\text{total}}$ [%]
breeding	4	4.49 (22)		
LASER on/off	3		4.74 (86)	
release curve	5		2.01 (7)	
weighted average		4.49 (22)	2.03 (7)	6.52 (23)
β -decay	8			7.7 (22)
^{30}Al CE	7			< 11.4
adopted value				6.53 (23)

Table 5.2: Amount of ^{30}Al in the ^{30}Mg beam deduced from different methods with the condition $0 \leq t_p \leq 1.2$ s (run of Oct. 2003). In the second column (#) the used method according to table 5.1 on the facing page is given. The values in the last column in the row “weighted average” is the sum of the values in the second and third columns. It agrees well with the other methods (# 8 and # 7).

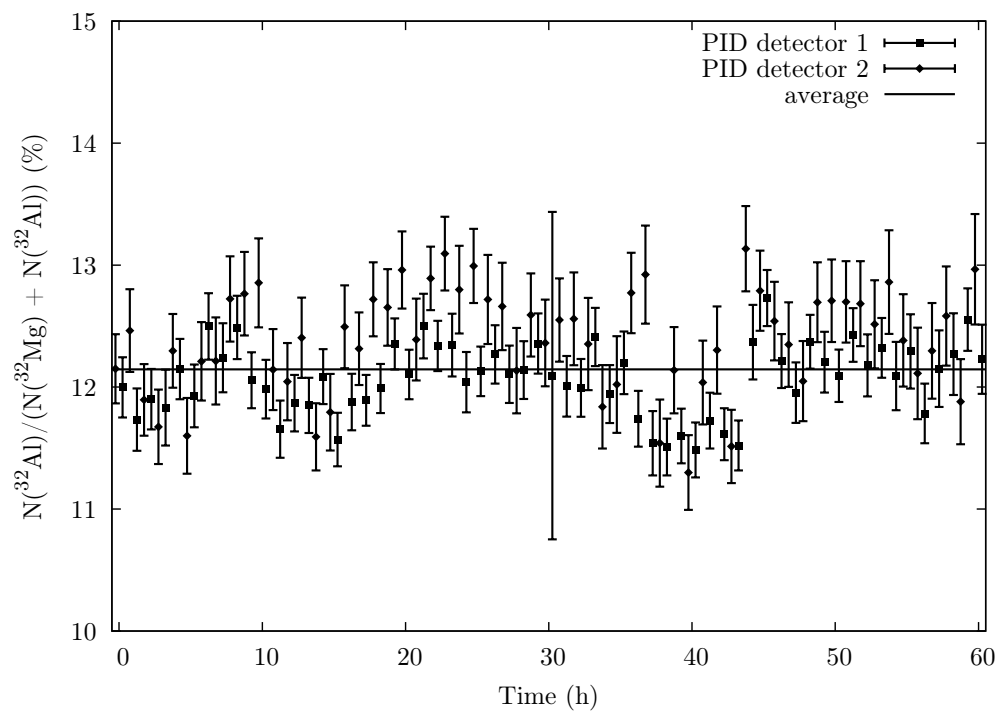


Figure 5.3: Beam contamination (^{32}Al) as function of time during the about 60 hour long ^{32}Mg run in Sept. 2004 (see table 5.4 on page 85). The PID detector (method #2) was used to obtain the values by accumulating data for one hour with the condition $0 \leq t_p \leq 400$ ms and integrating the ^{32}Al and ^{32}Mg peaks. See also figure 5.1 on page 73. Please note the expanded scale ranging from 10 % to 15 % only.

Correlation of t_p time with other detector signals

The knowledge of the time of each event t in relation to the time of the last proton impact T_1 , used already for the release curve analysis (method #5), helps to analyze and understand the spectra measured with the other detectors (CD, PID, MINIBALL) by correlating their signal with the time difference $t_p := t - T_1$. For example, in figure 5.1 on page 73 the measured energy loss in the PID detector is shown versus the time since the last proton pulse t_p . It is evident that the contribution with the largest energy-loss signal is independent of the time of the proton impact and must therefore correspond to long-lived nuclei with a very slow release from the ISOLDE target or to residual gas from the EBIS. Further investigation showed that it corresponds to the stable ^{32}S which is present in minute quantities in the EBIS. The other contributions are ^{32}Mg (isotope of interest), ^{32}Al , and ^{32}Si . Due to the short half-life and its fast release from the target, ^{32}Mg ($t_{1/2} = 95$ ms) is essentially not present anymore after about 400 ms after proton impact.

It is also interesting to note that while the half-life of ^{32}Al is only 33 ms this isotope is still observed after 200 ms and has a similar distribution in t_p time as ^{32}Mg . This is direct prove that this contamination is due to the β decay of ^{32}Mg in the REX-TRAP and the EBIS. For instance, using the trapping and breeding time ranging from 12 to 32 ms (depending on the time when a particular ion entered the trap) and the life-times of ^{32}Mg and ^{32}Al (see figure 6.8 on page 100) an ^{32}Al contamination of 13.1(21) % is deduced, which agrees very well with the data displayed in figure 5.3 on the page before.

The beam purity can be effectively improved by only analyzing events where the isotope of interest has a substantially higher (instantaneous) intensity than the contaminants, e.g. for the analysis of the ^{32}Mg data a time cut of $t_p < 400$ ms was applied, strongly suppressing the ^{32}S contamination.

Once the beam contaminants are known qualitatively and quantitatively the excitation cross sections can be deduced from the γ ray yields according to the procedure outlined in section 4.8 on page 64. The analysis steps followed to obtain the γ ray yields are discussed in the next section.

5.2 Analysis of the Data

In the following the analysis steps will be explained. For details the reader is referred to the Ph.D. thesis of O. Niedermaier [55].

For the analysis of the γ ray energy spectra only events in coincidence with particles in the CD detector are considered, as only for these a proper Doppler correction can be

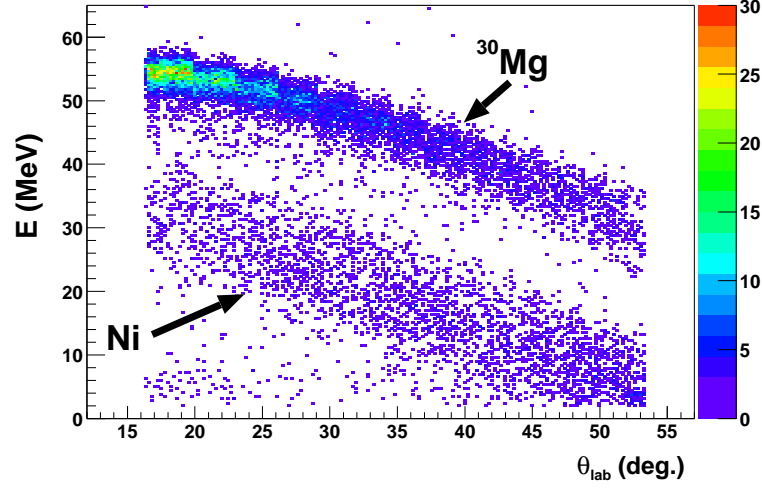


Figure 5.4: Particle single spectrum showing the measured particle energy vs. the measured laboratory angle for the ^{30}Mg run in Oct. 2003. Clearly two groups of events can be distinguished corresponding to scattered ^{30}Mg beam and to recoiling Ni target nuclei. Only the upper events, corresponding to ^{30}Mg laboratory scattering angles ranging from 16° to 53° , were analyzed to extract the γ ray yield. This ensured that the safe-condition (equation 4.34 on page 62) was fulfilled with a minimum surface distance Δ_s^{\min} of 6 fm.

performed and random background, mostly due to β decaying beam nuclei, is effectively suppressed to almost negligible levels. In addition, using the position and energy information from the CD detector the kinematics of the elastic scattering is used to distinguish scattered beam particles from recoiling target nuclei. This is shown in figure 5.4, where the measured energies of the particles are plotted versus the laboratory scattering angle for the ^{30}Mg beam ($E_b = 2.25$ MeV/u) on a natural Ni target (Oct. 2003 beam time; see table 5.4 on page 85). Two groups of events are manifest: the upper corresponding to the scattered beam nuclei and the lower to recoiling Ni isotopes.

The distinction between projectile and target recoils serves two purposes. Firstly, the knowledge of the particle type, scattering angle and energy allows for a Doppler shift correction of the γ rays measured in coincidence with this particle. Moreover, the velocity vector of the other reaction product can be deduced and a corresponding Doppler correction can also be performed, shown e.g. in figure 5.5 on the next page. Secondly, from the same information the center-of-mass scattering angle can be calculated and limits can be imposed to ensure that the safe distance requirement is fulfilled, as discussed in section 4.6 on page 61. For instance for the ^{30}Mg data only the upper group of events, corresponding to Mg ejectiles scattered into the laboratory angular range from 16° to 53° ,

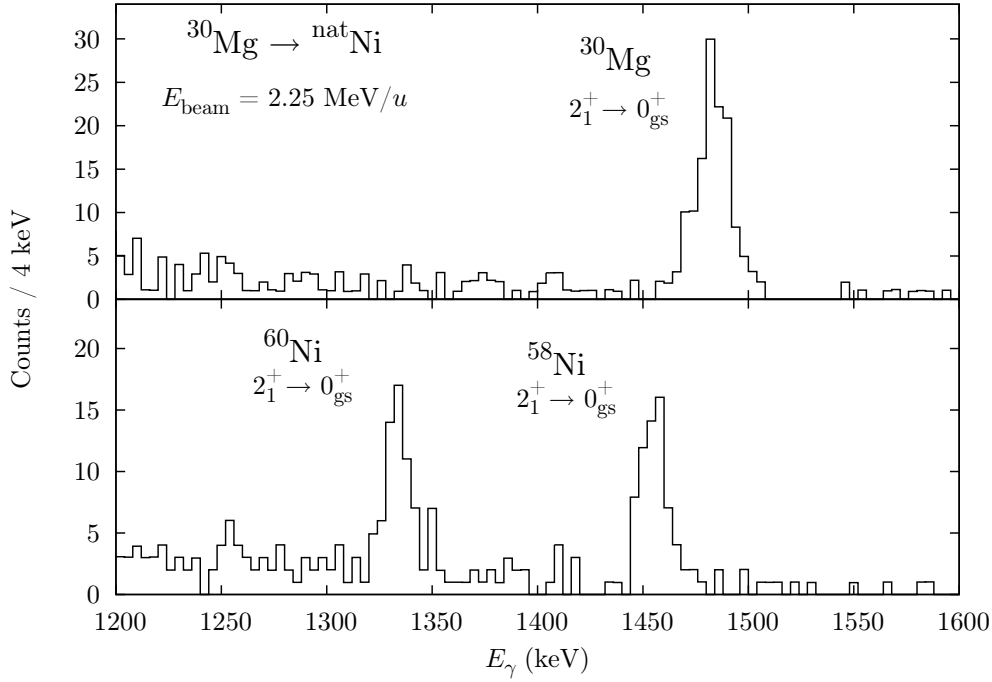


Figure 5.5: Doppler corrected γ ray energy spectra measured in the Oct. 2003 campaign with a ^{30}Mg beam at 2.25 MeV/u on a 1.0 mg/cm² natNi target, recorded in coincidence with ^{30}Mg projectiles observed in the CD detector, i.e. the upper group of events in figure 5.4 on the preceding page. The upper panel shows the spectrum with Doppler correction for ^{30}Mg and the lower for the recoiling Ni nuclei. The corresponding $2_1^+ \rightarrow 0_{\text{gs}}^+$ transitions can be seen. Doppler-smeared contributions in the spectra were avoided as explained in the text.

were analyzed, which ensured that the safe condition (equation 4.34 on page 62) was fulfilled with a minimum surface distance Δ_s^{min} of 6 fm. Indeed, when analyzing the lower events, corresponding to “unsafe” surface distances Δ_s in the range from 3.3 fm to 7 fm,³ strong γ ray transitions in ^{59}Ni and ^{61}Ni can be observed due to one-neutron-pickup of $^{58,60}\text{Ni}$ as is shown in figure 5.6.

For the calculation of the particle velocity vector it is assumed that the γ rays are emitted outside the target, i.e. after full energy loss, and that the scattering event took place in the middle of the target. Therefore, for the reconstruction of the not detected particle, say particle B, the energy of the detected particle A in the middle of the target is calculated, as well as its center-of-mass scattering angle θ_A . For particle B a center-of-mass momentum vector of $\vec{p}_B = -\vec{p}_A$ was assumed and transformed into the laboratory system.

³All radii and safe distances in this paragraph were calculated for ^{58}Ni ; for ^{60}Ni slightly (0.1 fm) smaller values are obtained.

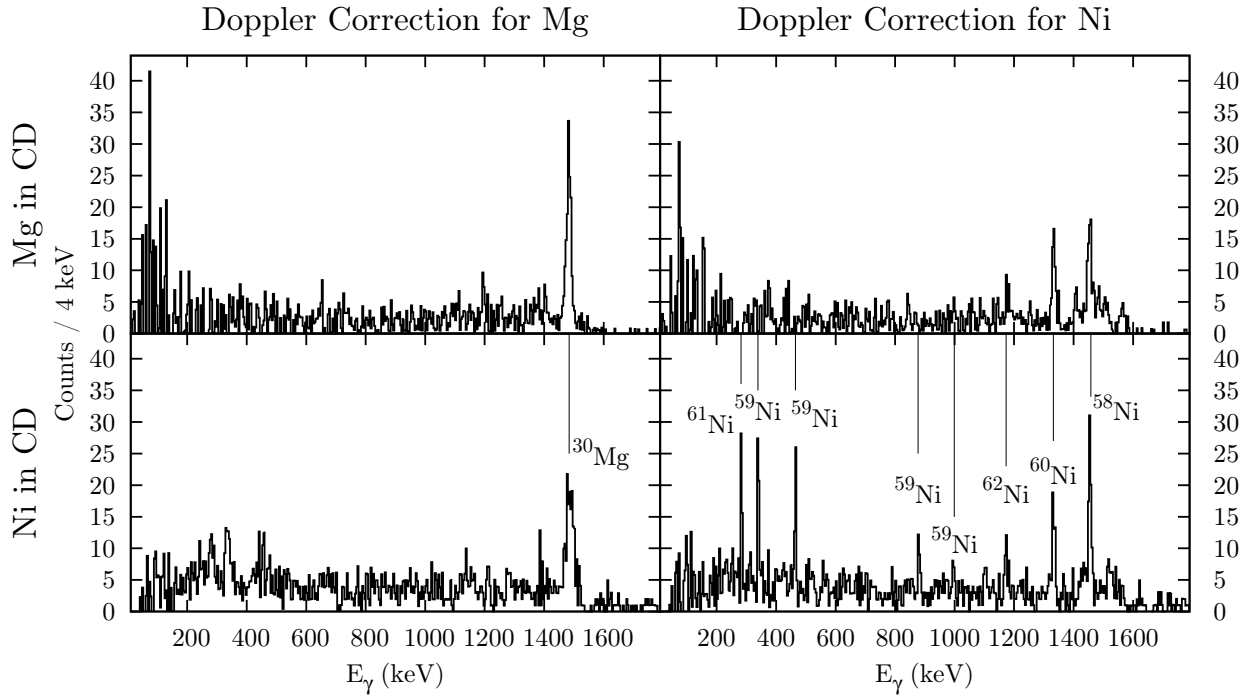


Figure 5.6: Doppler corrected γ ray energy spectra for 2.25 MeV/ u ^{30}Mg on the $^{\text{nat}}\text{Ni}$ target (Oct. 2003). The upper two panels show the same as the two panels in figure 5.5 on the preceding page (see also this caption), but with an enlarged γ ray energy scale and without avoiding the Doppler-smeared lines. The two bottom panels show data not included in the CE analysis as here the “safe” condition is not fulfilled. Indeed in the lower panels, containing only data coincident with particles in the CD which fall into the lower group in figure 5.4 on page 79, strong transitions in $^{59,61}\text{Ni}$ can be seen due to one-neutron-pickup reactions. Interestingly no line could be attributed to ^{29}Mg (left-bottom panel). The two panels on the right-hand side show Doppler correction for recoiling Ni nuclei and the panels on the left-hand side for the scattered ^{30}Mg . Random background was subtracted for all spectra.

The velocity, after considering the energy loss in half the target, was used for the Doppler correction of particle B.

An example of the Doppler corrected energy spectra obtained by this procedure is shown in figure 5.5 on page 80 for the data taken in one of the first experiments performed at REX-ISOLDE in Oct. 2003 with a ^{30}Mg beam at 2.25 MeV/ u on a 1.0 mg/cm² natNi target (see table 5.4 on page 85). The γ -ray energy spectra observed after 76 hours of data taking in coincidence with ^{30}Mg projectiles in the CD detector—i.e. the upper group in figure 5.4 on page 79—are shown, with the upper and lower panel displaying part of the Doppler-corrected spectrum assuming the γ ray emitting nucleus to be the projectile (Mg) or the recoil (Ni), respectively. The prominent peak in the upper panel observed at an energy of 1482 keV corresponds to the transition from the first 2^+ state to the ground state of ^{30}Mg , while the two lines observed at 1454 keV and 1333 keV in the bottom spectrum result from the decay of the first excited 2^+ state in ^{58}Ni and ^{60}Ni , respectively. Note that Doppler-smeared contributions of the Ni lines in the upper spectrum were avoided by suppressing events contributing to the Ni lines in the lower spectrum, and vice versa. The influence of this procedure on the line intensities was carefully investigated and resulted only in small corrections to the deduced intensity values. In both spectra the *same* events are shown only with different Doppler corrections.

After Doppler correction the peak areas were determined by fitting the peak(s) and the background typically in a region of about 20σ around the peak(s). In cases where background γ lines fall into the same energy region a separate fit of the background spectra, obtained with a shifted, enlarged, non-prompt time cut, was performed first. The results were scaled according to the widths of the prompt and non-prompt time windows, and included in the fit of the prompt spectrum. Due to the low statistics the errors σ_{x_i} on each histogram bin were assigned not as the square root of the number of counts y_i , but as the square root of the value of the fitted curve f : $\sigma_{x_i}^2 = f(x_i) \neq y_i$. With this procedure it is ensured that correct peak areas are reproduced and especially bins with zero or one count are taken into account with the correct weight [121, 122].

5.2.1 Consistency Tests

For all measurement campaigns a ^{22}Ne beam, copiously contained in the ionized residual gas of the EBIS, was used to test the method by determining its $B(\text{E}2)^\uparrow$ according to section 4.8 on page 64 and the previous section. In table 5.3 the results are compiled. It is evident that all values agree within the errors with the literature value of 230(10) $e^2\text{fm}^4$ lending confidence to the applied method.

E_b (MeV/ u)	Target, thick. ($\frac{\text{mg}}{\text{cm}^2}$)	Nuclide abundance	Normalization transition	$B(\text{E2})\uparrow$ ($e^2\text{fm}^4$)
2.25	nat.Ni, 1.0	^{58}Ni : 68.08 %	$^{58}\text{Ni}, 0_{\text{gs}}^+ \rightarrow 2_1^+$	235 (28)
		^{60}Ni : 26.22 %	$^{60}\text{Ni}, 0_{\text{gs}}^+ \rightarrow 2_1^+$	296 (75)
2.86	^{107}Ag , 1.1	^{107}Ag : 98.54 %	$^{107}\text{Ag}, \frac{1}{2}_{\text{gs}}^- \rightarrow \frac{3}{2}_1^-$	217 (23)
			$^{107}\text{Ag}, \frac{1}{2}_{\text{gs}}^- \rightarrow \frac{5}{2}_1^-$	223 (21)
Literature value [25]				230 (10)

Table 5.3: Summary of determined $B(\text{E2})\uparrow$ values for ^{22}Ne on various targets and literature value.

The above measurement can also be considered as an agreement between the calculated and measured excitation cross section (instead of the $B(\text{E2})\uparrow$) for ^{22}Ne . Due to the high count rate and the obtained statistics it was possible to measure the differential cross section $d\sigma/d\Omega$ as a function of the center-of-mass scattering angle. Very good agreement with the CE calculation was indeed observed [55, figure 5.7].

As discussed in section 5.1 on page 71 the various time structures of the REX beams make it possible to measure the beam contamination via an analysis of the release curve. If our analysis method for the beam contamination is correct, the extracted $B(\text{E2})\uparrow$ should show no (systematic) dependence on certain timing cuts; only statistical fluctuations should occur. No dependence of the extracted $B(\text{E2})\uparrow$ values on the time t_p , the time since the last proton pulse, was observed.

The extraction of the charge bred nuclei out of the EBIS takes about 100 μs with the majority of them included in a time window of only 50 μs (section 2.4 on page 14). Various gates were applied to this EBIS time; again no systematic dependency of the extracted $B(\text{E2})\uparrow$ values was found.

The $B(\text{E2})\uparrow$ of ^{22}Ne is known with a very good precision of less than 5 %, while the uncertainties in the ^{107}Ag $B(\text{E2})\uparrow$ values ($\frac{1}{2}_{\text{gs}}^- \rightarrow \frac{3}{2}_1^-$ and $\frac{1}{2}_{\text{gs}}^- \rightarrow \frac{5}{2}_1^-$) are larger as can be seen from the last column of table 5.3, where the large error derives from the uncertainty in the $B(\text{E2})\uparrow$ values of ^{107}Ag . Improved $B(\text{E2})\uparrow$ values for ^{107}Ag can therefore be deduced by using our data and the precise literature for the $B(\text{E2})\uparrow$ of ^{22}Ne . The weighted averages of the $B(\text{E2})\uparrow$ values of ^{107}Ag from previous CE results in the literature and the results from this measurement were used in the analysis of the ^{32}Mg data, where a ^{107}Ag target was employed.

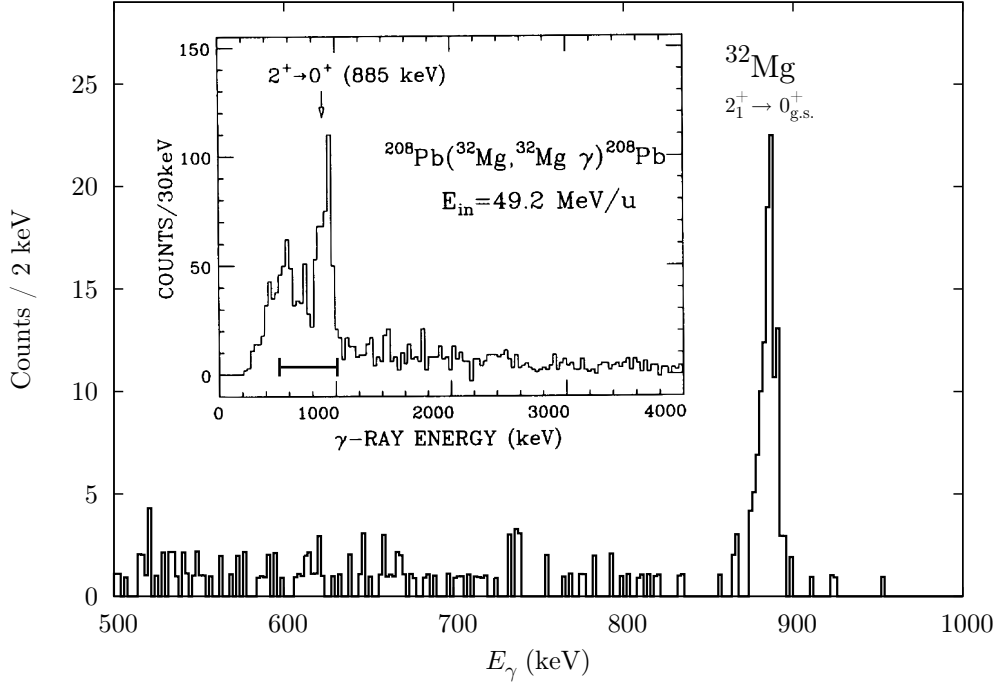


Figure 5.7: Doppler corrected (for Mg) γ ray energy spectrum obtained with a ^{32}Mg beam at 2.84 MeV/u on a ^{107}Ag target (see table 5.4 on the facing page). The inset shows the spectrum of Motobayashi *et al.* [51] obtained with intermediate-energy Coulomb excitation. The difference in resolution and background are strikingly evident. Please note the different energy scales, indicated by (H) in the inset.

5.3 Results

The results of the two measurement campaigns in Oct. 2003 and Sept. 2004 are compiled in table 5.4 on the next page with the final $B(E2; 0_{\text{gs}}^+ \rightarrow 2_1^+)$ values for ^{30}Mg and ^{32}Mg in bold. Before discussing the results in the next chapter one of the highlights of the experimental campaigns at REX-ISOLDE should be pointed out, the Coulomb excitation of ^{32}Mg already aimed at in the original REX proposal [9] from 1994. In figure 5.7 the spectrum with Doppler correction for the scattered ^{32}Mg is shown, exhibiting a sharp peak with excellent resolution and essentially no background (no random subtraction was performed). This should be compared to the spectrum shown in the inset, where the result of a study of ^{32}Mg with intermediate-energy beams is shown [51]: while the 885 keV transition is evident, the resolution is poor and a strong background is present reaching up to several MeV in γ ray energy.

As discussed in section 4.4 on page 60 the Coulomb excitation cross section is only in first order proportional to the $B(E2)_{\uparrow}$ value. The re-orientation effect is the strongest

Campaign	Nuclide	E_{beam} (MeV/ u)	I_b (Mg) 10^3 s^{-1}	t_m h	Target, thick. ($\frac{\text{mg}}{\text{cm}^2}$)	Normalization transition	σ^{p} (mb)	$B(\text{E}2)\uparrow$ ($e^2\text{fm}^4$)	$\sigma_{\text{stat.}}$ ($e^2\text{fm}^4$)	$\sigma_{\text{sys.}}$ ($e^2\text{fm}^4$)
Oct. 2003	^{30}Mg	2.25	~ 20	~ 72	nat. Ni, 1.0	$^{58}\text{Ni}, 0_{\text{gs}}^+ \rightarrow 2_1^+$ $^{60}\text{Ni}, 0_{\text{gs}}^+ \rightarrow 2_1^+$ weighted average	37	278 (54) 223 (38) 241 (31)	51 37 30	16 10 8
Sept. 2004	^{30}Mg	2.69	~ 26	~ 48	^{60}Ni , 3.85	$^{60}\text{Ni}, 0_{\text{gs}}^+ \rightarrow 2_1^+$	26	251 (27)	24	12
Sept. 2004	^{30}Mg	2.69	~ 26	~ 13	^{107}Ag , 4.4	$^{107}\text{Ag}, \frac{1}{2}_{\text{gs}}^- \rightarrow \frac{3}{2}_1^-$ $^{107}\text{Ag}, \frac{1}{2}_{\text{gs}}^- \rightarrow \frac{5}{2}_1^-$ weighted average		279 (66) 304 (71) 291 (48)	63 69 47	20 19 14
—	^{30}Mg	—	—	—	—	global w. average		253 (21)	18	12
Sept. 2004	^{32}Mg	2.84	~ 1.3	~ 60	^{107}Ag , 4.4	$^{107}\text{Ag}, \frac{1}{2}_{\text{gs}}^- \rightarrow \frac{3}{2}_1^-$ $^{107}\text{Ag}, \frac{1}{2}_{\text{gs}}^- \rightarrow \frac{5}{2}_1^-$ weighted average	236	427 (64) 441 (64) 434 (52)	50 50 35	40 39 39
	^{32}Mg									

Table 5.4: Summary of the experimental campaigns including the beam parameters and the final results. The given beam intensities I_b are only rough estimates, as are the listed durations of the measurements t_m , and do not include possible contaminants. The charge states of the beams were 7+ for ^{30}Mg and 9+ for ^{32}Mg . Statistical $\sigma_{\text{stat.}}$ and systematical $\sigma_{\text{sys.}}$ uncertainties are given in the rightmost two columns. The excitation energies of the first 2^+ states $E(2_1^+)$ in ^{30}Mg and ^{32}Mg are 885 keV and 1482 keV, respectively. An approximate projectile excitation cross section σ^{p} is given in the eighth column. It corresponds to the differential cross section integrated over the angular range of the CD detector used in the analysis (see text).

Nuclide	assumed $Q(2^+)$	$B(E2)\uparrow$ ($e^2\text{fm}^4$)
^{30}Mg	$Q_{2^+}^{\text{rot}}$ (prolate)	251 (27)
	0	239 (25)
	$Q_{2^+}^{\text{rot}}$ (oblate)	227 (24)
^{32}Mg	$Q_{2^+}^{\text{rot}}$ (prolate)	427 (63)
	0	402 (59)
	$Q_{2^+}^{\text{rot}}$ (oblate)	381 (56)

Table 5.5: The influence of the assumed $Q(2^+)$ on the extracted $B(E2)\uparrow$ value is shown.

second order effect due to the diagonal matrix elements proportional to the quadrupole moment of the 2^+ state $Q(2^+)$. Its influence on the extracted $B(E2)\uparrow$ results was tested by performing coupled channel calculations (see section 4.2 on page 54) assuming a vanishing quadrupole moment and a quadrupole moment according to the rotational model [26, 27] with a prolate $Q_0 > 0$ and an oblate $Q_0 < 0$ intrinsic deformation. The results are shown in table 5.5. As can be seen the differences in the $B(E2)\uparrow$ values are within the one σ uncertainties. For the final result we assumed a prolate intrinsic shape, which is the best estimate according to most of the model calculations, according to systematics and the general preponderance of prolate deformation.

For further details on the analysis and the results see [114, 116, 123–125] and the dissertation of O. Niedermaier [55].

Chapter 6

$^{30,32}\text{Mg}$ and the “Island of Inversion”

The results presented in the previous chapter will be summarized and compared to those obtained by other techniques; differences and their possible origin will be discussed. Furthermore selected model predictions as well as the origin of the changes in the shell structure near the “Island of Inversion” will be examined.

6.1 Experimental Results

The $B(E2; 0_{\text{gs}}^+ \rightarrow 2_1^+)$ values obtained with REX-ISOLDE and MINIBALL (solid circles) for the very neutron-rich even- A Mg isotopes are compiled in table 6.1 on the next page together with previous results, obtained by intermediate-energy Coulomb excitation (open circles) and direct life-time measurement of the 2^+ state (square). They are graphically displayed in figure 6.1 on page 89 by the full (“safe” Coulomb excitation) and open (intermediate energy Coulomb excitation) circles. Comparing these results it is evident that for both isotopes, ^{30}Mg and ^{32}Mg , there is no agreement of our results with the values measured at GANIL [53] which are larger by 70 % and 40 %, respectively. The source of this large discrepancy is not understood, and will be discussed later in this section. The two values measured at RIKEN in two separate experiments [51, 54] for ^{32}Mg are in excellent agreement with our result, while the value extracted by the MSU group [52] agrees with the present and the RIKEN values better, if the same analysis method as employed by the RIKEN group is used. In its γ ray spectra the MSU group observed, however, a transition *feeding* the first 2^+ state in ^{32}Mg which, when taken into account properly, reduces the extracted $B(E2)\uparrow$ value to the final (smaller) result. Due to its large uncertainty this value is still consistent with the present result—the same can be said about the preliminary $B(E2)\uparrow$ deduced by H. Mach *et al.* [126] as it agrees perfectly (including the error) with

Isotope	RIKEN		MSU	GANIL	ISOLDE	REX-ISOLDE	adopted
	[51]	[54]	[52]	[53]	[126]	this work	
³⁰ Mg	—	—	295 (26)	435 (58) [†]	—	253 (21)²	270 (16)
³² Mg	454 (78)	449 (53)	333 (70) 440 (55) ^{1†}	622 (90) [†]	327 (87)	434 (52)	413 (29)
³⁴ Mg	—	631 (126)	<670	—	—	—	631 (126)
E_b (MeV/ u)	49.2	45	36–58	32	—	2.25–2.84	—
target	²⁰⁸ Pb	Pb	¹⁹⁷ Au	²⁰⁸ Pb	—	^{nat} Ni, ⁶⁰ Ni, ¹⁰⁷ Ag	—

Table 6.1: Compilation of the $B(E2; 0_{\text{gs}}^+ \rightarrow 2_1^+)$ values from REX-ISOLDE/MINIBALL (bold) and results from the literature. The RIKEN, MSU, and GANIL results were obtained by intermediate-energy Coulomb excitation. In contrast at REX-ISOLDE “safe” Coulomb excitation was employed. The laboratory beam energies and targets are listed in the bottom two rows. The beam energies for the MSU measurements were 36, 58 and 51 MeV/ u for ^{30,32,34}Mg, respectively. Please see table 5.4 on page 85 for the details on the present REX-ISOLDE/MINIBALL results. The ISOLDE result by H. Mach *et al.* [126] corresponds to a preliminary value obtained from a direct life-time measurement of the 2_1^+ state of ³²Mg. The values given in the last column are adopted and correspond to a weighted average of all results shown in the table, except both GANIL results and except the MSU result without feeding correction.

¹Without feeding correction.

²Partly published in [114].

[†]Ignored for adopted value.

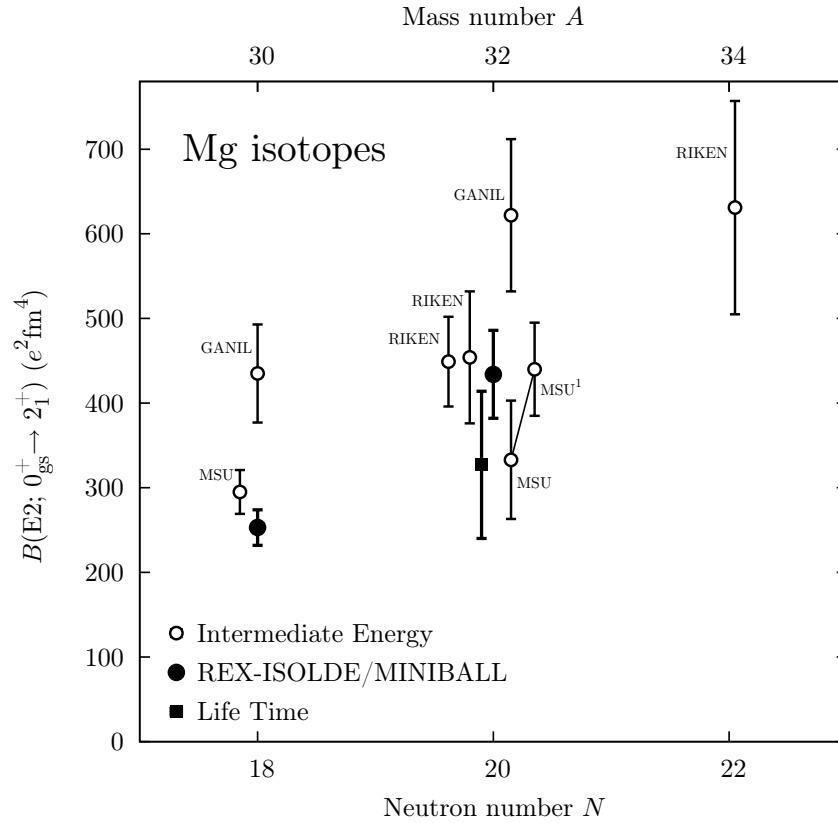


Figure 6.1: Experimental $B(E2; 0_{gs}^+ \rightarrow 2_1^+)$ values. Shown are the results of this work (filled circles) and results obtained at intermediate energies (open circles labeled by the laboratory where the measurement was performed). The square symbol shows the value deduced from the life-time measurement of H. Mach *et al.* [126]. The two MSU values shown for ^{32}Mg connected by the thin line correspond to the same data, but analyzed differently; the lower value is their final result [52]. The other references are [51, 53, 54].

¹Without feeding correction (see text and table 6.1 on the facing page).

the MSU result. While the RIKEN group takes possible feeding into account in its analysis it did not discern the feeding transition observed at MSU [52]. No feeding was observed by the MSU group for ^{30}Mg and the resulting $B(\text{E2}; 0_{\text{gs}}^+ \rightarrow 2_1^+)$ value, while slightly larger than the present one, is still compatible with it.

The compatibility between the present REX-ISOLDE and the MSU results for ^{30}Mg is evidence that this isotope is indeed prolate deformed (with $Q(2_1^+) < 0$), as was assumed in the analysis. Any other assumption about the quadrupole moment of the 2^+ state $Q(2^+)$ would lessen the agreement (confer table 5.5 on page 86). In particular there would be no agreement with the MSU result if an oblate intrinsic deformation was assumed.

In searching for possible sources of the discrepancy of our and the GANIL results it should be noted that in intermediate-energy measurements at beam energies around 30–50 MeV/ u several effects can influence the deduced $B(\text{E2})\uparrow$ values. As shown and discussed in section 4.7 on page 63 not only is the beam energy far above the Coulomb barrier, therefore giving rise to Coulomb-nuclear interference effects (see figure 6.2 on the next page), but also due to the short collision time 2^+ (or even 1^-) states with very high excitation energy (5–10 MeV) can be directly populated in a one-step process. Feeding transitions from such states to the first excited 2^+ state are likely to result in an increased deduced $B(\text{E2})\uparrow$, as the latter is determined from the γ ray yield of the $2_1^+ \rightarrow 0_{\text{gs}}^+$ transition. The influence of this effect is debated in the literature. While in recent publications it is pointed out that feeding should be negligible [127, 128], such feeding was observed in at least one experiment (MSU) [52], as discussed above. Even though no feeding was observed in the γ ray energy spectra obtained at GANIL [53], feeding is considered by a coupled-channel calculation (ECIS94) including not only the Coulomb but also the nuclear interaction. The resulting feeding corrections for ^{30}Mg and ^{32}Mg are 12.5 % and 8 %, respectively. These were obtained by performing the calculation for ^{24}Mg and scaling the *calculated* feeding (21 %) by the neutron separation energy. It is surprising that despite these significant corrections the resultant $B(\text{E2})\uparrow$ values are still by far the largest for both isotopes $^{30,32}\text{Mg}$. Due to these large deviations from all other results the GANIL values were not included in the adopted weighted average listed in table 6.1 on page 88.

While feeding and nuclear interference effects may account for the slightly larger MSU value for ^{30}Mg as compared to the present one, it is questionable if uncertainties in their estimate can be the cause for the large $B(\text{E2})\uparrow$ values measured at GANIL. The present REX-ISOLDE/MINIBALL results, on the other hand, which are based on the well established technique of Coulomb excitation with beam energies well below the Coulomb barrier, are safe with regard to nuclear interference effects and are barely influenced by real or virtual excitations of higher lying states; moreover, due to the relative measurement

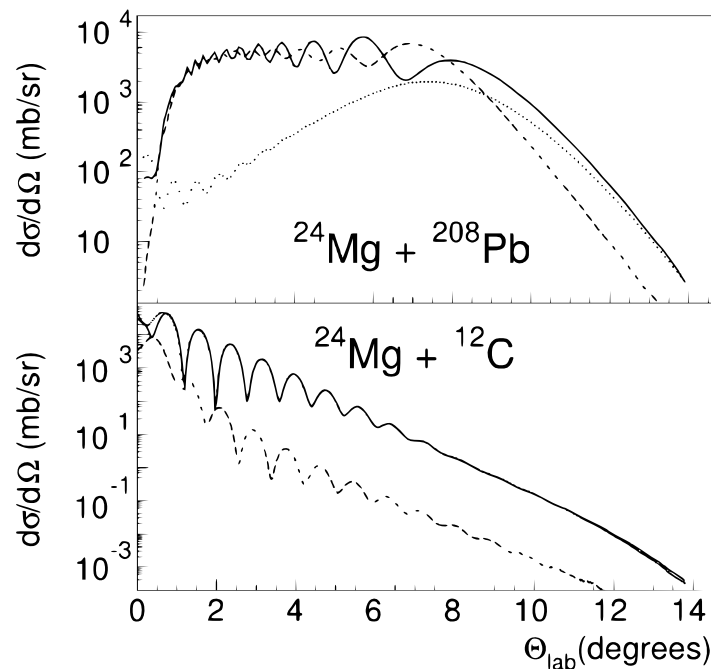


Figure 6.2: Coupled channel (ECIS) calculations of the differential cross section to excite the 2_1^+ state of ^{24}Mg incident with an energy of 32 MeV/ u on ^{208}Pb and ^{12}C targets (from [53]). The solid, dashed and dotted lines correspond to the total cross section and to the cross section with only Coulomb and only nuclear interaction enabled in the calculation, respectively. See [53] for details. The effect of Coulomb nuclear interference is evident and variations in the cross section with θ_{lab} can be as large as a factor of two.

of projectile to target excitation they are largely insensitive to systematic experimental uncertainties.

In the following the weighted averages of the $B(E2)\uparrow$ values in table 6.1 on page 88, with the exception of the GANIL results and the MSU result without feeding, are adopted, which are listed in the last column.

6.2 Experiment and Theory

The theoretical interest in the structure of the nuclei near the “Island of Inversion” has been increasing enormously. The ever growing computational capabilities allow for large scale shell model calculations thought impossible a few years ago (see the recent review articles [129–131]). New techniques and algorithms and the growing sophistication of

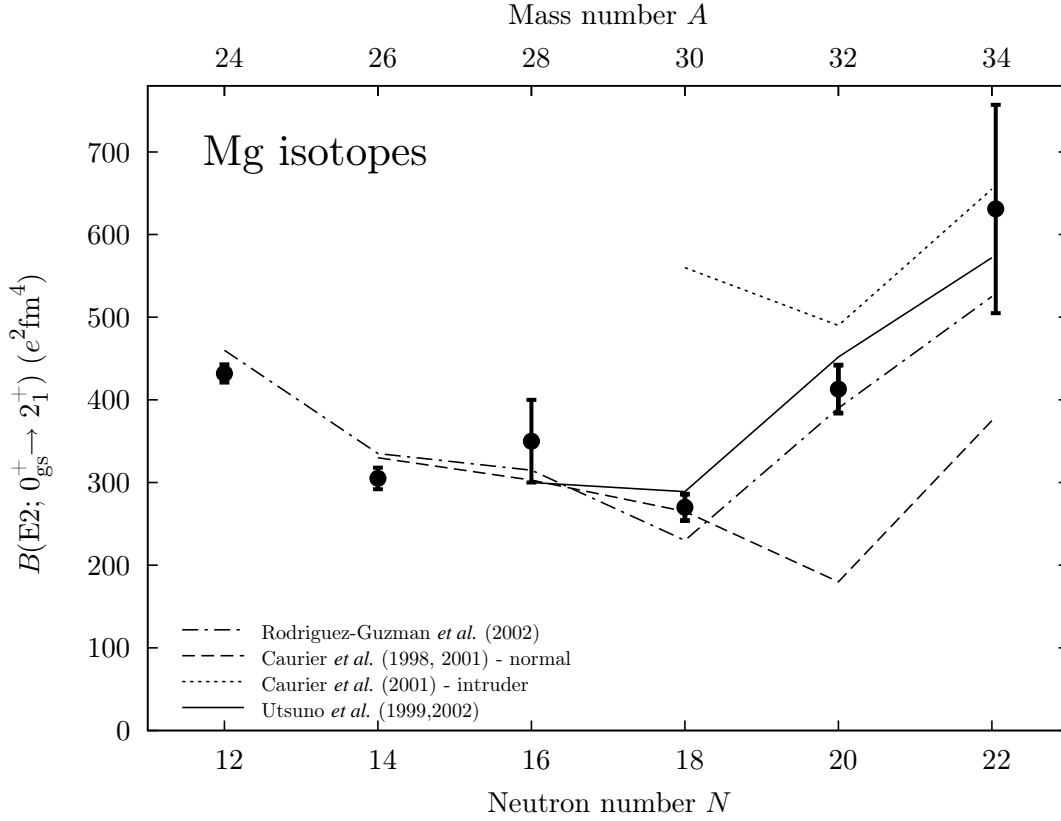


Figure 6.3: Experimental $B(E2; 0_{gs}^+ \rightarrow 2_1^+)$ values of the even- A Mg isotopes from neutron number 12 to 22 and selected model pre- and postdictions; see text.

numerical methods have enlarged the scope of the feasible theoretical studies. However, the current interest is not only driven by these new possibilities but also by the new data available—such as the present ones—due to the commissioning of new radioactive nuclear beam facilities, such as REX-ISOLDE, and new experimental devices. As there are more than 20 publications on this subject within the last seven years alone [130–152] only a selected number of them can be discussed here in some detail.

In figure 6.3 the experimental $B(E2)^\uparrow$ values for the even- A Mg isotopes from the stable ^{24}Mg to ^{34}Mg (8 neutrons from stability) are shown, together with results of selected theoretical publications. Shell model calculation were performed by Caurier *et al.* [132, 138] using the full sd model space for the protons and the $sd\bar{f}p$ model space¹ for the neutrons with the important limitation that the number of neutrons in the sd shell and pf shell

¹They are not really clear about this in their publications. In [138] it is stated that the same valence space is used as in [132], where the reader is referred to their “previous work” [153], which deals, however, with nuclei near $N = 28$ and only the pf shell is allowed for $(N - 20)$ neutrons. It is not clear how this applies to the present $sd\bar{f}p$ case.

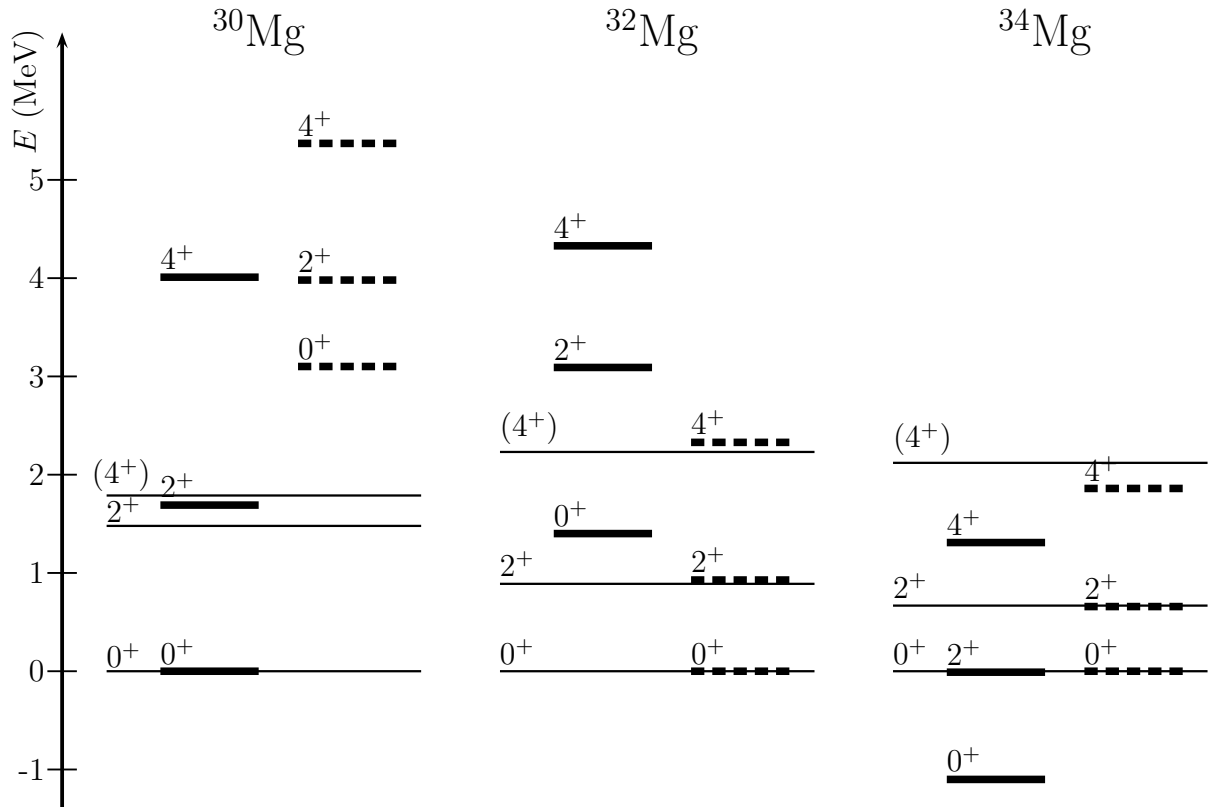


Figure 6.4: Experimental and theoretical level schemes according to Caurier *et al.* [138]. The thin lines correspond to the experimental level energies with the ground state at zero energy. The thick solid and dashed lines are the energies of the “normal” and “intruder” configurations according to [138], respectively. The theoretical levels are drawn so that the “normal” ground state for ^{30}Mg and the “intruder” ground states for the other two isotopes are located at zero energy. The calculation does not reproduce the “intruder” ground state of ^{34}Mg . See figure 6.3 on the preceding page for a comparison of the reduced transition probabilities $B(E2)\uparrow$.

was fixed. Therefore there are two different curves shown in figure 6.3 on page 92: the dashed curve corresponds to the “normal” configurations, i.e. two (zero) neutron holes in the sd shell for ^{30}Mg (^{32}Mg) and two neutrons in the pf shell for ^{34}Mg ; the dotted curve on the other hand corresponds to the situation with a $2p-4h$,² a $2p-2h$, and a $4p-2h$ neutron configuration for $^{30,32,34}\text{Mg}$, respectively, the “intruder configurations”. It is clear that the true physical states will be mixtures of these two cases and could in principle produce any $B(E2)\uparrow$ value between the dashed and the dotted curves. From the data shown in the figure it is evident that ^{30}Mg is best described by the (pure) “normal” configuration, while ^{32}Mg and ^{34}Mg agree reasonably well with the pure “intruder” result, so that any mixing, if present, must be small [138]. Furthermore the 2_1^+ excitation energies calculated by Caurier *et al.* agree well with the measured energies for the “normal” configuration of ^{30}Mg and the “intruder” configurations for $^{32,34}\text{Mg}$ as shown in figure 6.4 on the preceding page. There is very good agreement concerning the level energies and the transition strengths for ^{30}Mg (neglecting the not well known 4^+ state), ^{32}Mg and also for ^{34}Mg , provided the results are compared to the “normal” (^{30}Mg) and “intruder” ($^{32,34}\text{Mg}$) configuration. The only caveat is that Caurier *et al.* predict the “normal” ground state for ^{34}Mg to be about 1 MeV lower than the “intruder”, which is instead favored by the experiment as being the ground state.

In the calculation by Utsuno *et al.* [135, 145] the mixing of these configurations was explicitly considered. This was computationally feasible by employing the so-called Monte Carlo shell model (MCSM) or, recently, the quantum Monte Carlo diagonalization, which effectively performs an “importance” truncation of the pf shell model space (see [130] for a review), while keeping the full sd shell. The effective interaction (SDPF-M) used was constructed from the universal sd (USD) interaction [1], the Kuo-Brown interaction in the pf shell [154] and the Millener-Kurath cross shell interaction [155] with some modification outlined in [135, 139, 145] to account for the enlarged model space in relation to that of (the fit of) the original interaction. Their results, shown by the solid line, agree very well with the data. From their wave function they can easily calculate the average number of neutrons excited from the sd to the pf shells for the ground states: they obtain numbers of 0.3, 2.1, and 1.8 for $^{30,32,34}\text{Mg}$, respectively, in very good agreement with the more qualitative arguments presented above based on the calculation of Caurier *et al.* [138]. In a more recent publication the onset of intruder ground states in the neutron-rich Na isotopes ($Z = 11$) was investigated and a similar result was obtained [147] with even a small $4p-4h$ contribution to the wave function at $N = 20$. The level energies— 2_1^+ and 4_1^+ , where known—are all well reproduced. Interestingly, the authors trace the (unusual) swift

²i.e. two particles in the pf shell and four holes in the sd shell

change in shell structure when going from the stable to the most exotic Mg isotopes to the spin-isospin dependent part of the nucleon-nucleon interaction [140], which seems to be driving a general mechanism responsible for the appearance of new and the disappearance of well-known shell closures throughout the nuclear chart, as discussed in more detail in section 6.3 on page 97.

Most other approaches taken in the recent literature to describe the nuclides near the “Island of Inversion” start from the mean field and incorporate correlations by several means. Particularly successful is the work of Rodríguez-Guzmán *et al.* [142], which is shown in figure 6.3 on page 92 by the dash-dotted line. These results were obtained with the angular momentum projected generator coordinate method (AMPGCM) with the axially symmetric quadrupole moment as the generating coordinate. An introduction to this method can be found in [156].

Other approaches (not shown in the figure) include anti-symmetrized molecular dynamics (AMD) [144, 150], constrained Hartree-Fock-Bogoliubov (HFB) [136, 157], HFB with quasi random phase approximation (QRPA) [148], and relativistic mean field (RMF) studies [158]. Most of these pre- and postdictions can reproduce the large $B(E2)\uparrow$ of ^{32}Mg , while some of them fail, e.g. the recent mean field calculations with the separable monopole interaction [143] agrees with the experimental value for ^{32}Mg but cannot reproduce the trend of the data for the neighboring isotopes (shown in figure 1.2 on page 7). The reason for the large collectivity of ^{32}Mg is debated as well as the nature of the 2^+ excitation. Pèru *et al.* [136] found that ^{32}Mg is always spherical at the mean field level, but vibration-rotation coupling yields a deformed ground state of ^{32}Mg . The HFB+QRPA results by Yamagami *et al.* [148] can reproduce a large $B(E2)\uparrow$ of ^{32}Mg *without* deformation, but only if pairing is “enabled” in the calculation. In contrast, most other calculations predict ^{32}Mg to be statically prolate deformed. Unfortunately many publications only report on results near the “Island of Inversion” or even only for ^{32}Mg ; a much more meaningful judgement of the models can be made if a chain of isotopes is calculated from the stable nuclei to the most exotic. An introduction to some of the above mentioned theoretical methods can be found in [94, 156, 159].

Interesting is also a comparison of the present $B(E2)\uparrow$ values with values derived from systematics such as studied by Grodzins [24], where the $B(E2)\uparrow$ is predicted using an expression containing the energy of the transition E , the mass number A and the charge number Z . The most recent empirical fit was performed by Raman *et al.* [25] with the following result

$$B(E2)\uparrow = (2.57 \pm 0.45) E^{-1} Z^2 A^{-2/3} . \quad (6.1)$$

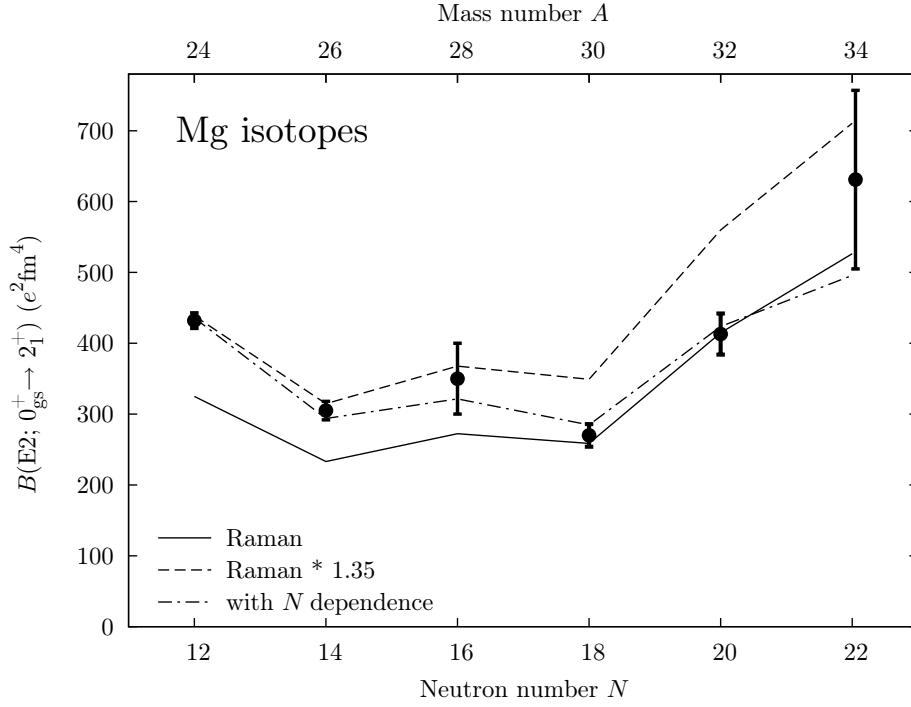


Figure 6.5: Experimental $B(E2; 0_{\text{gs}}^+ \rightarrow 2_1^+)$ values of the even- A Mg isotopes from neutron number 12 to 22 and Raman’s predictions [25] based on the work of Grodzins [24] are shown. A curve scaled by 1.35 and an unscaled one are shown. Also plotted is a curve from [160, 161] with an explicit dependence on neutron number N , which reproduces the data very well.

The Z and E dependence was already derived, though with a different A dependence and very different factors of proportionality, by Bohr and Mottelson [26] for the irrotational flow models with small oscillations around the equilibrium and also for collective rotations of axially symmetric nuclei. It was pointed out in [25] that for some (especially lighter) isotopes a better fit is obtained by scaling the above result. The not scaled result and the one scaled by a factor of 1.35 to reproduce the data for the stable isotopes $^{24,26}\text{Mg}$ are shown in figure 6.5. Surprisingly the unscaled result (solid line) reproduces the data for the exotic nuclei near $N = 20$ very well, but fails for the stable isotopes. The curve scaled (dashed line) to reproduce the values near stability now (obviously) fails for the exotic nuclei.

A modified version of equation 6.1 has been proposed [160, 161] which should better reproduce the observed dependence on the neutron-excess. The following equation

$$B(E2)\uparrow = (2.57 \pm 0.45) E^{-1} Z^2 A^{-2/3} (1.288 - 0.088(N - \bar{N})) \quad (6.2)$$

with the average neutron number \bar{N} for given A defined as

$$\bar{N} = \frac{A}{2} \frac{1 + 0.0128 A^{2/3}}{1 + 0.0064 A^{2/3}} \quad (6.3)$$

is also shown (dot-dashed line) and reproduces the measured data surprisingly well. The new functional form should account for a possible decoupling of a neutron skin or halo from the core, giving rise to a large iso-vector components in the wave function and different deformations of the nuclear core and the “surrounding” neutron skin [161].

It is evident that such relation can be used to deduce approximate $B(E2)\uparrow$ values far from stability if the energy of the first 2^+ state is known, but a measurement of the $B(E2)\uparrow$ value is not yet feasible.

6.3 On the Evolution of the Shell Structure

As was discussed in the introductory chapter 1 the nuclear shell structure as it is known from any nuclear physics text book (e.g. [26, 94, 162, 163]) is not rigidly predetermined throughout the nuclear chart, but it is subject to change with proton and neutron number Z and N or equivalently with mass number A and neutron excess $(N - Z)/A$ and *shell occupation*. One consequence is that the well known magic proton and neutron numbers are in fact corresponding to closed shells only near the valley of stability. Why this is so shall shortly be discussed in this section.

The dependence on A can be understood in terms of the mean field. Due to the changing radial extension of the wave functions there is a relative increase in binding for the high- l orbitals. A softening of the Woods-Saxon shape of the neutron potential caused by increasing neutron-excess, on the other hand, results in a rising of high- l orbitals (similar to the shift of the single particle energies when going from a (3D) square well potential to a harmonic oscillator). This is graphically represented in figure 6.6 on the next page from [164]. Another well known effect is the weakening of the spin-orbit splitting, being proportional to the radial derivative of the potential. All of the above effects, however, depend smoothly and only weakly on the “parameters” A and $(N - Z)/A$. Thus, a change in shell structure cannot happen unless extraordinary changes of their value occur [165] and the extremely rapid changes in shell structure near the “Island of Inversion” cannot be explained by this reasoning.

A different explanation has been proposed, based on the so-called monopole shift of particular shell model orbits [140, 165, 166], i.e. the change in shell structure is attributed to a change of the *residual* interaction with shell occupation and not to changes in the mean

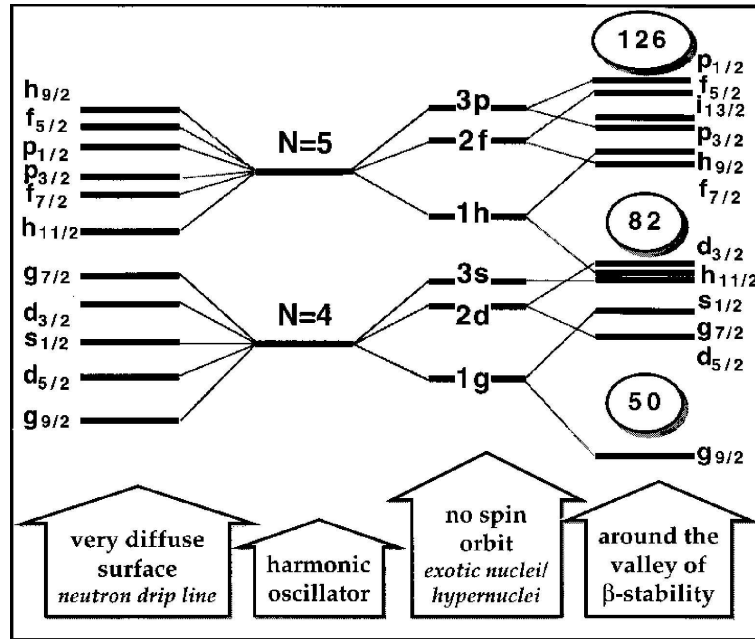


Figure 6.6: Nuclear single-particle levels for various potentials (from [164]). The well known shell structure is shown on the far right-hand side, while the middle right-hand panel shows a possible scenario for “exotic nuclei” with a weakened spin-orbit potential. At the extremes of nuclear stability a “flat” shell structure might emerge (far left-hand side). See [164] for details.

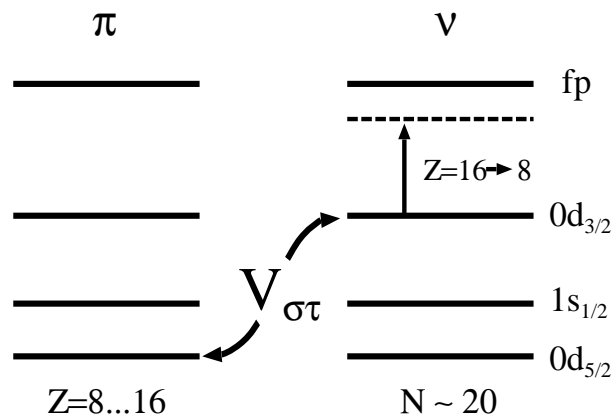


Figure 6.7: Illustration of monopole shift of the effective single particle energies (see text).

field. The shift in the effective single particle energies with changing occupation numbers can easily be calculated within the shell model [165, section 5] and the largest shifts were observed for proton-neutron spin-flip partners, such as $\nu d_{3/2} - \pi d_{5/2}$ orbitals relevant for the present case. The source of this remarkably large shift could be traced back to the $(\sigma \cdot \sigma)(\tau \cdot \tau)$ in-medium nucleon-nucleon interaction $V_{\sigma\tau}$. Thus, strong binding is generated by filled proton-neutron spin-orbit partner orbitals. The resultant effect is illustrated in figure 6.7 on the facing page for the nuclei of interest here. For stable nuclei near $N = 20$ the $\pi d_{5/2}$ proton orbital is filled, as is the $\nu d_{3/2}$. Due to the $V_{\sigma\tau}$ interaction there exists a strong attraction between these (spin-flip and isospin-flip) orbitals, producing the usual shell structure with a closed $N = 20$ shell, i.e. a large gap to the fp shell (solid levels in the figure). When the $\pi d_{5/2}$ orbital is emptied when going to more exotic neutron-rich nuclei (near $N = 20$) the $V_{\sigma\tau}$ interaction weakens and the $\nu d_{3/2}$ level moves up in energy (dashed level): the $N = 20$ shell vanishes completely and a new shell at $N = 14$ occurs, which is not present in stable nuclei. Only qualitative arguments are given here, see [130, 140, 152] for details.

This mechanism is expected to be active throughout the nuclear chart, as for stable isotopes often the neutron orbital with smaller angular momentum $\nu l_{<}$ is filled if the corresponding proton spin-orbit partner $\pi l_{>}$ is occupied. If the latter is emptied rapid changes in the shell structure are expected due to upward shift of the former orbitals, creating new and destroying existing shell closures, with only moderate variations of N and Z .

6.4 “Island of Inversion”

Finally, a summary of the properties of the nuclei near the “Island of Inversion” is given in the figures 6.8 on the next page, 6.9 on page 101 and 6.10 on page 102 where a nuclear chart near the “Island of Inversion” is shown. Basic properties such as the ground state spins, half-lives, Q_β values, as well as neutron-separation energies S_n are shown in figure 6.8 on the following page. The most basic $E2$ properties such as the energies of the first excited 2^+ and 4^+ states, their ratios and the $B(E2; 0_{\text{gs}}^+ \rightarrow 2_1^+)$ values for the even-even nuclides are shown in figure 6.9 on page 101. The relevant references are shown in figure 6.10 on page 102. In all three figures the color code indicates which isotope belongs to the “Island of Inversion” on the basis of the available experimental data. The present REX-ISOLDE/MINIBALL measurements as well as the here adopted values show unambiguously that ^{30}Mg is outside while ^{32}Mg is squarely inside the “Island of Inversion”, with a variation of the neutron

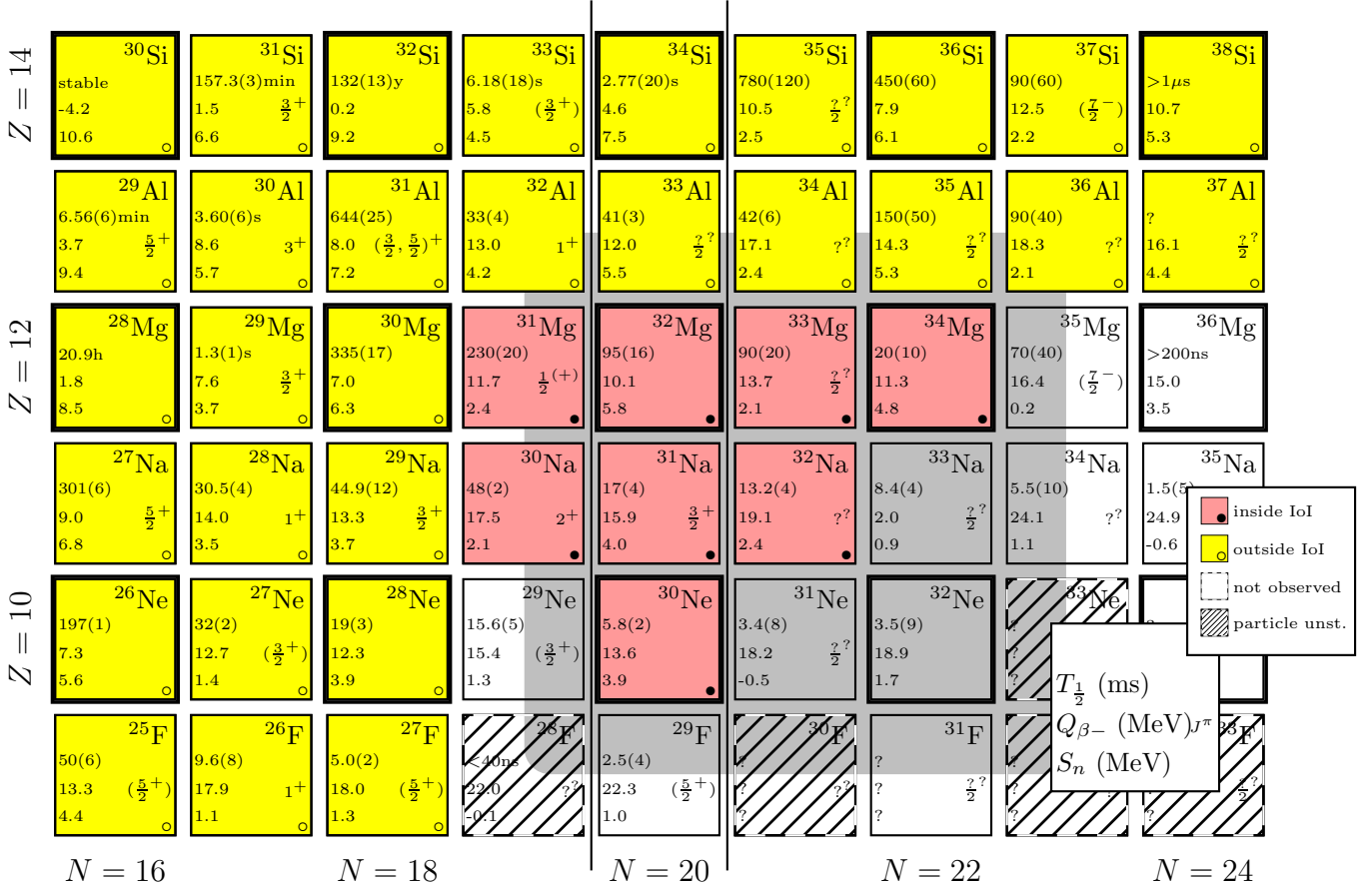


Figure 6.8: Properties of nuclei near the “Island of Inversion”. The shaded area shows the “Island of Inversion” as outlined by Warburton, Becker, Brown in 1990 [36]. The color code described in the legend on the right shows which nuclides can be considered to be inside the “Island of Inversion” on the basis of experimental evidence. Besides the ground state spin-parity J^π (except when even-even) the half-life $T_{1/2}$ of the ground state is given in ms if not otherwise specified. The β -decay Q -values ($Q_{\beta-}$) and the neutron separation energies S_n are also listed (both in MeV). Experimentally unknown values are indicated by question marks. In figure 6.9 on the facing page the $E2$ properties of these nuclei are compiled.

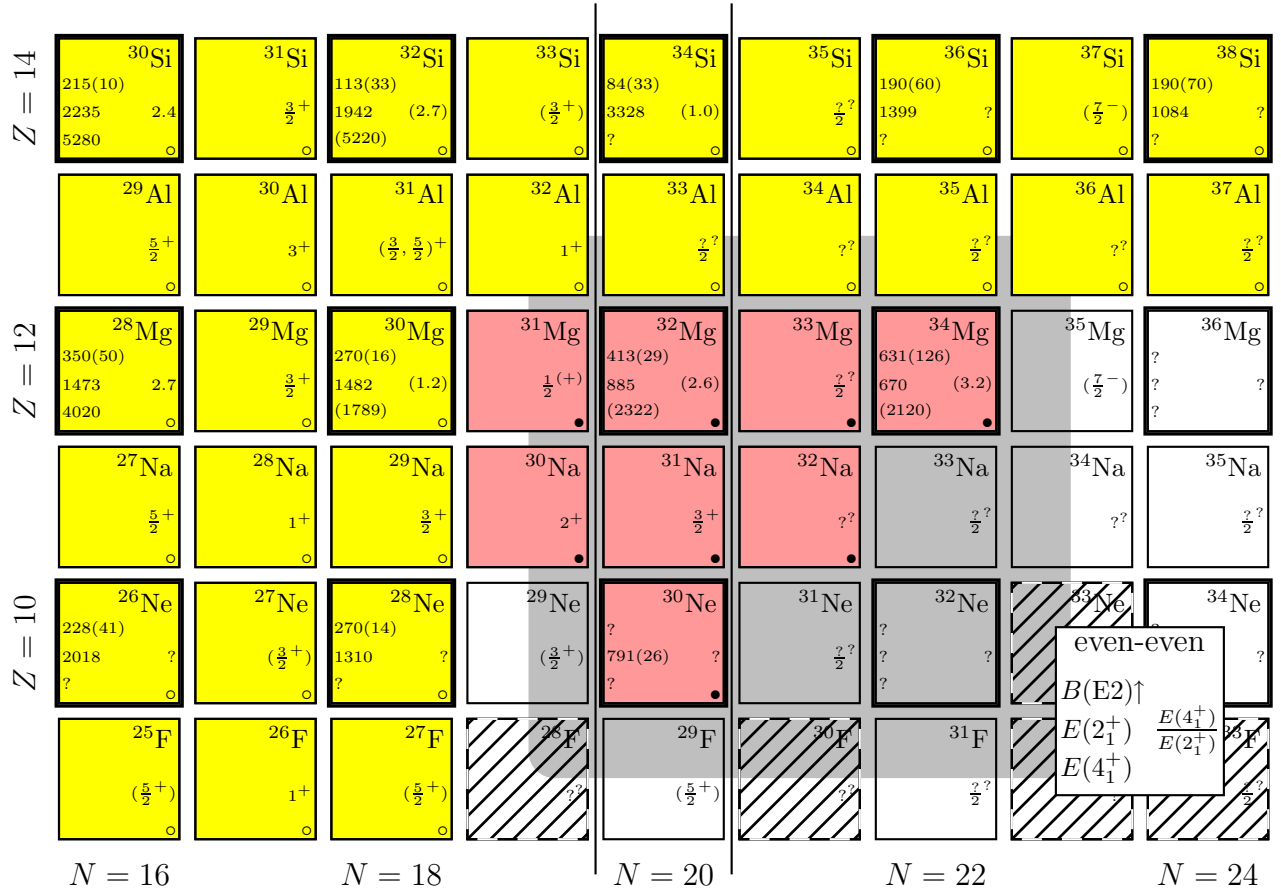


Figure 6.9: $E2$ properties of nuclei near the “Island of Inversion”. For the even- Z even- N nuclei the $B(E2)\uparrow$ values, the energies of the first 2^+ and 4^+ states and their ratios are shown. If the values for the 4_1^+ energy or the ratio are given in parenthesis then the 4^+ spin is not confirmed experimentally. The value in parenthesis after the $B(E2)\uparrow$ is its one σ uncertainty. For the odd- A and odd-odd isotopes the ground state spin is listed. See also the caption and legend of figure 6.8 on the facing page.

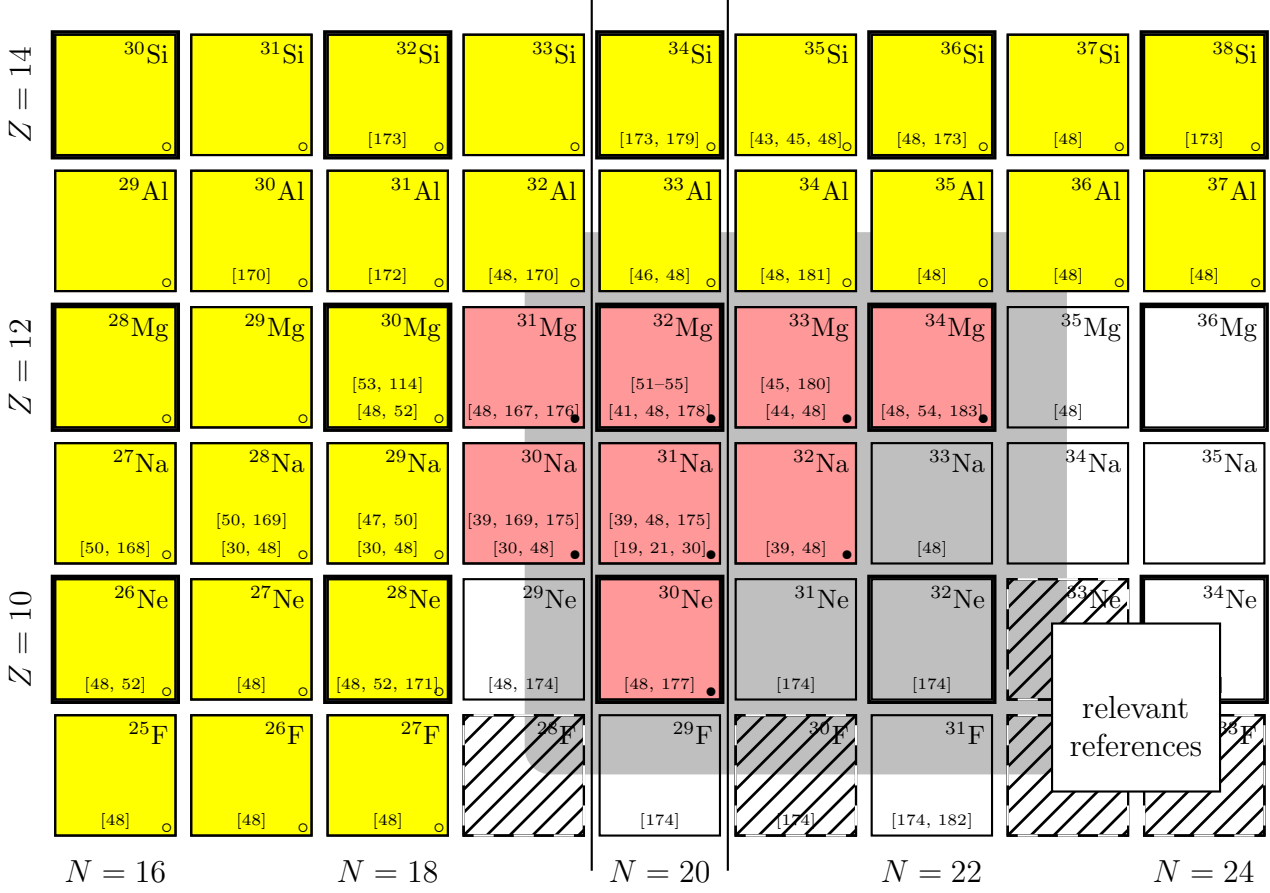


Figure 6.10: Relevant references for experimental results.

number from the first to the second isotope of only 2 units. It is evident from the figures that the available experimental data on the isotopes beyond ^{30}Ne , ^{31}Na , and ^{34}Mg is rather meager.

The spin parity of the ground state of ^{31}Mg was measured recently to be $\frac{1}{2}^+$ placing ^{31}Mg inside the “Island of Inversion”, as this measurement reveals the coexistence of $1\hbar\omega$ and $2\hbar\omega$ intruder states below 500 keV [167].

Chapter 7

Summary and Outlook

With the commissioning of the REX-ISOLDE accelerator and the MINIBALL array a new chapter in nuclear structure studies has been opened. REX, which is now in routine operation since two years, as is the MINIBALL array, provides access to re-accelerated nuclei very far from stability, exploiting the availability of more than 600 nuclides of more than 60 elements at the ISOLDE facility. MINIBALL, with its high efficiency and excellent granularity, is the ideal experimental device to be used in conjunction with the REX accelerator.

While until a few years ago only studies with stable beams or fast in-flight separated projectile fragmentation beams could be carried out, with REX and MINIBALL it is now possible to use the well known and proven tools, applicable with beams having energies around the Coulomb barrier, such as “safe” Coulomb excitation and single particle transfer reactions, to study the interplay between the single particle and collective degrees of freedom far from stability.

The results obtained till now demonstrate the power of these two new devices. In two of the first experimental campaigns carried out it was possible for the first time to obtain spectroscopic information on the very neutron-rich Mg isotopes by the model independent technique of “safe” Coulomb excitation. The $B(E2)^\uparrow$ values of $^{30,32}\text{Mg}$ can now be considered to be firmly established, placing the boundary of the “Island of Inversion” between these two isotopes for $Z = 12$. During the commissioning phase of REX and MINIBALL feasibility studies were undertaken to employ single neutron transfer reactions to study the single particle structure of neutron-rich Na and Mg isotopes. Even though the setup was by no means optimized, very promising results could be extracted [56, 184]. The construction of a setup optimized for these studies is under way opening a new route to investigate the single particle properties of exotic nuclei with REX-ISOLDE/MINIBALL.

While the REX project was started, built up and brought into operation as a regular ISOLDE experiment, once the novel charge breeding concept was proven, REX became a CERN user facility in 2004. In the same year an extension of the ISOLDE hall was completed creating additional floor space for dedicated experimental equipment, such as a recoil spectrometer for the detection of fusion products. In addition, as part of the HIE-ISOLDE¹ project [185], the REX accelerator will be extended to boost its maximum beam energy (with continuous variability down to below 1 MeV/*u*) in two steps to 4.3 MeV/*u* (2006/7) and to 10 MeV/*u* (2011), enormously enlarging the scope of possible experiments, as after the final upgrade beam energies near the Coulomb barrier can be reached for any target and beam combination.

Due to these planned energy and intensity upgrades it will be possible to extend the studies presented here to nuclei beyond ³²Mg and ²⁸Ne and possibly the long sought spherical (non-intruder) 0⁺ state of ³²Mg can be identified. This will allow for a better understanding the very rapid and unusual changes in shell structure near the “Island of Inversion”.

A new exciting era in nuclear structure research has just started.

¹High Intensity and Energy ISOLDE

Bibliography

- [1] B.A. Brown and B.H. Wildenthal. Status of the nuclear shell model. *Ann. Rev. Nucl. Part. Sci.*, 38:29, 1988.
- [2] <http://www.discover.com/issues/feb-02/cover/>.
- [3] <http://www.orau.org/ria/>.
- [4] <http://www.ganil.fr/eurisol/>.
- [5] <http://www.cyc.ucl.ac.be/>.
- [6] <http://www.phy.ornl.gov/hrifb/>.
- [7] <http://www.triumf.info/>.
- [8] <http://ganinfo.in2p3.fr/spiral/>.
- [9] D. Habs et al. Radioactive beam EXperiments at ISOLDE: Coulomb excitation and neutron transfer reactions of exotic nuclei. Proposal to the ISOLDE committee, CERN, Nov 1994. CERN-ISC-94-25, ISC-P-68.
- [10] D. Habs, O. Kester, T. Sieber, H. Bongers, S. Emhofer, P. Reiter, P.G. Thirolf, G. Bollen, J. Äystö, O. Forstner, H. Ravn, T. Nilsson, M. Oinonen, H. Simon, J. Cederkall, F. Ames, P. Schmidt, G. Huber, L. Liljeby, O. Skeppstedt, K.G. Rensfeldt, F. Wenander, B. Jonson, G. Nyman, R. von Hahn, H. Podlech, R. Repnow, C. Gund, D. Schwalm, A. Schempp, K.-U. Kühnel, C. Welsch, U. Ratzinger, G. Walter, A. Huck, K. Kruglov, M. Huyse, P. Van den Bergh, P. Van Duppen, L. Weissman, A.C. Shotter, A.N. Ostrowski, T. Davinson, P.J. Woods, J. Cub, A. Richter, and G. Schrieder. The REX-ISOLDE project. *Hyperf. Int.*, 129:43, 2000.
- [11] O. Kester, T. Sieber, S. Emhofer, F. Ames, K. Reisinger, P. Reiter, P.G. Thirolf, R. Lutter, D. Habs, B.H. Wolf, G. Huber, P. Schmidt, A.N. Ostrowski, R. von Hahn, R. Repnow, J. Fitting, M. Lauer, H. Scheit, D. Schwalm, H. Podlech, A. Schempp, U. Ratzinger, O. Forstner, F. Wenander, J. Cederkäll, T. Nilsson, M. Lindroos, H. Fynbo, S. Franchoo, U. Bergmann, M. Oinonen, J. Äystö, P. Van Den Bergh, P. Van Duppen, M. Huyse, N. Warr, D. Weisshaar, J. Eberth, B. Jonson, G. Nyman, M. Pantea, H. Simon, G. Schrieder, A. Richter, O. Tengblad, T. Davinson, P.J. Woods, G. Bollen, L. Weissmann, L. Liljeby, and K.G. Rensfeldt. Accelerated radioactive beams from REX-ISOLDE. *Nucl. Instr. Meth. B*, 204:20, 2003.

-
- [12] J. Eberth, G. Pascovici, H.G. Thomas, N. Warr, D. Weisshaar, D. Habs, P. Reiter, P. Thierolf, D. Schwalm, C. Gund, H. Scheit, M. Lauer, P. Van Duppen, S. Franchoo, M. Huyse, R.M. Lieder, W. Gast, J. Gerl, and K.P. Lieb. MINIBALL: a Ge detector array for radioactive ion beam facilities. *Prog. Part. Nucl. Phys.*, 46:389, 2001.
 - [13] Christoph Gund. Eigenschaften des zweifach segmentierten Prototypen eines MINIBALL Cluster Moduls. Diplomarbeit, Universität Heidelberg, 1997.
 - [14] Luis Palafox Gamir. *A New Method for the Determination of the Entry Position of γ rays in HPGe Detectors by Current Pulse Analysis*. PhD thesis, Cranfield University, 1997.
 - [15] Christoph Gund. *The Sixfold Segmented MINIBALL Module: Simulation and Experiment*. Dissertation, Universität Heidelberg, 2000.
 - [16] Jörg Fitting. Messung und Pulsformanalyse an einem MINIBALL-Cluster-Detektor. Diplomarbeit, Universität Heidelberg, 2002.
 - [17] Martin Lauer. Implementierung von Algorithmen zur Echtzeitpulsformanalyse von HPGe Detektorsignalen. Diplomarbeit, Universität Heidelberg, 2001.
 - [18] Martin Lauer. *Digital Signal Processing for segmented HPGe Detectors: Preprocessing Algorithms and Pulse Shape Analysis*. Dissertation, Universität Heidelberg, 2004.
 - [19] R. Klapisch, C. Thibault-Philippe, C. Détraz, J. Chaumont, R. Bernas, and E. Beck. Half-life of ^{11}Li , of ^{27}Na , and of the new isotopes ^{28}Na , ^{29}Na , ^{30}Na , and ^{31}Na produced in high-energy nuclear reactions. *Phys. Rev. Lett.*, 23:652, 1969.
 - [20] R. Klapisch, R. Prieels, C. Thibault, A. M. Poskanzer, C. Rigaud, and E. Roeckl. On-line mass-spectrometric measurement of the masses of neutron-rich sodium isotopes. *Phys. Rev. Lett.*, 31:118, 1973.
 - [21] C. Thibault, R. Klapisch, C. Rigaud, A.M. Poskanzer, R. Prieels, L. Lessard, and W. Reisdorf. Direct measurements of the masses of ^{11}Li and $^{26-32}\text{Na}$ with an on-line mass spectrometer. *Phys. Rev. C*, 12:644, 1975.
 - [22] X. Campi, H. Flocard, A.K. Kerman, and S. Koonin. Shape transitions in the neutron rich sodium isotopes. *Nucl. Phys. A*, 251:193, 1975.
 - [23] C. Détraz, M. Langevin, M.C. Goffri-Kouassi, D. Guillemaud, M. Epherre, G. Audi, C. Thibault, and F. Touchard. Mapping of the onset of a new region of deformation: the masses of ^{31}Mg and ^{32}Mg . *Nucl. Phys. A*, 394:378, 1983.
 - [24] L. Grodzins. The uniform behaviour of electric quadrupole transition probabilities from first 2^+ states in even-even nuclei. *Phys. Lett.*, 2:88, 1962.
 - [25] S. Raman, C. W. Nestor Jr., and P. Tikkanen. Transition probability from the ground to the first-excited 2^+ state of even-even nuclides. *Atom. Data and Nucl. Data Tab.*, 78:1, 2001.
 - [26] Aage Bohr and Ben R. Mottelson. *Nuclear Structure*. World Scientific, Singapore, 1998.
-

-
- [27] D. Pelte and Dirk Schwalm. *In-beam gamma-ray spectroscopy with heavy ions*, page 1. Volume 3 of Bock [75], 1982.
- [28] Dirk Schwalm. Coulomb excitation at “safe” and “unsafe” energies. page 1. World Scientific, 1994.
- [29] C. Détraz, D. Guillemaud, G. Huber, R. Klapisch, M. Langevin, F. Naulin, C. Thibault, L. C. Carraz, and F. Touchard. Beta decay of $^{27-32}\text{Na}$ and their descendants. *Phys. Rev. C*, 19:164, 1979.
- [30] G. Huber, F. Touchard, S. Büttgenbach, C. Thibault, R. Klapisch, H. T. Duong, S. Liberman, J. Pinard, J. L. Vialle, P. Juncar, and P. Jacquinet. Spins, magnetic moments, and isotope shifts of $^{21-31}\text{Na}$ by high resolution laser spectroscopy of the atomic d_1 line. *Phys. Rev. C*, 18:2342, 1978.
- [31] F. Touchard, J. M. Serre, S. Büttgenbach, P. Guimbal, R. Klapisch, M. de Saint Simon, C. Thibault, H. T. Duong, P. Juncar, S. Liberman, J. Pinard, and J. L. Vialle. Electric quadrupole moments and isotope shifts of radioactive sodium isotopes. *Phys. Rev. C*, 25:2756–2770, 1982.
- [32] A. Watt, R. P. Singhal, M. H. Storm, and R. R. Whitehead. A shell-model investigation of the binding energies of some exotic isotopes of sodium and magnesium. *J. Phys. G*, 7:L145, 1981.
- [33] B. H. Wildenthal and W. Chung. Collapse of the conventional shell-model ordering in the very-neutron-rich isotopes of Na and Mg. *Phys. Rev. C*, 22:2260, 1980.
- [34] M.H. Storm, A. Watt, and R.R. Whitehead. Crossing of single-particle energy-levels resulting from neutron excess in the sd shell. *J. Phys. G*, 9:L165, 1983.
- [35] A. Poves and J. Retamosa. The onset of deformation at the $N = 20$ neutron shell closure far from stability. *Phys. Lett. B*, 184:311, 1987.
- [36] E. K. Warburton, J. A. Becker, and B. A. Brown. Mass systematics for $A = 29 - 44$ nuclei: The deformed $A \sim 32$ region. *Phys. Rev. C*, 41:1147, 1990.
- [37] D. R. Goosman, C. N. Davids, and D. E. Alburger. Mass and β decay of the new isotope ^{29}Mg : Systematics of masses of $T_z = \frac{5}{2}$ nuclides in the $2s-1d$ shell. *Phys. Rev. C*, 8:1331, 1973.
- [38] E. Roeckl, P. F. Dittner, C. Détraz, R. Klapisch, C. Thibault, and C. Rigaud. Decay properties of the neutron-rich isotopes, ^{11}Li and $^{27-31}\text{Na}$. *Phys. Rev. C*, 10:1181, 1974.
- [39] C. Detraz, M. Epherre, D. Guillemaud, P. G. Hansen, B. Jonson, R. Klapisch, M. Langevin, S. Mattsson, F. Naulin, G. Nyman, A. M. Poskanzer, H. L. Ravn, M. de Saint-Simon, K. Takahashi, C. Thibault, and F. Touchard. Beta-delayed two-neutron emission from $^{30,31,32}\text{Na}$. *Phys. Lett. B*, 94:307, 1980.
- [40] C. Détraz, M. Langevin, D. Guillemaud-Mueller, A.C. Mueller, C. Thibault, F. Touchard,
-

- G. Klotz, C. Miehé, G. Walter, M. Epherre, and C. Richard-Serre. β -delayed α -emission from neutron-rich nuclei: the case of ^{30}Na . *Nucl. Phys. A*, 402:301, 1983.
- [41] D. Guillemaud-Mueller, C. Détraz, M. Langevin, F. Naulin, M. de Saint-Simon, C. Thibault, F. Touchard, and M. Epherre. β -decay schemes of very neutron-rich sodium isotopes and their descendants. *Nucl. Phys. A*, 426:37, 1984.
- [42] G. Klotz, P. Baumann, M. Bounajma, A. Huck, A. Knipper, G. Walter, G. Marguier, C. Richard-Serre, A. Poves, and J. Retamosa. Beta decay of $^{31,32}\text{Na}$ and ^{31}Mg : Study of the $N = 20$ shell closure. *Phys. Rev. C*, 47:2502, 1993.
- [43] S. Nummela, P. Baumann, E. Caurier, P. Dessagne, A. Jokinen, A. Knipper, G. Le Scornet, C. Miehé, F. Nowacki, M. Oinonen, Z. Radivojevic, M. Ramdhane, G. Walter, and J. Äystö. Spectroscopy of $^{34,35}\text{Si}$ by β decay: sd - fp shell gap and single-particle states. *Phys. Rev. C*, 63:44316, 2001.
- [44] S. Nummela, F. Nowacki, P. Baumann, E. Caurier, J. Cederkäll, S. Courtin, P. Dessagne, A. Jokinen, A. Knipper, G. Le Scornet, L. G. Lyapin, Ch. Miehé, M. Oinonen, E. Poirier, Z. Radivojevic, M. Ramdhane, W. H. Trzaska, G. Walter, and J. Äystö. Intruder features in the island of inversion: The case of ^{33}Mg . *Phys. Rev. C*, 64:054313, 2001.
- [45] S. Nummela, P. Baumann, E. Caurier, S. Courtin, P. Dessagne, E. Holmlund, A. Jokinen, A. Knipper, G. Le Scornet, f. C. Miehé, F. Nowacki, L. G. Lyapin, M. Oinonen, E. Poirier, Z. Radivojevic, M. Ramdhane, W. H. Trzaska, G. Walter, and J. Äystö. Study of the neutron-rich nuclei with $N = 21$, ^{35}Si and ^{33}Mg , by beta decay of ^{35}Al and ^{33}Na . *Nucl. Phys. A*, 701:410c, 2002.
- [46] A.C. Morton, P. F. Mantica, B. A. Brown, A. D. Davies, D. E. Groh, b, P. T. Hosmer, S. N. Liddick, J. I. Prisciandaro, H. Schatz, M. Steiner, and A. Stolz. Beta decay studies of nuclei near ^{32}Mg : Investigating the small $\nu(f_{7/2}) - (d_{3/2})$ inversion at the $N = 20$ shell closure. *Phys. Lett. B*, 544:274, 2002.
- [47] V. Tripathi, S.L. Tabor, P.F. Mantica, C.R. Hoffman, M. Wiedeking, A.D. Davies, S.N. Liddick, W.F. Mueller, T. Otsuka, A. Stolz, B.E. Tomlin, Y. Utsuno, and A. Volya. ^{29}Na : Defining the edge of the island of inversion for $Z = 11$. *Phys. Rev. Lett.*, 94:162501, 2005.
- [48] N.A. Orr, W. Mittig, L.K. Fifield, M. Lewitowicz, E. Plagnol, Y. Schutz, Zhan Wen Long, L. Bianchi, A. Gillibert, A.V. Belozorov, S.M. Lukyanov, Yu. E. Penionzhkevich, A.C.C. Villari, A. Cunsolo, A. Foti, G. Audi, C. Stephan, and L. Tassan-Got. New mass measurements of neutron-rich nuclei near $N = 20$. *Phys. Lett. B*, 258:29, 1991.
- [49] A. Ozawa, T. Kobayashi, T. Suzuki, K. Yoshida, and I. Tanihata. New magic number, $N = 16$, near the neutron drip line. *Phys. Rev. Lett.*, 84:5493, 2000.
- [50] M. Keim, U. Georg, A. Klein, R. Neugart, M. Neuroth, S. Wilbert, P. Lievens, L. Vermeeren, and B.A. Brown. Measurement of the electric quadrupole moments of $^{26-29}\text{Na}$. *Eur. Phys. J. A*, 8:31, 2000.

-
- [51] T. Motobayashi, Y. Ikeda, K. Ieki, M. Inoue, N. Iwasa, T. Kikuchi, M. Kurokawa, S. Moriya, S. Ogawa, H. Murakami, S. Shimoura, Y. Yanagisawa, T. Nakamura, Y. Watanabe, M. Ishihara, T. Teranishi, H. Okuno, and R. F. Casten. Large deformation of the very neutron-rich nucleus ^{32}Mg from intermediate-energy Coulomb excitation. *Phys. Lett. B*, 346:9, 1995.
- [52] B.V. Pritychenko, T. Glasmacher, P.D. Cottle, M. Fauerbach, R.W. Ibbotson, K.W. Kemper, V. Maddalena, A. Navin, R. Ronningen, A. Sakharuk, H. Scheit, and V. G. Zelevinsky. Role of intruder configurations in $^{26,28}\text{Ne}$ and $^{30,32}\text{Mg}$. *Phys. Lett. B*, 461:322, 1999.
- [53] V. Chisté, A. Gillibert, A. Lepine-Szily, N. Alamanos, F. Auger, J. Barrette, F. Braga, M. D. Cortina-Gil, Z. Dlouhy, V. Lapoux, M. Lewitowicz, R. Lichtenthäler, R. Liguori Neto, S.M. Lukyanov, M. MacCormick, F. Marie, W. Mittig, F. de Oliveira Santos, N.A. Orr, A.N. Ostrowski, S. Ottini, A. Pakou, Yu.E. Penionzhkevich, P. Roussel-Chomaz, and J.L. Sida. Electric and nuclear transition strength in $^{30,32}\text{Mg}$. *Phys. Lett. B*, 514:233, 2001.
- [54] H. Iwasaki, T. Motobayashi, H. Sakurai, K. Yoneda, T. Gomi, N. Aoi, N. Fukuda, Zs. Fülöp, U. Futakami, Z. Gacsi, Y. Higurashi, N. Imai, N. Iwasa, T. Kubo, M. Kunibu, M. Kurokawa, Z. Liu, T. Minemura, A. Saito, M. Serata, S. Shimoura, S. Takeuchi, Y.X. Watanabe, K. Yamada, Y. Yanagisawa, and M. Ishihara. Large collectivity of ^{34}Mg . *Phys. Lett. B*, 522:227, 2001.
- [55] Oliver Thomas Niedermaier. *Low-Energy Coulomb-Excitation of the Neutron-Rich Mg Isotopes ^{30}Mg and ^{32}Mg* . Dissertation, Universität Heidelberg, 2005.
- [56] Vinzenz Bildstein. Particle detection at REX-ISOLDE and the $d(^{30}\text{Mg}, ^{31}\text{Mg})p$ reaction. Diplomarbeit, Universität Heidelberg, 2005.
- [57] E. Kugler. The ISOLDE facility. *Hyperf. Int.*, 129:23, 2000.
- [58] E. Kugler, D. Fiander, B. Johnson, H. Haas, A. Przewloka, H. L. Ravn, D. J. Simon, and K. Zimmer. The new CERN-ISOLDE on-line mass-separator facility at the PS-Booster. *Nucl. Instr. Meth. B*, 70:41, 1992.
- [59] D. Habs, F. Ames, W. Assmann, S. Emhofer, O. Engels, M. Gross, O. Kester, H. J. Maier, P. Reiter, T. Sieber, and P. Thirolf. The REX-ISOLDE-project and the Munich accelerator for fission fragments MAFF. *Prog. Part. Nucl. Phys.*, 46:343–358, 2001.
- [60] D. Schwalm. First experiments with REX-ISOLDE and MINIBALL. In Aldo Covello, editor, *booktitle*, page 21. World Scientific, 2005. Proceedings of the 8th International Spring Seminar on Nuclear Physics.
- [61] Heiko Scheit. Rex scientific report. CERN-INTC-2004-030, INTC-SR-003, Scientific Report to the INTC, 2004.
- [62] J. Lettry, R. Catherall, P. Drumm, P. Van Duppen, A. H. M. Evensen, G. J. Focker, A. Jockinen, O. C. Jonsson, E. Kugler, H. Ravn, and ISOLDE Collaboration. Pulse shape of the ISOLDE radioactive ion beams. *Nucl. Instr. Meth. B*, 126:130–134, 1997.
-

-
- [63] <http://www.ganil.fr/>.
- [64] C. J. Gross, T. N. Ginter, D. Shapira, W. T. Milner, J. W. McConnell, A. N. James, J. W. Johnson, J. Mas, P. F. Mantica, R. L. Auble, J. J. Das, J. L. Blankenship, J. H. Hamilton, R. L. Robinson, Y. A. Akovali, C. Baktash, J. C. Batchelder, C. R. Bingham, M. J. Brinkman, H. K. Carter, R. A. Cunningham, T. Davinson, J. D. Fox, A. Galindo-Uribarri, R. Grzywacz, J. F. Liang, B. D. MacDonald, J. MacKenzie, S. D. Paul, A. Piechaczek, D. C. Radford, A. V. Ramayya, W. Reviol, D. Rudolph, K. Rykaczewski, K. S. Toth, W. Weintraub, C. Williams, P. J. Woods, C. H. Yu, and E. F. Zganjar. Performance of the recoil mass spectrometer and its detector systems at the holifield radioactive ion beam facility. *Nucl. Instr. Meth. A*, 450:12–29, 2000.
- [65] V.N. Fedoseyev, G. Huber, U. Köster, J. Lettry, V.I. Mishin, H. Ravn, and V. Sebastian. The ISOLDE laser ion source for exotic nuclei. *Hyperf. Int.*, 127:409, 2000.
- [66] U. Köster, V. N. Fedoseyev, A. N. Andreyev, U. C. Bergmann, R. Catherall, J. Cederkäll, M. Dietrich, H. De Witte, D. V. Fedorov, L. Fraile, S. Franchoo, H. Fynbo, U. Georg, T. Giles, M. Gorska, M. Hannawald, M. Huyse, A. Joinet, O. C. Jonsson, K. L. Kratz, K. Kruglov, Ch. Lau, J. Lettry, V. I. Mishin, M. Oinonen, K. Partes, K. Peräjärvi, B. Pfeiffer, H. L. Ravn, M. D. Seliverstov, P. Thierolf, K. Van de Vel, P. Van Duppen, J. Van Roosbroeck, and L. Weissman. On-line yields obtained with the ISOLDE RILIS. *Nucl. Instr. Meth. B*, 204:347, 2003.
- [67] F. Ames, G. Bollen, P. Delahaye, O. Forstner, G. Huber, O. Kester, K. Reisinger, and P. Schmidt. Cooling of radioactive ions with the Penning trap REXTRAP. *Nucl. Instr. Meth. A*, 538:17, 2005.
- [68] F. Ames, J. Cederkäll, F. J. C. Wenander, and B. H. Wolf. REXEBIS operation and developments. *Rev. Sci. Instr.*, 75:1607, 2004.
- [69] H. Podlech, M. Grieser, R. von Hahn, S. Papureanu, R. Repnow, and D. Schwalm. The 7-gap-resonator-accelerator for the REX-ISOLDE-experiment at CERN. *Nucl. Instr. Meth. B*, 139:447, 1998.
- [70] Dirk Werner Weißhaar. *MINIBALL Ein neuartiges Gamma-Spektrometer mit ortsaufauflösenden Germaniumdetektoren*. Dissertation, Universität zu Köln, 2002.
- [71] Kurt Alder and Aage Winther. *Electromagnetic excitation: theory of Coulomb excitation with heavy ions*. North-Holland, 1975.
- [72] D. Cline. Nuclear shapes studied by Coulomb excitation. *Ann. Rev. Nucl. Part. Sci.*, 36:683, 1986.
- [73] D. Schwalm, E.K. Warburton, and J.W. Olness. Coulomb excitation of *sd* shell nuclei: a self-contained set of $B(E2)$ values and lifetime measurements. *Nucl. Phys. A*, 293:425, 1977.
-

-
- [74] D. Schwalm, A. Bamberger, P.G. Bizzeti, B. Povh, G.A.P. Engelbertink, J.W. Olness, and E.K. Warburton. Reorientation measurements using the Doppler-shift method: static quadrupole moments of ^{20}Ne , ^{22}Ne , ^{24}Mg , ^{26}Mg and ^{28}Si . *Nucl. Phys. A*, 192:449, 1972.
- [75] R. Bock, editor. *Heavy Ion Collisions*. North-Holland, 1982.
- [76] Reiner Bass. *Nuclear Reactions with Heavy Ions*. Texts and Monographs in Physics. Springer Verlag, Heidelberg, 1980.
- [77] G.R. Satchler. *Introduction to Nuclear Reactions*. Oxford University Press, New York, second edition, 1990.
- [78] Heinz G. Thomas. *Entwicklung eines Germanium-CLUSTER-Detektors für das Gamma-Spektrometer EUROBALL*. Verlag Dr. Köster, Berlin, 1995. ISBN 3-89574-113-2.
- [79] <http://nnsa.dl.ac.uk/euroball-home/>.
- [80] D. Pansegrau, P. Reiter, D. Schwalm, H. Bauer, J. Eberth, D. Gassmann, D. Habs, T. Härtlein, F. Köck, and H.G. Thomas. γ -spectroscopy in the superdeformed minimum of ^{240}Pu . *Phys. Lett. B*, 484:1, 2000.
- [81] J. Eberth, H. G. Thomas, D. Weisshaar, F. Becker, B. Fiedler, S. Skoda, P. Von Brentano, C. Gund, L. Palafox, P. Reiter, D. Schwalm, D. Habs, T. Servene, R. Schwengner, H. Schnare, W. Schulze, H. Prade, G. Winter, A. Jungclaus, C. Lingk, C. Teich, and K. P. Lieb. Development of segmented Ge detectors for future γ -ray arrays. *Prog. Part. Nucl. Phys.*, 38:29–37, 1997.
- [82] <http://www.ganil.fr/diraces/exogam.html>.
- [83] <http://www-w2k.gsi.de/agata/>.
- [84] <http://greta.lbl.gov/>.
- [85] J. Eberth, H.G. Thomas, P. v. Brentano, R.M. Lieder, H.M. Jäger, H. Kämmerling, M. Berst, D. Gutknecht, and R. Henck. Encapsulated Ge detectors: Development and first tests. *Nucl. Instr. Meth. A*, 369:135–140, 1996.
- [86] D. Habs, D. Rudolph, P. Thirolf, C. Fischbeck, Ch. Gund, D. Schwalm, J. Eberth, E. Grosse, H. Prade, H. Emling, J. Gerl, R. M. Lieder, P. Van Duppen, C. Rossi-Alvarez, and M. Pignanelli. Physics with Ge-Miniball-Arrays. *Prog. Part. Nucl. Phys.*, 38:111–126, 1997.
- [87] EURISYS, Strasbourg, France.
- [88] Cryostat and Detector Technique Thomas, Montabaur, Germany.
- [89] The DGF4C modules were procured from X-ray Instrumentation Associates, Newark, CA, USA.
- [90] A.N. Ostrowski, S. Cherubini, T. Davinson, D. Groombridge, A.M. Laird, A. Musumarra, A. Ninane, A. di Pietro, A.C. Shotter, and P.J. Woods. CD: A double sided silicon strip detector for radioactive nuclear beam experiments. *Nucl. Instr. Meth. A*, 480:448, 2002.
- [91] The CD detector was procured from MICRON Semiconductor Ltd.
-

-
- [92] J. Cub, C. Gund, D. Pansegrau, G. Schrieder, and H. Stelzer. A position sensitive parallel plate avalanche counter for single particle and current readout. *Nucl. Instr. Meth. A*, 453:522, 2000.
- [93] C. Gund, H. Bauer, J. Cub, A. Dietrich, T. Härtlein, H. Lenske, D. Pansegrau, A. Richter, H. Scheit, G. Schrieder, and D. Schwalm. Potential and limitations of nucleon transfer experiments with radioactive beams at REX-ISOLDE. *Eur. Phys. J. A*, 10:85, 2001.
- [94] J.M. Eisenberg and W. Greiner. *Excitation mechanisms of the nucleus*, volume 2 of *Nuclear Theory*. North-Holland, Amsterdam, 3rd edition, 1988.
- [95] K. Alder, A. Bohr, T. Huus, B. Mottelson, and A. Winther. Study of nuclear structure by electromagnetic excitation with accelerated ions. *Rev. Mod. Phys.*, 28:432, 1956.
- [96] Albert Messiah. *Quantenmechanik*, volume 1. de Gruyter, Berlin, 2nd edition, 1991.
- [97] L. D. Tolsma. Solving coupled equations by iteration for heavy ion multiple Coulomb excitation. *Phys. Rev. C*, 20:592, 1979.
- [98] N. Rowley and P. Colombani. Classical description of the Coulomb excitation of very heavy deformed nuclei. *Phys. Rev. C*, 11:648, 1975.
- [99] S.S.M. Wong. *Introductory Nuclear Physics*. Prentice-Hall, New Jersey, 1990.
- [100] A. Winther and J. de Boer. A computer program for multiple Coulomb excitation. Technical report, California Institute of Technology, 1965. reprinted in [101] p. 303.
- [101] Kurt Alder and Aage Winther. *Coulomb Excitation*. Academic Press, London, 1966.
- [102] H. Ower. Coulomb excitation code CLX.
- [103] Alois Lell. Rechnerprogramm für Coulomb-Anregung. Diplomarbeit, Universität München, 1978. Unpublished.
- [104] T. Czosnyka, D. Cline, L. Hasselgren, C.Y. Wu, R.M. Diamond, H. Kluge, C. Roulet, E.K. Hulet, R.W. Loughheed, and C. Baktash. E2 properties of the ground state band in ^{248}Cm . *Nucl. Phys. A*, 458:123, 1986.
- [105] Jorrit de Boer and Jörg Eichler. *The reorientation effect*, chapter 1, pages 1–65. Volume 1 of Baranger and Vogt [106], 1968.
- [106] Michel Baranger and Erich Vogt, editors. *Advances in Nuclear Physics*. Plenum Press, New York, 1968.
- [107] K. Alder and R.M. Steffen. Electromagnetic moments of excited nuclear states. *Ann. Rev. Nucl. Sci.*, 14:403–482, 1964.
- [108] F.W.N. de Boer, H.J. Wollersheim, H. Emling, H. Grein, E. Grosse, W. Spreng, G. Eckert, Th.W. Elze, K. Stelzer, and Ch. Lauterbach. Nucleon transfer reactions to rotational states induced by $^{206,208}\text{Pb}$ projectiles. *Z. Phys. A*, 325:457, 1986.
- [109] W.W. Wilcke, J.R. Birkelund, H.J. Wollersheim, A.D. Hoover, J.R. Huizenga, W.U. Schröder, and L.E. Tubbs. Reaction parameters for heavy-ion collisions. *Atom. Data and*
-

- Nucl. Data Tab.*, 25:389, 1980.
- [110] S. Wan, J. Gerl, J. Cub, J.M. Holeczek, P. Reiter, D. Schwalm, T. Aumann, K. Boretzky, W. Dostal, B. Eberlein, H. Emling, Ch. Ender, Th.W. Elze, H. Geissel, A. Grünschloß, R. Holzmann, N. Iwasa, M. Kaspar, A. Kleinböhl, O. Koschorreck, Y. Leifels, A. Leisten-schneider, I. Peter, H. Schaffner, C. Scheidenberger, R. Schubart, R. Schubert, H. Simon, G. Stengel, A. Surowiec, and H.J. Wollersheim. In-beam γ -spectroscopy with relativistic radioactive ion beams. *Eur. Phys. J. A*, 6:167–174, 1999.
- [111] H. Scheit, T. Glasmacher, B. A. Brown, J. A. Brown, P. D. Cottle, P. G. Hansen, R. Harkewicz, M. Hellström, R. W. Ibbotson, J. K. Jewell, K. W. Kemper, D. J. Morrissey, M. Steiner, P. Thirolf, and M. Thoennessen. New region of deformation: The neutron-rich sulfur isotopes. *Phys. Rev. Lett.*, 77:3967, 1996.
- [112] R. Anne, D. Bazin, R. Bimbot, et al. Projectile Coulomb excitation with fast radioactive beams. *Z. Phys. A*, 352:397, 1995.
- [113] Aage Winther and Kurt Alder. Relativistic Coulomb excitation. *Nucl. Phys. A*, 319:518–532, 1979.
- [114] O. Niedermaier, H. Scheit, V. Bildstein, H. Boie, J. Fitting, R. von Hahn, F. Köck, M. Lauer, U.K. Pal, H. Podlech, R. Repnow, D. Schwalm, C. Alvarez, F. Ames, G. Bollen, S. Emhofer, D. Habs, O. Kester, R. Lutter, K. Rudolph, M. Pasini, P.G. Thirolf, B.H. Wolf, J. Eberth, G. Gersch, H. Hess, P. Reiter, O. Thelen, N. Warr, D. Weisshaar, F. Aksouh, P. Van den Bergh, P. Van Duppen, M. Huyse, O. Ivanov, P. Mayet, J. Van de Walle, J. Äystö, P.A. Butler, J. Cederkäll, P. Delahaye, H.O.U. Fynbo, L.M. Fraile, O. Forstner, S. Franchoo, U. Köster, T. Nilsson, M. Oinonen, T. Sieber, F. Wenander, M. Pantea, A. Richter, G. Schrieder, H. Simon, T. Behrens, R. Gernhäuser, T. Kröll, R. Krücken, M. Münch, T. Davinson, J. Gerl, G. Huber, A. Hurst, J. Iwanicki, B. Jonson, P. Lieb, L. Liljeby, A. Schempp, A. Scherillo, P. Schmidt, and G. Walter. "Safe" Coulomb Excitation of ^{30}Mg . *Phys. Rev. Lett.*, 94:172501, 2005.
- [115] H. Scheit, T. Glasmacher, R.W. Ibbotson, and P.G. Thirolf. A position sensitive high-efficiency NaI(Tl) photon-detection system for use with intermediate energy radioactive ion beams. *Nucl. Instr. Meth. A*, 422:124–128, 1999.
- [116] O. Niedermaier, H. Scheit, V. Bildstein, H. Boie, J. Fitting, R. von Hahn, F. Köck, M. Lauer, U.K. Pal, H. Podlech, R. Repnow, D. Schwalm, C. Alvarez, F. Ames, G. Bollen, S. Emhofer, D. Habs, O. Kester, R. Lutter, K. Rudolph, M. Pasini, P.G. Thirolf, B.H. Wolf, J. Eberth, G. Gersch, H. Hess, P. Reiter, O. Thelen, N. Warr, D. Weisshaar, F. Aksouh, P. Van den Bergh, P. Van Duppen, M. Huyse, O. Ivanov, P. Mayet, J. Van de Walle, J. Äystö, P.A. Butler, J. Cederkäll, P. Delahaye, H.O.U. Fynbo, L.M. Fraile, O. Forstner, S. Franchoo, U. Köster, T. Nilsson, M. Oinonen, T. Sieber, F. Wenander, M. Pantea, A. Richter, G. Schrieder, H. Simon, T. Behrens, R. Gernhäuser, T. Kröll, R. Krücken, M. Münch,
-

- T. Davinson, J. Gerl, G. Huber, A. Hurst, J. Iwanicki, B. Jonson, P. Lieb, L. Liljeby, A. Schempp, A. Scherillo, P. Schmidt, and G. Walter. The neutron-rich Mg isotopes: first results from MINIBALL at REX-ISOLDE. *Nucl. Phys. A*, 752:273, 2005.
- [117] Hans Boie. Aufbau eines Experimentes zur Messung der Emissionswahrscheinlichkeit von Bremsstrahlung im α -Zerfall von ^{210}Po . Diplomarbeit, Universität Heidelberg, 2002.
- [118] H. Boie. MINIBALL GEANT4 simulation. Technical report, 2005.
- [119] H. Scheit, O. Niedermaier, F. Ames, J. Äystö, U. Bergmann, J. Cederkäll, P. Dessagne, J. Eberth, J. Fitting, L. Fraile, S. Franchoo, D. Habs, M. Huyse, A. Jungclaus, O. Kester, M. Lauer, P. Mayet, T. Nilsson, U. Pal, M. Pantea, P. Reiter, A. Richter, G. Schrieder, D. Schwalm, H. Simon, D. Smirnov, P. Thirolf, P. van Duppen, R. von Hahn, N. Warr, and D. Weisshaar. Evolution of single particle and collective properties in the neutron-rich Mg isotopes. CERN-INTC-2002-020, 2002. Proposal to the INTC.
- [120] H. Scheit, F. Aksouh, F. Ames, T. Behrens, V. Bildstein, H. Boie, P. Butler, J. Cederkäll, T. Davinson, P. Delahaye, P. Van Duppen, J. Eberth, S. Emhofer, S. Franchoo, R. Gernhäuser, G. Gersch, D. Habs, R. v. Hahn, H. Hess, A. Hurst, M. Huyse, O. Ivanov, J. Iwanicki, O. Kester, F. Köck, U. Köster, T. Kröll, R. Krücken, M. Lauer, R. Lutter, P. Mayet, M. Münch, O. Niedermaier, U.K. Pal, M. Pantea, M. Pasini, P. Reiter, A. Richter, A. Scherillo, G. Schrieder, D. Schwalm, T. Sieber, H. Simon, O. Thelen, P. Thirolf, J. van de Walle, N. Warr, and D. Weisshaar. Coulomb excitation of ^{32}Mg . CERN-INTC-2004-009, 2004. Proposal to the INTC.
- [121] Heiko Scheit. *Low-Lying Collective Excitations in Neutron-Rich Sulfur and Argon Isotopes Studied via Intermediate-Energy Coulomb Excitation and Proton Scattering*. PhD thesis, Michigan State University, 1998.
- [122] Philip R. Bevington and D. Keith Robinson. *Data Reduction and Error Analysis for the Physical Sciences*. McGraw-Hill, Boston, 2nd edition, 1992.
- [123] H. Scheit. First γ -rays from radioactive beams at REX-ISOLDE. *Eur. Phys. J. A*, 20:67, 2004.
- [124] H. Scheit, O. Niedermaier, M. Pantea, F. Aksouh, C. Alvarez, F. Ames, T. Behrens, V. Bildstein, H. Boie, P. Butler, J. Cederkäll, T. Davinson, P. Delahaye, P. Van Duppen, J. Eberth, S. Emhofer, J. Fitting, S. Franchoo, R. Gernhäuser, G. Gersch, D. Habs, R.v. Hahn, H. Hess, A. Hurst, M. Huyse, O. Ivanov, J. Iwanicki, O. Kester, F. Köck, T. Kröll, R. Krücken, M. Lauer, R. Lutter, P. Mayet, M. Münch, U.K. Pal, M. Pasini, P. Reiter, A. Richter, A. Scherillo, k, G. Schrieder, D. Schwalm, T. Sieber, H. Simon, O. Thelen, P. Thirolf, J. van de Walle, N. Warr, and D. Weißhaar. First results on in-beam γ spectroscopy of neutron-rich Na and Mg isotopes at REX-ISOLDE. *Nucl. Phys. A*, 746:96c, 2004.
- [125] H. Scheit, O. Niedermaier, V. Bildstein, H. Boie, J. Fitting, R. von Hahn, F. Köck, M. Lauer, U. K. Pal, H. Podlech, R. Repnow, D. Schwalm, C. Alvarez, F. Ames, G. Bollen, S. Emhofer,

- D. Habs, O. Kester, R. Lutter, K. Rudolph, M. Pasini, P. G. Thirolf, B. H. Wolf, J. Eberth, G. Gersch, H. Hess, P. Reiter, O. Thelen, N. Warr, D. Weisshaar, F. Aksouh, P. Van den Bergh, P. Van Duppen, M. Huyse, O. Ivanov, P. Mayet, J. Van de Walle, J. Äystö, P. A. Butler, J. Cederkäll, P. Delahaye, H. O. U. Fynbo, L. M. Fraile, O. Forstner, S. Franchoo, U. Köster, T. Nilsson, M. Oinonen, T. Sieber, F. Wenander, M. Pantea, A. Richter, G. Schrieder, H. Simon, T. Behrens, R. Gernhäuser, T. Kröll, R. Krücken, M. Münch, T. Davinson, J. Gerl, G. Huber, A. Hurst, J. Iwanicki, B. Jonson, P. Lieb, L. Liljeby, A. Schempp, A. Scherillo, P. Schmidt, and G. Walter. Coulomb excitation of neutron-rich beams at REX-ISOLDE. *Eur. Phys. J. A*, 25:397 – 402, 2005.
- [126] H. Mach, L. M. Fraile, O. Tengblad, R. Boutami, C. Jollet, W. A. Plociennik, D. T. Yordanov, M. Stanoiu, M. J. G. Borge, P. A. Butler, J. Cederkäll, Ph. Dessagne, B. Fogelberg, H. Fynbo, P. Hoff, A. Jokinen, A. Korgul, U. Köster, W. Kurcewicz, F. Marechal, T. Motobayashi, J. Mrazek, G. Neyens, T. Nilsson, S. Pedersen, A. Poves, B. Rubio, and E. Ruchowska. New structure information on ^{30}Mg , ^{31}Mg and ^{32}Mg . *Eur. Phys. J. A*, 25:105 – 109, 2005.
- [127] A. Gade, D. Bazin, A. Becerril, C. M. Campbell, J. M. Cook, D. J. Dean, D.-C. Dinca, T. Glasmacher, G. W. Hitt, M. E. Howard, W. F. Mueller, H. Olliver, J. R. Terry, and K. Yoneda. Quadrupole deformation of the self-conjugate nucleus ^{72}Kr . *Phys. Rev. Lett.*, 95:022502, 2005.
- [128] A. Bürger, T.R. Saito, H. Grawe, H. Hübel, P. Reiter, J. Gerl, M. Górska, H.J. Wollersheim, A. Al-Khatib, A. Banu, T. Beck, F. Becker, P. Bednarczyk, G. Benzoni, A. Bracco, S. Brambilla, P. Bringel, F. Camera, E. Clément, P. Doornenbal, H. Geissel, A. Görgen, J. Grebosz, G. Hammond, M. Hellström, M. Honma, M. Kavatsyuk, O. Kavatsyuk, M. Kmiecik, I. Kojouharov, W. Korten, N. Kurz, R. Lozeva, A. Maj, S. Mandal, B. Million, S. Muralithar, A. Neußera, F. Nowacki, T. Otsuka, Zs. Podolyáko, N. Saitob, A.K. Singh, H. Weick, C. Wheldon, O. Wieland, and M. Winkler. Relativistic Coulomb excitation of neutron-rich $^{54,56,58}\text{Cr}$: On the pathway of magicity from $N = 40$ to $N = 32$. *Phys. Lett. B*, 622:29–34, 2005.
- [129] B. A. Brown. The nuclear shell model towards the drip lines. *Prog. Part. Nucl. Phys.*, 47:517–599, 2001.
- [130] T. Otsuka, M. Honma, T. Mizusaki, N. Shimizu, and Y. Utsuno. Monte Carlo shell model for atomic nuclei. *Prog. Part. Nucl. Phys.*, 47:319, 2001.
- [131] E. Caurier, G. Martínez-Pinedo, F. Nowacki, A. Poves, and A. P. Zuker. The shell model as a unified view of nuclear structure. *Rev. Mod. Phys.*, 77:427–488, 2005.
- [132] E. Caurier, F. Nowacki, A. Poves, and J. Retamosa. Shell model study of the neutron rich isotopes from oxygen to silicon. *Phys. Rev. C*, 58:2033, 1998.
- [133] T. Siiskonen, P. O. Lipas, and J. Rikowska. Shell-model and Hartree-Fock calculations for
-

- even-mass O, Ne, and Mg nuclei. *Phys. Rev. C*, 60:034312, 1999.
- [134] D. J. Dean, M. T. Ressel, M. Hjorth-Jensen, S. E. Koonin, K. Langanke, and A. P. Zuker. Shell-model Monte Carlo studies of neutron-rich nuclei in the $1s-0d-1p-0f$ shells. *Phys. Rev. C*, 59:2472, 1999.
- [135] Y. Utsuno, T. Otsuka, T. Mizusaki, and M. Honma. Varying shell gap and deformation in $N \sim 20$ unstable nuclei studied by the Monte Carlo shell model. *Phys. Rev. C*, 60:054315, 1999.
- [136] S. Péru, M. Girod, and J.F. Berger. Evolution of the $N = 20$ and $N = 28$ shell closures in neutron-rich nuclei. *Eur. Phys. J. A*, 9:35, 2000.
- [137] R. Rodríguez-Guzmán, J.L Egido, and L.M. Robledo. Angular momentum projected analysis of quadrupole collectivity in $^{30,32,34}\text{Mg}$ and $^{32,34,36,38}\text{Si}$ with the Gogny interaction. *Phys. Lett. B*, 474:15, 2000.
- [138] E. Caurier, F. Nowacki, and A. Poves. Shell model studies of neutron-rich nuclei. *Nucl. Phys. A*, 693:374, 2001.
- [139] Yutaka Utsuno, Takaharu Otsuka, Takahiro Mizusaki, and Michio Honma. Extreme location of F drip line and disappearance of the $N = 20$ magic structure. *Phys. Rev. C*, 64:011301(R), 2001.
- [140] Takaharu Otsuka, Rintaro Fujimoto, Yutaka Utsuno, B. Alex Brown, Michio Honma, and Takahiro Mizusaki. Magic numbers in exotic nuclei and spin-isospin properties of the NN interaction. *Phys. Rev. Lett.*, 87:082502, 2001. See also the Comment [186] and the Reply [187].
- [141] T. Otsuka, Y. Utsuno, R. Fujimoto, B.A. Brown, M. Honma, and T. Mizusaki. Frontiers and challenges of nuclear shell model. *Eur. Phys. J. A*, 15:151, 2002.
- [142] R. Rodríguez-Guzmán, J.L Egido, and L.M. Robledo. Correlations beyond the mean field in magnesium isotopes: angular momentum projection and configuration mixing. *Nucl. Phys. A*, 709:201–235, 2002.
- [143] P.D. Stevenson, J. Rikowska Stone, and M. R. Strayer. Mean field calculation of Ne, Mg and Si nuclei at $N = 20$ with the separable monopole interaction. *Phys. Lett. B*, 545:291, 2002.
- [144] Masaaki Kimura and Hisashi Horiuchi. Breaking of the neutron magic number $N = 20$ in ^{32}Mg and ^{30}Ne and its possible relation to the cluster structure. *Prog. Theo. Phys.*, 107:33, 2002.
- [145] Y. Utsuno, T. Otsuka, T. Mizusaki, and M. Honma. Monte Carlo shell model calculation for unstable nuclei around $N = 20$. *Nucl. Phys. A*, 704:50c, 2002.
- [146] R.R. Rodríguez-Guzmán, J.L. Egido, and L.M. Robledo. Quadrupole collectivity of neutron-rich neon isotopes. *Eur. Phys. J. A*, 17:37, 2003.
-

-
- [147] Yutaka Utsuno, Takaharu Otsuka, Thomas Glasmacher, Takahiro Mizusaki, and Michio Honma. Onset of intruder ground state in exotic Na isotopes and evolution of the $N = 20$ shell gap. *Phys. Rev. C*, 70:044307, 2004.
- [148] M. Yamagami and Nguyen Van Giai. Pairing effects on the collectivity of quadrupole states around ^{32}Mg . *Phys. Rev. C*, 69:034301, 2004.
- [149] S. Khaled, M. Ramdhane, and F. Benrachi. Application of the weak-coupling model for calculating the binding energies of neutron-rich $A \sim 32$ nuclei. *Eur. Phys. J. A*, 22:17, 2004.
- [150] M. Kimura and H. Horiuchi. Many-particle and many-hole states in neutron-rich Ne isotopes related to broken $N = 20$ shell closure. *Prog. Theo. Phys.*, 111:841–855, 2004.
- [151] N. Van Giai and M. Yamagami. QRPA coordinate space calculations of 2^+ states in $N = 20$ isotones. *Phys. Atom. Nucl.*, 67:1633–1639, 2004.
- [152] T. Otsuka. Shell model results for exotic nuclei. *Eur. Phys. J. A*, 20:69, 2004.
- [153] J. Retamosa, E. Caurier, F. Nowacki, and A. Poves. Shell model study of the neutron-rich nuclei around $N = 28$. *Phys. Rev. C*, 55:1266, 1997.
- [154] T. T. S. Kuo and G. E. Brown. Reaction matrix elements for the $0f$ - $1p$ shell nuclei. *Nucl. Phys. A*, 114:241, 1968.
- [155] D. J. Millener and D. Kurath. The particle-hole interaction and the beta decay of ^{14}B . *Nucl. Phys. A*, 255:315–338, 1975.
- [156] Peter Ring and Peter Schuck. *The Nuclear Many-Body Problem*. Texts and Monographs in Physics. Springer-Verlage, Heidelberg, 1980.
- [157] J. Terasaki, H. Flocard, P. H. Heenen, and P. Bonche. Deformation of nuclei close to the two-neutron drip line in the Mg region. *Nucl. Phys. A*, 621:706, 1997.
- [158] Zhongzhou Ren, Z. Y. Zhu, Y. H. Cai, and Gongou Xu. Relativistic mean-field study of Mg isotopes. *Phys. Lett. B*, 380:241, 1996.
- [159] Richard F. Casten. *Nuclear Structure from a Simple Perspective*. Oxford University Press, second edition, 2000.
- [160] D. Habs, O. Kester, F. Ames, T. Sieber, H. Bongers, et al. Coulomb excitation of neutron-rich $A \sim 140$ nuclei. CERN-INTC-2002-015, 2002. Proposal to the INTC.
- [161] Th. Kröll, R. Krücken, T. Behrens, T. Faestermann, R. Gernhäuser, M. Mahgoub, P. Maierbeck, P. Thirolf, T. Morgan, D. Habs, O. Kester, R. Lutter, H. Scheit, O. Niedermaier, V. Bildstein, D. Schwalm, N. Warr, D. Martin, J. Iwanicki, P. Delahaye, F. Wenander, L. Fraile, P. Butler, T. Sieber, U. Köster, G. Georgiev, S. Franchoo, A. Scherillo, A. Hurst, P. Mayet, P. Van Duppen, J. Van De Walle, I. Stefanescu, M. Huyse, M. Pantea, T. Davinson, and D. Weisshaar. Coulomb excitation of neutron-rich $A \approx 140$ nuclei. CERN-INTC-2005-011, 2005. Proposal to the INTC.
-

-
- [162] Amos de-Shalit and Igal Talmi. *Nuclear Shell Theory*. Academic Press, New York, 1963.
 - [163] Theo Mayer-Kuckuk. *Kernphysik: Eine Einführung*. Teubner, Stuttgart, 6th edition, 1994.
 - [164] J. Dobaczewski, W. Nazarewicz, T.R. Werner, J.F. Berger, C.R. Chinn, and J. Dechargé. Mean-field description of ground-state properties of drip-line nuclei: Pairing and continuum effects. *Phys. Rev. C*, 53:2809, 1996.
 - [165] Hubert Grawe. *Shell Model from a Practitioner's Point of View*, volume 1, page 33. Springer-Verlag Heidelberg, 2004.
 - [166] J. Duflo and A. P. Zuker. The nuclear monopole Hamiltonian. *Phys. Rev. C*, 59:R2347, 1999.
 - [167] G. Neyens, M. Kowalska, D. Yordanov, K. Blaum, P. Himpe, P. Lievens, S. Mallion, R. Neugart, N. Vermeulen, Y. Utsuno, and T. Otsuka. Measurement of the spin and magnetic moment of ^{31}Mg : Evidence for a strongly deformed intruder ground state. *Phys. Rev. Lett.*, 94:022501, 2005.
 - [168] M.W. Cooper, S. L. Tabor, T. Baldwin, D.B. Campbell, C. Chandler, C.R. Hoffman, K.W. Kemper, J. Pavan, A. Pipidis, M.A. Riley, and M. Wiedeking. $T = \frac{5}{2}$ ^{27}Na from $^{14}\text{C} + ^{14}\text{C}$, and the $N = 16$ shell gap. *Phys. Rev. C*, 65:051302(R), 2002.
 - [169] B. V. Pritychenko, T. Glasmacher, P. D. Cottle, R. W. Ibbotson, K. W. Kemper, K. L. Miller, L. A. Riley, and H. Scheit. Transition to the “island of inversion”: Fast-beam γ -ray spectroscopy of $^{28,30}\text{Na}$. *Phys. Rev. C*, 66:024325, 2002.
 - [170] H. Ueno, D. Kameda, G. Kijima, K. Asahi, A. Yoshimi, H. Miyoshi, K. Shimada, G. Kato, D. Nagae, S. Emori, T. Haseyama, H. Watanabe, and M. Tsukui. Magnetic moments of $^{30}_{13}\text{Al}_{17}$ and $^{32}_{13}\text{Al}_{19}$. *Phys. Lett. B*, 615:186–192, 2005.
 - [171] H. Iwasaki, T. Motobayashi, H. Sakurai, K. Yoneda, T. Gomi, N. Aoi, N. Fukuda, Zs. Fülöp, U. Futakami, Z. Gacsi, Y. Higurashi, N. Imai, N. Iwasa, T. Kubo, M. Kunibu, M. Kurokawa, Z. Liu, T. Minemura, A. Saito, M. Serata, S. Shimoura, S. Takeuchi, Y.X. Watanabe, K. Yamada, Y. Yanagisawa, and M. Ishihara. Quadrupole collectivity of ^{28}Ne and the boundary of the island of inversion. *Phys. Lett. B*, 620:118, 2005.
 - [172] D. Borremans, S. Teughels, N. A. Smirnova, D. L. Balabanski, N. Coulier, J. M. Daugas, F. de Oliveira Santos, G. Georgiev, M. Lewitowicz, I. Matea, Yu. E. Penionzhkevich, W.-D. Schmidt-Ott, Yu. Sobolev, M. Stanoiu, K. Vyvey, and G. Neyens. Spin and magnetic moment of ^{31}Al ground state. *Phys. Lett. B*, 537:45, 2002.
 - [173] R. W. Ibbotson, T. Glasmacher, B. A. Brown, L. Chen, M. J. Chromik, P. D. Cottle, M. Fauerbach, K. W. Kemper, D. J. Morrissey, H. Scheit, and M. Thoennessen. Quadrupole collectivity in $^{32,34,36,38}\text{Si}$ and the $N = 20$ shell closure. *Phys. Rev. Lett.*, 80:2081, 1998.
 - [174] M. Notani, H. Sakurai, N. Aoi, Y. Yanagisawa, A. Saito, N. Imai, T. Gomi, M. Miura, S. Michimasa, H. Iwasaki, N. Fukuda, M. Ishihara, T. Kubo, S. Kubono, H. Kumagai, S. M.
-

- Lukyanov, T. Motobayashi, T. K. Onishi, Yu. E. Penionzhkevich, S. Shimoura, T. Teranishi, K. Ue, V. Ugryumov, and A. Yoshida. New neutron-rich isotopes, ^{34}Ne , ^{37}Na and ^{43}Si , produced by fragmentation of a 64 amev ^{48}Ca beam. *Phys. Lett. B*, 542:49, 2002.
- [175] W. Geithner, U. Georg, S. Kappertz, M. Keim, A. Klein, P. Lievens, R. Neugart, M. Neuroth, L. Vermeeren, and S. Wilbert. Measurement of nuclear moments and radii by collinear laser spectroscopy and by β -NMR spectroscopy. *Hyperf. Int.*, 129:271 – 288, 2000.
- [176] B. V. Pritychenko, T. Glasmacher, B. A. Brown, P. D. Cottle, R. W. Ibbotson, K. W. Kemper, and H. Scheit. Single-particle structure along the boundary of the “island of inversion”: Radioactive beam spectroscopy of ^{33}Si and ^{34}P . *Phys. Rev. C*, 62:051601, 2000.
- [177] Y. Yanagisawa, M. Notani, H. Sakurai, M. Kunibu, H. Akiyoshi, N. Aoi, H. Baba, K. Demichi, N. Fukuda, H. Hasegawa, Y. Higurashi, M. Ishihara, N. Iwasa, H. Iwasaki, T. Gomi, S. Kanno, M. Kurokawa, Y. U. Matsuyama, S. Michimasa, T. Minemura, T. Mizoi, T. Nakamura, A. Saito, M. Serata, S. Shimoura, T. Sugimoto, E. Takeshita, S. Takeuchi, K. Ue, K. Yamada, K. Yoneda, and T. Motobayashi. The first excited state of ^{30}Ne studied by proton inelastic scattering in reversed kinematics. *Phys. Lett. B*, 566:84, 2003.
- [178] M. Belleguic, M.-J. Lopez-Jimenez, M. Stanoiu, F. Azaiez, M.-G. Saint-Laurent, O. Sorlin, N. L. Achouri, J.-C. AngClique, C. Bourgeois, C. Borcea, J.-M. Daugas, C. Donzau, F. De Oliveira-Santos, J. Duprat, S. GrCvy, D. Guillemaud-Mueller, S. Leenhardt, M. Lewitowicz, Yu.-E. Penionzhkevich, and Yu. Sobolev. In-beam γ -spectroscopy using projectile fragmentation: Structure of neutron-rich nuclei around $N = 20$. *Nucl. Phys. A*, 682:136c, 2001.
- [179] N. Iwasa, T. Motobayashi, H. Sakurai, H. Akiyoshi, Y. Ando, N. Aoi, H. Baba, N. Fukuda, Z. Fülöp, U. Futakami, T. Gomi, Y. Higurashi, K. Ieki, H. Iwasaki, T. Kubo, S. Kubono, H. Kinugawa, H. Kumagai, M. Kunibu, S. Michimasa, T. Minemura, H. Murakami, K. Sagara, A. Saito, S. Shimoura, S. Takeuchi, Y. Yanagisawa, K. Yoneda, and M. Ishihara. In-beam γ spectroscopy of ^{34}Si with deuteron inelastic scattering using reverse kinematics. *Phys. Rev. C*, 67:064315, 2003.
- [180] B. V. Pritychenko, T. Glasmacher, P. D. Cottle, R. W. Ibbotson, K. W. Kemper, L. A. Riley, A. Sakharuk, H. Scheit, M. Steiner, and V. Zelevinsky. structure of the “island of inversion” nucleus ^{33}Mg . *Phys. Rev. C*, 65:061304(R), 2002.
- [181] B. V. Pritychenko, T. Glasmacher, B. A. Brown, P. D. Cottle, R. W. Ibbotson, K. W. Kemper, and H. Scheit. Shape coexistence on the boundary of the “island of inversion”: Exotic beam spectroscopy of ^{34}Al . *Phys. Rev. C*, 63:047308, 2001.
- [182] H. Sakurai, S. M. Lukyanov, M. Notani, N. Aoi, D. Beaumel, N. Fukuda, M. Hirai, E. Ideguchi, N. Imai, M. Ishihara, H. Iwasaki, T. Kubo, K. Kusaka, H. Kumagai, T. Nakamura, H. Ogawa, Yu. E. Penionzhkevich, T. Teranishi, Y. X. Watanabe, K. Yoneda, and A. Yoshida. Evidence for particle stability of ^{31}F and particle instability of ^{25}N and ^{28}O .
-

- Phys. Lett. B*, 448:180, 1999.
- [183] K. Yoneda, H. Sakurai, T. Gomi, T. Motobayashi, N. Aoi, N. Fukuda, U. Futakami, Z. Gacsi, Y. Higurashi, N. Imai, N. Iwasa, H. Iwasaki, T. Kubo, M. Kunibu, M. Kurokawa, Z. Liu, T. Minemura, A. Saito, M. Serata, S. Shimoura, S. Takeuchi, Y.X. Watanabe, K. Yamada, Y. Yanagisawa, K. Yogo, A. Yoshida, and M. Ishihara. Deformation of ^{34}Mg studied via in-beam γ -ray spectroscopy using radioactive-ion projectile fragmentation. *Phys. Lett. B*, 499:233, 2001.
- [184] M. Pantea. . Dissertation, TU Darmstadt, 2005.
- [185] P.A. Butler. Through the looking glass: probing the nucleus using accelerated radioactive beams. *Nucl. Phys. A*, 751:485–493, 2005.
- [186] A. P. Zuker. Comment on “magic numbers in exotic nuclei and spin-isospin properties of the NN interaction”. *Phys. Rev. Lett.*, 91:179201, 2003. Comment on [140]. See also the Reply [187].
- [187] T. Otsuka, R. Fujimoto, Y. Utsuno, B. A. Brown, M. Honma, and T. Mizusaki. Otsuka et al. reply. *Phys. Rev. Lett.*, 91:179202, 2003. Reply to comment [186].
-